Modeling and Parameterization of Basin Effects for Engineering Design Applications

Thesis by
Peyman Ayoubi

In Partial Fulfillment of the Requirements for the
Degree of
Doctor of Philosophy

CALIFORNIA INSTITUTE OF TECHNOLOGY
Pasadena, California

2022
Defended June 29, 2021

Peyman Ayoubi
ORCID: 0000-0001-6795-4923

To my family.

Acknowledgements

I would like to express my deepest gratitude to my advisor, Professor Domniki Asimaki, for her help and guidance. She has taught me so much and was there in difficult times. She encouraged me to explore new ideas and grow as an independent researcher. I feel fortunate to be one of her students.

I would also like to extend my appreciation to my committee members, Professor Jean-Philippe Avouac, Professor Monica D. Kohler, and Professor Zachary E. Ross. They have offered valuable guidance. Their advice and perspectives helped to improve the quality of the current work.

I want to thank all the current and previous members of the Asimaki (a.k.a. Geoquake) group. I will miss all the times we talked and laughed in group meetings, and my conversations with Kien, Danilo, Jian, and Joaquin in the basement of Gates-Thomas (B112). The CS nights are among my best memories from Caltech. In addition, I would like to give a special thanks to Professor Kami Mohammadi. Kami was my mentor and my go-to for any research-related question. I will never forget all the scientific arguments, funny moments, and late-night discussions in the office. I would also like to thank Professor Elnaz Seylabi. She was there every time I needed help and was ready to share her perspective and experiences in both academic and non-academic matters.

I'd like to thank Professor Kamyar Azizzadenesheli. I enjoyed collaborating with him on the third chapter of this thesis.

I would like to thank the MCE faculty members. I've learned a lot in courses, and conversations during Monday's coffee hour. I also would like to thank the MCE staff members who were always helpful and supportive.

I want to thank the International Student Program (ISP) staff, Daniel and Laura. I used to walk to their offices just to talk to them for 10 minutes. Seeing them smile is one of the memories I will never forget from Caltech.

I want to thank all my friends here at Caltech: Amirhossein, Pooya, Omid, Ehsan, Pourya, Fariborz, Parham, Aryaan, and Mostafa, who have been instrumental to my Caltech experience and without whom my life would have been much harder. I'll miss the times we sat for a coffee in the MCE lobby or Red Door, walked all over the campus multiple times, played PS, and went to Doghaus on Sunday nights. In addition, I also want to thank Saumya, Tomo, Zoila, and all the people in the 2015 cohort with whom I've shared a lot of great experiences. Moreover, I want to thank Majid, Alireza S., Alireza Y., Payam, and Javad.

I've spent two crazy years with them during my master's studies at Sharif University, and still enjoy talking to them every now and then.

I also want to thank my dear friend from my undergrad studies, Farshid. Although we've been on two different continents, he always had time for a friendly chat, scientific discussion, and going over old memories.

I want to mention my friends from middle school, Hossein and Pourya. They've always been a source of fun memories and conversations.

A special thanks should go to my cousins Mehran and Soraya Kohansal and their families. They have been there for me and Samira from the day I landed in the U.S. Being with them feels like home.

Next, I want to thank my family (my mom Matin, my dad Akbar, my little sister Yeganeh, and my brother-in-law Pejman) who have supported me and believed in me. I was lucky to be raised in such a family and be surrounded by them. I also want to thank my in-laws, Liana, Tala, Ghadir, Sara, and Mohammad, who have been a source of motivation.

Last but not least, I want to thank my wife. Samira, you are my rock, and I am grateful that I was not alone in this journey. I appreciate your understanding and patience from day one.

Abstract

The term "Basin effects" refers to trapped and reverberating earthquake waves in soft sedimentary deposits overlying convex depressions of the basement bedrock, which significantly alter frequency content, amplitude, and duration of seismic waves. This has played an important role in shaking duration and intensity in past earthquakes such as the M_w 8.0 1985 Michoácan, Mexico, M_w 6.9 1995 Kobe, Japan, and M_w 7.8 2015 Gorkha, Nepal earthquakes. While the standard practice is to perform a 1D analysis of a soil column, edge effect and surface waves are among the key contributors to the surface ground motion within a basin. This thesis studies basin effects in a 2D medium to help better understand the phenomena, better parameterize them, and suggest a path to appropriately incorporate them in ground motion prediction equations and building design codes. After the introduction in Chapter 1, I present the results in three main parts as follows:

In Chapter 2, we perform an extensive parametric study on the characteristics of surface ground motion associated with basin effects. We use an elastic idealized-shaped medium subjected to vertically propagating SV plane waves and examine the effects of basin geometry and material properties. We specifically study the effects of four dimensionless parameters, the width-to-depth (aspect) ratio, the rock-to-soil material contrast, a dimensionless frequency that quantifies the depth of the basin relative to the dominant incident wavelength, and a dimensionless distance that quantifies the distance of the basin edges relative to the dominant wavelength. Our results show that basin effects can be reasonably characterized using at least three independent parameters, each of which can significantly alter the resultant ground motion. To demonstrate the application of dimensional analysis applied here, we investigate the response of the Kathmandu Valley during the 2015 M_w 7.8 Gorkha Earthquake in Nepal using an idealized basin geometry and soil properties. Our results show that a simplified model can capture notable ground motion characteristics associated with basin effects.

Chapter 3 uses the identified parameters from the previous chapter to estimate surface acceleration time-series given earthquake frequency content, basin geometry and material properties, and location inside a basin. This is of practical use when the amount of available data is limited or the fast estimation of time-series is desirable. For that, we train a neural network to estimate surface ground acceleration time-series across a basin. Three input parameters are needed for the estimation: basin-to-bedrock shear wave velocity ratio, aspect ratio of the basin, and dimensionless location. These parameters define an idealized-shaped basin and the location at which the time-series are to be computed. It will be shown that

the model performs with high accuracy in comparison to the result of a full-fidelity Finite Element (FE) simulation (ground truth) and generalizes well for input parameters outside of the training set. Moreover, we will also use the model for the case of Kathmandu Valley, Nepal, during the 2015 $M_w 7.8$ Gorkha earthquake and compare the results of NN versus recordings of the mainshock, similarly to Chapter 2.

Once we have studied basin behavior in a homogeneous case in previous chapters, we focus on material representation inside a basin in Chapter 4. Here, we study basin effects for the cases where high-frequency response and realistic material representation are desirable. However, the lack of sufficient information about the material properties and stratigraphy of a basin prevents accurate simulation of the phenomena. To do that, we perform a stochastic analysis using the Monte Carlo technique, where a random field represents basin material. Similarly to the previous chapters, we use a 2D FE model with an idealized basin subjected to vertically propagating SV plane waves and investigate the spatial variation of surface ground motion (SGM) associated with basin effects by assuming different realizations of the correlated random field. We then study various correlation lengths, coefficients of variations, and autocorrelation functions to evaluate their contribution to SGM. We show that the coefficient of variation is the most influential parameter on SGM, followed by correlation lengths and type of autocorrelation function. Increasing the coefficient of variation not only affects the mean surface amplification, but also results in a dramatic change in the standard deviation. Correlation lengths and autocorrelation functions, on the other hand, are of less importance for the cases we examine in this study.

Published and In-preparation Contributions

P. Ayoubi and D. Asimaki. Monte Carlo simulation to study the spatial variation of ground motion associated with basin effects. *In preparation*, 2022.
P.A. performed all data analysis, model development, numerical simulations, produced all figures, and wrote most of the manuscript.

P. Ayoubi, D. Asimaki, and K. Mohammadi. Basin effects in strong ground motion: A case study from the 2015 Gorkha, Nepal earthquake. *Geotechnical Earthquake Engineering and Soil Dynamics V, Austin, TX*, 1(1):288–296, 2018. doi: 10.1061/9780784481462.028.
P.A. performed all data analysis, model development, numerical simulations, produced all figures, and wrote most of the manuscript.

P. Ayoubi, D. Asimaki, M. Stupazzini, and I. Mazzieri. Three-dimensional nonlinear amplification of the Kathmandu Basin sediments during the 2015 mw 7.8 Gorkha earthquake. *VII International Conference on Earthquake Geotechnical Engineering*, 2019. doi: 10.1201/9780429031274.
P.A. performed all data analysis, model development, numerical simulations, produced all figures, and wrote most of the manuscript.

P. Ayoubi, E. Seylabi, and D. Asimaki. Geotechnical site characterization via deep neural networks: Recovering the shear wave velocity profile of layered soils. *Neurips - Machine Learning and the Physical Sciences Workshop*, 2020. doi: 10.31224/osf.io/jcw3t.
P.A. performed all data analysis, model development, numerical simulations, trained the model, produced all figures, and wrote most of the manuscript.

P. Ayoubi, Kami Mohammadi, and D. Asimaki. A systematic analysis of basin effects on surface ground motion. *Soil Dynamics and Earthquake Engineering*, 141, 2021. doi: 10.1016/j.soildyn.2020.106490.
P.A. performed all data analysis, model development, numerical simulations, produced all figures, and wrote most of the manuscript.

P. Ayoubi, K. Azizzadehneshali, K. Mohammadi, K. Nguyen, and D. Asimaki. Time-series estimation using neural network: Application of basin effects. *In preparation*, 2022.
P.A. performed all data analysis, model development, numerical simulations, trained the model, produced all figures, and wrote most of the manuscript.

Table of Contents

List of Illustrations

List of Tables

Chapter 1

Introduction

This chapter provides background information about basin effects and builds a foundation for future chapters. We first define basin effects and explain the underlying physics by decomposing the phenomena into its building components, namely material contrast and basin edge effects. At the end of this chapter, we present the goal of this research and the overall structure of the thesis.

Contents of this chapter

1.1 Physics of Basin Effects

As shown in Figure 1.1, three aspects govern an earthquake-induced surface ground motion in a basin scenario. Source represents the nucleation and characteristics of the rupture. Path demonstrates waves scattering and attenuation as they propagate in the crust and before reaching the surface. Finally, the basin represents a bowl-shaped shallow soil close to the ground surface. Basin effects are the subject of this study, where we investigate how a basin's presence impacts the surface ground motion. Basin effects are a sub-category of local site effects. They refer to trapped and reverberating earthquake waves in soft sedimentary deposits overlying convex depressions of basement bedrock and significantly alter the frequency content, amplitude, and duration of seismic waves. They have played an essential role during past earthquakes, such as the M_w 8.0 1985 Michoácan, Mexico, M_w 6.9 1995 Kobe, Japan, and M_w 7.8 2015 Gorkha, Nepal (Kawase and Aki [1989], Pitarka and Irikura [1996], Kawase [1996], Asimaki et al. [2017]).

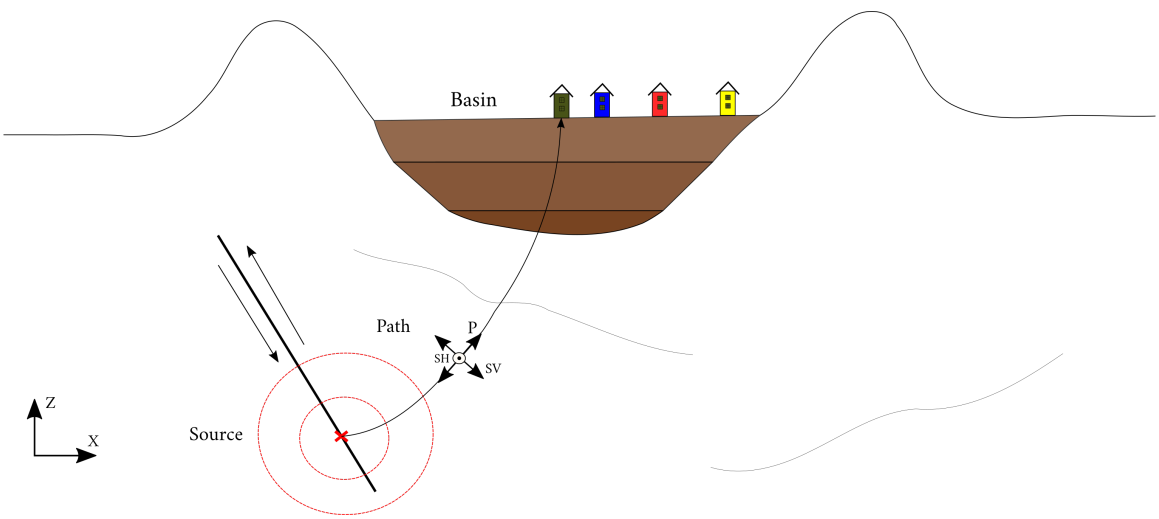

Figure 1.1: Three aspects that govern earthquake ground motions: source, path, and site. Basin shows the near-surface geology in many areas where a sedimentary deposit is located on top of the bedrock.

Basin effects arise from a combination of (a) trapping of seismic waves due to impedance contrast and consecutive reverberations of seismic energy (Spudich and Iida [1993]), and (b) focusing effects at the edges of a basin, frequently referred to as *basin-edge effects* (Graves et al. [1998]). Similar to 1D site response, soil-to-rock impedance contrast plays a vital role in the amount of trapped seismic energy in a basin and, thus, in seismic motion's amplification and elongation.

One can readily quantify the role of material contrast by solving the three-dimensional wave equation (Eq. 1.1) for incidence on a two-material interface (see Figure 1.2):

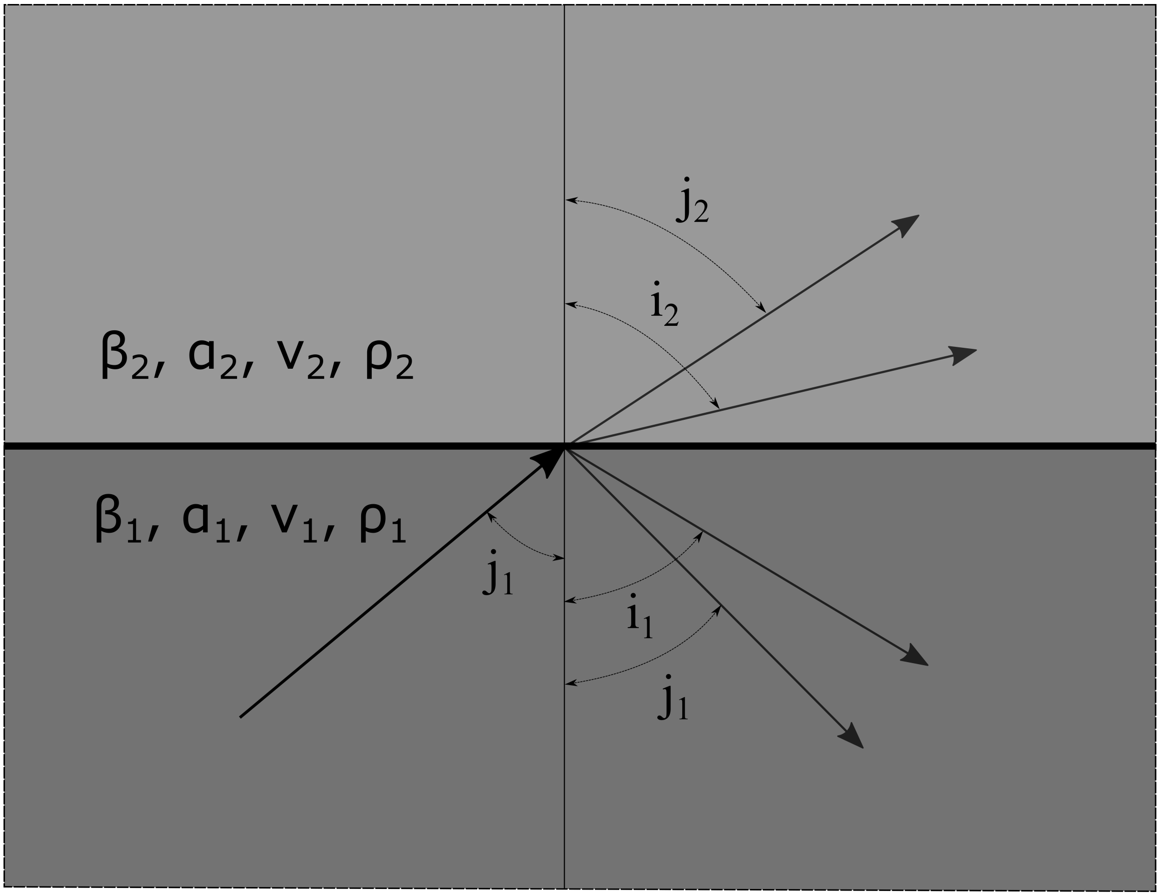

Figure 1.2: Schematic representation of reflection and transmission of a plane SV wave incident with angle α on a plane boundary of two materials.

$$(\lambda + \mu)u_{j,ji} + \mu u_{i,jj} + F_i = \rho \frac{\partial^2 u_i}{\partial t^2} \quad i, j = 1, 2, 3 \tag{1.1}$$

in which ρ is the density of a medium, F_i is the body force, u_i are the components of the displacement vector, and λ and μ are Lame's constants.

Assuming the upcoming SV wave is $S(\cos j_1, 0, \sin j_1) \exp\left\{[i\omega(px - \frac{\cos j_1}{\beta_1} z - t)]\right\}$, transmitted and reflected S waves are: $S(\cos j_2, 0, \sin j_2) T_s \exp\left\{i\omega(px - \frac{\cos j_2}{\beta_2} z - t)\right\}$ and $S(\cos j_1, 0, -\sin j_1) R_s \exp\left\{i\omega(px + \frac{\cos j_1}{\beta_1} z - t)\right\}$, respectively. Moreover, transmitted and reflected P waves are $S(\sin i_2, 0, -\cos i_2) T_p \exp\left\{i\omega(px - \frac{\cos i_2}{\alpha_2} z - t)\right\}$ and $S(\sin i_1, 0, \cos i_1) R_p \exp\left\{i\omega(px + \frac{\cos i_1}{\alpha_1} z - t)\right\}$, respectively. In these equations, T_p, T_s, R_p, and R_s are the amplitude of transmitted P-wave, transmitted S-wave, reflected P-wave, and reflected S-wave amplitudes, respectively. By satisfying traction equilibrium and displacement compatibility conditions at the material interface, reflection and transmission coefficients can be computed as outlined in detail in Aki and Richards [2002]:

$$T_p = 2\rho_1 \frac{\cos(j_1)}{\beta_1} H p \beta_1 / (\alpha_2 D) \tag{1.2}$$

$$T_s = 2\rho_1 \frac{\cos(j_1)}{\beta_1} E \beta_1 / (\beta_2 D) \tag{1.3}$$

$$R_p = 2 \frac{\cos j_1}{\beta_1} \left(ac + bd \frac{\cos i_2}{\alpha_2} \frac{\cos j_2}{\beta_2}\right) p \beta_1 / (\alpha_1 D) \tag{1.4}$$

$$R_s = \frac{1}{D}\left((b \frac{\cos(j_2)}{\beta_2} - c \frac{\cos(j_2)}{\beta_1}) E - (a + d \frac{\cos(i_2)}{\alpha_2} \frac{\cos(j_1)}{\beta_1}) H p^2\right). \tag{1.5}$$

P is the slowness of medium 1, which is given by:

$$p = \sin \phi_{j_1} / \beta_1 \tag{1.6}$$

and a, b, c, d, E, F, G, H, and D are constants (reader should refer to Aki and Richards [2002] for explanation of constants). To show the variation of the reflection and transmission coefficients as a function of rock-to-soil shear wave velocity contrast, Figure 1.3 plots the displacement amplification coefficients for the two welded half-spaces of Figure 1.2 subjected to a plane SV wave. As can be seen, by increasing the material contrast while keeping all other parameters constant, the amplitude of the reflected S-wave increases, and the amplitude of the transmitted S-wave decreases. In addition, P-waves are generated at the interface due to mode conversion. Such amplification and mode conversion effects are one aspect of basin effects. In a basin scenario, the softer and stiffer materials are basin and bedrock, respectively, propagating from a soft medium toward a stiffer medium results in more reflection as the impedance contrast increases.

On the other hand, basin-edge effects result from energy focusing and interference of seismic waves in the wedge-shaped edges. The constructive interference between direct waves and edge-generated surface waves is schematically depicted in Figure 1.4: when a vertically propagating plane SV wave incites on a sloped subsurface interface between bedrock and sediment, it generates a set of reflected and refracted P and S waves. Focusing on the latter, Figure 1.4 illustrates the interference of SV direct arrivals, the reflections of SV waves from the bedrock-sediment interface, and the transversely propagating surface waves, which show a complex interaction of wave components that frequently exacerbates the intensity of the wavefield in a basin.

Figure 1.5 shows the combined effects of impedance contrast and basin-edge surface wave generation, in the form of simulated particle motion on the ground surface of a 20° dipping layer, which is subjected to a unit amplitude vertically propagating SV plane wave of Ricker

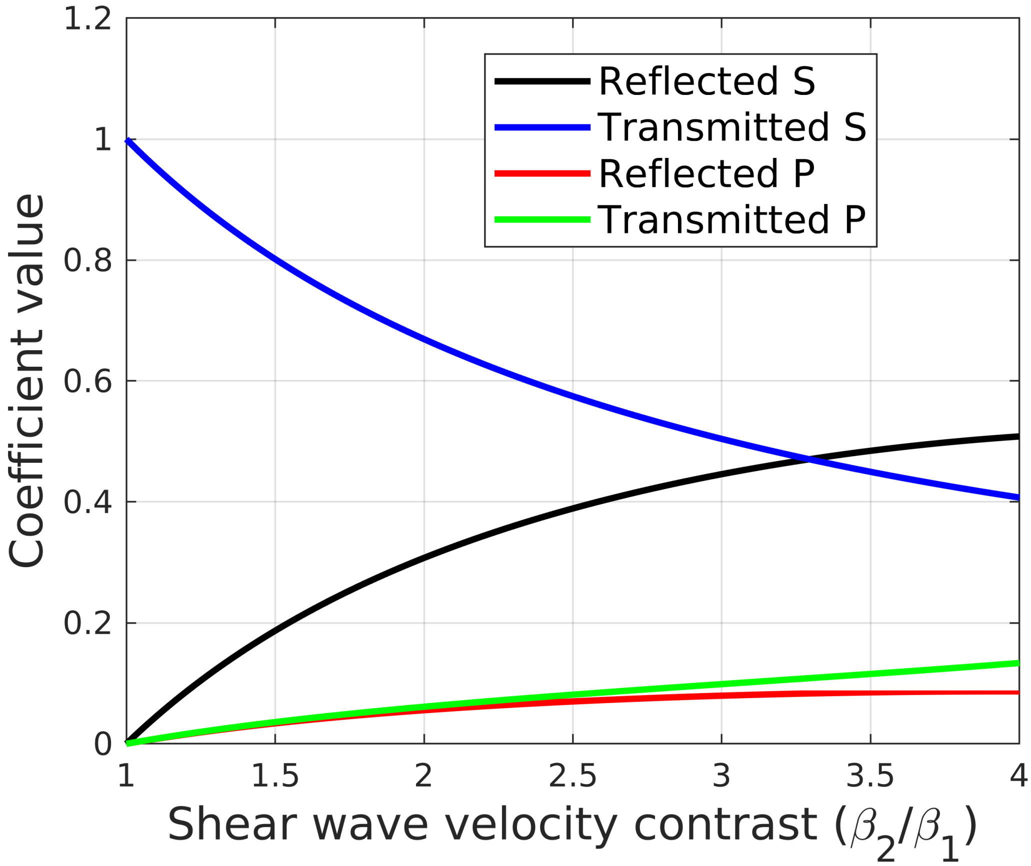

Figure 1.3: Variation of displacement reflection and transmission coefficients by changing material contrast. This figure shows the case of incident angle $\alpha = 5^o$. Different patterns may be observed for higher angles. With reference to Figure 1.2, medium 1 has softer material.

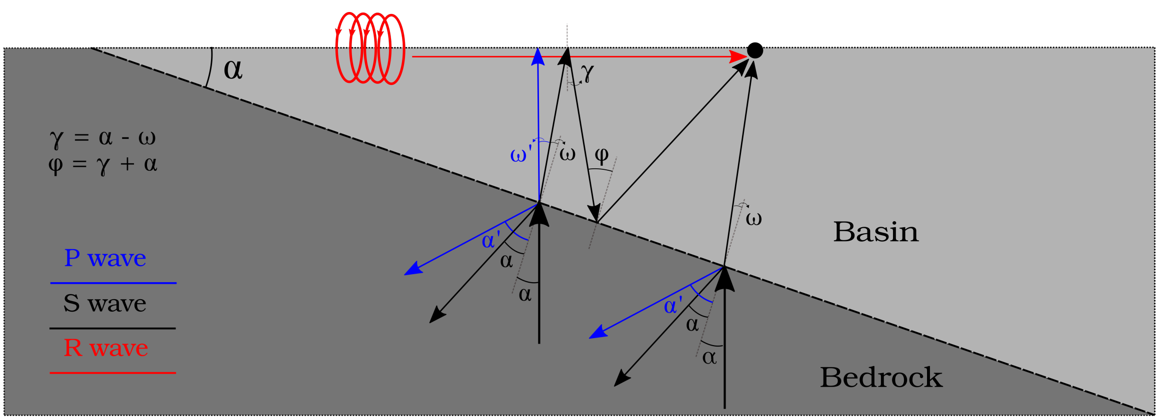

Figure 1.4: Schematic view of the coupled effect of material contrast and basin edge. P, S and R waves stand for Primary, Shear and Rayleigh waves. β_1 and α_1 are S and P wave velocities in the dipping layer, and β_2 and α_2 are the ones for bedrock. In this figure, $\omega = \arcsin \frac{\beta_1}{\beta_2} \sin\alpha$, $\omega' = \arcsin \frac{\alpha_1}{\beta_2} \sin\alpha$ and $\alpha' = \arcsin \frac{\alpha_2}{\beta_2} \sin\alpha$. Other parameters and angles are shown in the figure.

type. Points 1 to 5 lie on the rock outcrop, while points 6 to 16 lie on the surface of the sedimentary dipping layer. Point 6 is located precisely at the tip of the $20°$ wedge. As can be seen, the basin edge introduces a very complex particle motion compared to the frequently assumed horizontally stratified medium, which does not generate any vertical component. While its effects are evident on the rock outcrop motion in the vicinity of the wedge tip, it predominantly impacts the particles' motion inside the dipping layer. Note that while the incident motion was purely horizontally polarized, the ground motion has a significant vertical component arising from mode conversion, as well as very pronounced spatial variability, both of which are likely to affect distributed systems and long components of infrastructure such as pipelines.

1.2 Current Practice and Goals of This Study

As the title of this thesis suggests, the goal is to discuss basin effects parameterization and modeling. As for parameterization, we examine how we are able to incorporate basin effects in seismic hazard analysis better. For modeling, we explain approaches through which one is able to increase the accuracy of a basin simulation.

From the parameterization perspective, ground motion prediction equations and design codes acknowledge the importance of basin effects. However, lack of sufficient data, namely geometry, stratigraphy, and material properties, is a setback to fully incorporate basin effects. In an empirical ground motion analysis, basin effects are generally taken into account using V_{s30} (the travel-time based average of the shear wave velocity of the top $30\,m$). Most of the empirical studies ignore the impact of basin depth on long-period response of surface response with some exceptions, for example Abrahamson et al. [2014], Boore et al. [2014], Campbell and Bozorgnia [2014], and Chiou and Youngs [2014] from NGA-West ground motion models. These studies include a measure of depth by introducing a Z_x parameter which shows the depth at which the shear wave velocity reaches $x\ {}^{km}/_{s}$. The most common ones are Z_1 and $Z_{2.5}$, which show the depth that shear wave velocity reaches $1\ {}^{km}/_{s}$ and $2.5\ {}^{km}/_{s}$, respectively.

In a best-case scenario, two parameters (V_{s30} and Z_x) are used to quantify a basin's response. One important missing component is the distance from basin edges. In reality, the slow variation of basin depth results in a wedge-like outskirt. This introduces edge-induced surface waves and results in an extensive wave interference inside a basin. By using only V_{s30} and Z_x (which in theory represent a $1D$ column including a layer over halfspace), one could represent different basin geometries. For example, consider two basins. One has a total width of W and a maximum depth of D, and the other one has a width of $4 \times W$

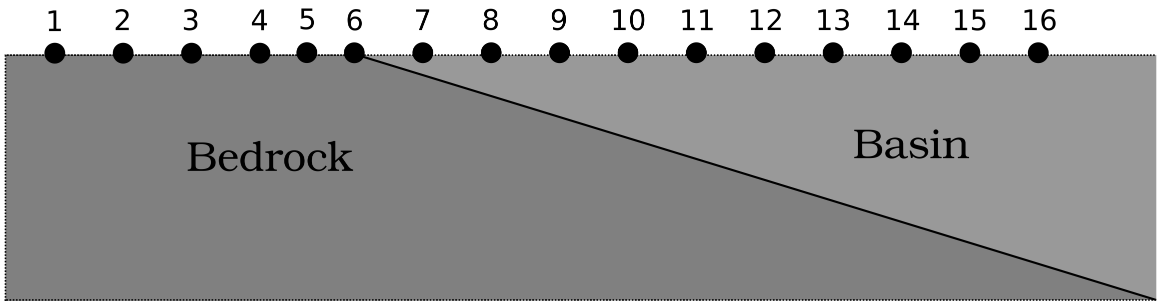

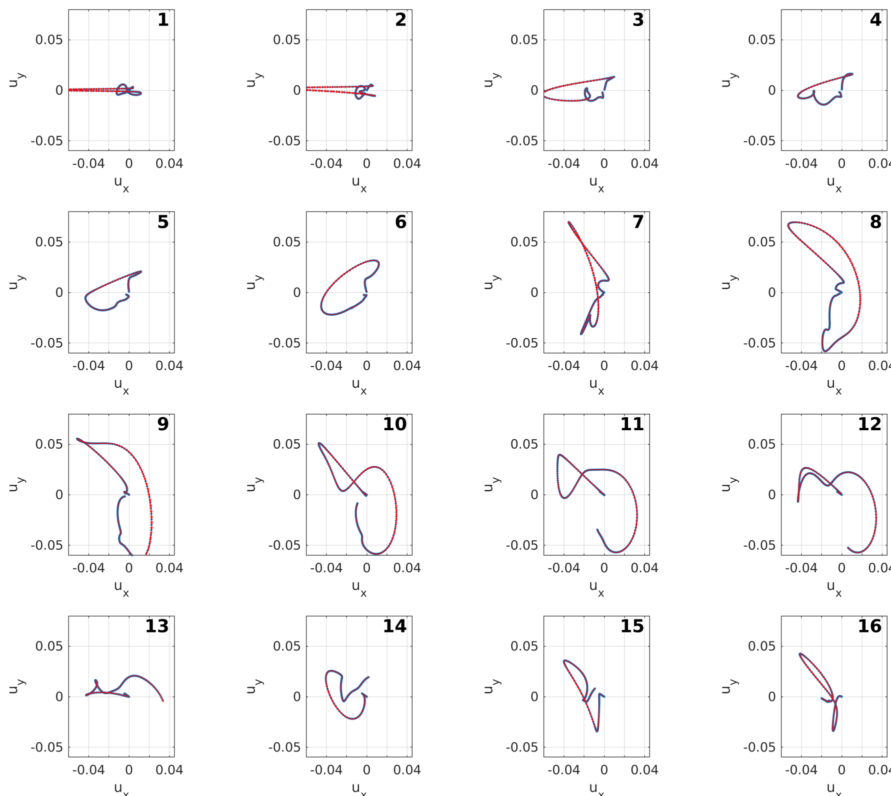

Figure 1.5: Particle motion diagram for a set of stations close to the tip of a dipping layer of $20°$. An example is shown for material velocity contrast 2 and unit amplitude plane Ricker SV wave with a dominant frequency of 1 Hz.

and a maximum depth of D. At a point p, both could have the same V_{s30} and Z_x while the wavefield might be significantly different between the two. Therefore, there is not a one-to-one mapping between (V_{s30}, Z_x) to the corresponding basin response. In addition, such a parameterization ignores the frequency content of incoming seismic wave, which would change basin response. In an empirical analysis, this is resolved by using a reference site. However, selecting a reference site through which the empirical functional forms are calibrated is not easy. Most of the GMPEs are well-calibrated for soft rock (shear wave velocity of up to 800 m/s) (Pilz et al. [2021]), which restricts the generalizability of the developed functional forms. In sum, the current practice has two main shortcomings that Chapter 2 of this thesis will address: 1) most of the models are calibrated based on a fixed rock shear wave velocity value that reduces their generalizability. Through dimensional analysis (Buckingham [1914]), one is able to develop a general mapping that does not depend on a reference site. 2) The use of two parameters that are correlated (V_{s30} and Z_x) may reduce the accuracy of the amplification factor. To properly incorporate basin effects, a measure of basin geometry or distance from the corner needs to be considered.

From modeling perspective, basin simulations can be done for a specific location independent of GMPEs or design codes. A $1D$ site response usually replaces $2D$ basin analysis in such cases. This means that instead of a $2D$ domain, an oversimplified $1D$ homogeneous material or a layered profile is assumed to represent basin material. While this approach may work in some cases (middle of a very shallow and long basins), neglecting the importance of basin edges and material variations could result in over- or under-prediction of surface response. This oversimplification often arises from the computational cost of $2D$ simulations and/or unavailability of detailed material properties of soil, both of which can be addressed.

Once the basin geometry is correctly defined using the information in Chapter 2, there are two possible directions to perform numerical simulations: 1) to assume a homogeneous medium similar to what is being done in Chapter 2, or 2) to assume a heterogeneous basin. For the case of homogeneous basin, the computational cost is the main issue. However, one can leverage statistical approaches to reduce the computational time significantly. In Chapter 3, a procedure will be detailed that utilizes the power of deep Neural Networks to learn a basin's response given few dimensionless parameters as input. The trained model is able to return basin surface acceleration at any point in a fraction of second.

On the other hand, for the case of heterogeneous basins, the main problem is a way to properly account for basin material properties in situations that data is unavailable. In Chapter 4, a Monte Carlo (MC)-based approach is presented as an alternative to address the problem. In this technique, by generating a sufficient number of realizations, one can perform a stochastic analysis that quantifies basin response uncertainty accurately. The method will be able to not only produce the expected value of the response but also it returns the standard error. Note that the computational cost still remains an issue in this case, but is out of scope of this thesis. In Chapter 5, a series of recommendations will be made to lay out a plan to utilize statistical methods and machine learning to address this shortcoming as well.

1.3 Structure of Thesis

For the rest of this thesis, we discuss the following subjects:

Chapter 2 includes a literature review and a discussion about the results of a parametric study to examine the effects of different parameters on surface ground motion in a basin subjected to dynamic loading. We will parameterize an idealized-shaped basin using dimensionless parameters. The goal is to prioritize the parameters and make suggestions on incorporating basin effects in GMPEs, design codes, among others.

Chapter 3 uses the results of Chapter 2 to build a neural network model and predict the surface ground acceleration time-series in a basin. The network estimates the time-series of acceleration at a location inside a basin using three parameters. The computational cost of the model is negligible compared to a full-fidelity finite element simulation. Such a model is valuable for cases when a fast estimation of time-series is desirable, such as early warning systems.

Chapter 4 studies basin effects from the perspective of probability finite element simulations, where a correlated random field represents basin material. In a deterministic scenario, the basin geometry and material properties can impact seismic waves up to a particular frequency. However, there are cases where the response of a basin in a high-frequency range is of interest, but the shear wave velocity profile is not well resolved. Monte Carlo technique and probabilistic FEM are valuable alternatives to a deterministic simulation in such a scenario and will be addressed in this chapter.

Chapter 5 presents the conclusion of this study and suggests future directions.

Chapter 2

A Systematic Analysis of Basin Effects on Surface Ground Motion

In this chapter, we perform an extensive parametric study on the characteristics of surface ground motion associated with basin effects using finite element simulations. We use an elastic medium subjected to vertically propagating SV plane waves and utilize idealized basin shapes to examine the impact of basin geometry and material properties. We specifically study the effects of four dimensionless parameters, the width-to-depth (aspect) ratio, the rock-to-soil material contrast, a dimensionless frequency that quantifies the depth of the basin relative to the dominant incident wavelength, and a dimensionless distance quantifying the distance of the basin edges compared to the dominant wavelength. Our results show that basin effects can be reasonably characterized using at least three independent parameters, each of which can significantly alter the resultant ground motion. To demonstrate the application of dimensional analysis applied here, we investigate the response of the Kathmandu Valley during 2015 M_w 7.8 Gorkha Earthquake in Nepal using an idealized basin geometry and soil properties. Our results show that a simplified model can capture notable characteristics of the ground motion associated with basin effects, suggesting that such studies can provide valuable insights relevant to the parameterization of basin effects in GMPEs and design code provisions.

The contents of this chapter are adapted from our publication Ayoubi et al. [2021]:

Contents of this chapter

2.1 Introduction

Studies on basin effects date back half a century and have produced several analytical/semi-analytical and numerical results. Researchers studied the out-of-plane (SH wave) problem first due to its scalar nature and its simplicity. Among others, seminal was the work by Aki and Larner [1970], who derived a method (Aki-Larner method) and found a strong lateral interference of waves in a layer over bedrock medium, which is absent in the solution of flat layer approximation (FLA, assuming horizontally stratified media). Parallel to Aki and Larner [1970], Boore [1970] studied an irregularly shaped layer over half-space for a transient input motion using FDM. They observed a significant Love wave perturbation in the vicinity of the transition zone where both the amplitude and phase of the wavefield are affected. Also, it was later shown that Aki-Larner and FDM methods are in good agreement (Boore et al. [1971]). At the same time, the FLA could not adequately capture the late arrivals of strong reverberations due to the lateral interference caused by the non-planar basin shape. Shortly after, Trifunac [1971] and Wong and Trifunac [1974] used the wave expansion method to devise a semi-analytical solution for semi-cylindrical and semi-elliptical basins. They confirmed the inadequacy of FLA in complex geometries and found that increasing the frequency of incident waves would complicate the wave interference in basins, a phenomenon that can also occur due to the change in incident angle.

Studies on the more complex SV-P (in-plane) problems became more prevalent in the following decade. Bard and Bouchon [1980] studied a cosine-shaped basin subjected to P and SV incident motions. For wide basins with high-velocity contrast, they observed a clear generation of Rayleigh waves and showed that higher Rayleigh modes were excited by SV incident wave because of the lower value of shear wave velocity compared to the compressional wave. Moreover, they observed that the maximum amplification corresponds to the direct wave arrival for P-waves and the Rayleigh wave generation for S-waves. Later, Dravinski [1982] examined the scattering of elastic waves by an alluvial valley of elliptical shape subjected to harmonic in-plane and out-of-plane incident motions using the boundary integral (BI) method. They noticed that the effects of incident motion frequency and basin depth were interdependent and concluded that the SH incident wavefield is less sensitive to basin depth than P and SV waves at the low-frequency regime. In addition, for Rayleigh wave incidence (as would be the case, e.g., for a basin located next to a surface topographic), they showed a comparable surface displacement amplification to P and SV incidences.

The M_w 8.1 1985 Michoàcan, Mexico Earthquake was a turning point in recognizing the significance of basin effects. Despite the considerable distance ($\geq$ 350km) from the epicenter, Mexico City experienced disproportionately large amplification and a very long shaking duration. Many studies were prompted in the wake of the event and were mainly focused on idealized 2D models of the basin (Bard et al. [1988], Campillo et al. [1988], Kawase and Aki [1989]). The ensemble of studies attributed the observed amplification to basin-edge effects and reverberation of earthquake waves in the sedimentary deposits. The consensus was not as strong for the observed ground motion duration, and some studies attributed it to 3D effects (Chávez-Garcia and Bard [1994]) not accounted for in 2D models. It was recently shown that the long duration could be attributed to longer period waves reverberating in the deeper sediments of the basin not previously accounted for (Cruz-Atienza et al. [2016]).

Following the 1985 Mexico City Earthquake, 3D models were brought forth to study basin effects in a more realistic setting by simultaneously solving the in-plane and out-of-plane components (Sánchez-Sesma et al. [1993], Battan and Narayan [2015]). This includes both simplified geometries (Sánchez-Sesma and Luzón [1995]) and realistic basin configurations (Olsen et al. [1995], Lee et al. [2008]). Horike et al. [1990] studied 3D irregularly layered subsurface structures and observed 3D effects, namely localization, rapid growth, and strong spatial variability of surface waves. Comparing 2D simulations confirmed that idealized 2D models could not fully reproduce the true amplitude and duration of surface motion. Pitarka et al. [1998] performed near-fault ground motion simulations with kinematic source models of the 1995 M_w 6.9 Hyogo-ken Nanbu (Kobe) earthquake and showed that the constructive interference between source and basin was the main reason for the catastrophic consequences of the event. With the increase in stratigraphy and material information in some regions, researchers can better capture sedimentary deposits' responses during a seismic event. Rodgers et al. [2019] performed a broadband (0-5 Hz) 3D simulation of the Hayward fault in California and showed that such high-fidelity simulations could produce earthquake ground motions consistent with the empirical data. They also observed a site-specific surface motion and concluded that fault dip and material heterogeneity play an important role in site response.

In the last twenty years, spectral and pseudo-spectral methods have become prevalent for regional-scale simulations of basin effects as a computationally efficient and highly accurate method (Komatitsch et al. [2004], Di-Giulio et al. [2016], Hallier et al. [2008], Faccioli et al. [1997], Komatitsch and Vilotte [1998]). Stupazzini et al. [2009] used 3D SEM to study basin effects in the Grenoble valley. In addition to basin amplification, they also considered source effects and sediment pseudo-nonlinear response. They found that the hypocenter location and directivity play an influential role on surface ground motion. Moreover, the radiation mechanism and the relative location of the Grenoble valley to the fault strike played a significant role on the observed ground motion.

Recently, the focus has been on large-scale simulation case studies (Wei et al. [2018], Esmaeilzadeh and Motazedian [2019]) and some idealized-shaped basin parametric analyses (Battan and Narayan [2015], Gelagoti et al. [2010, 2012]). The daunting computational cost and input parameters required to capture basin effects (using realistic source models, crustal structures, and near-surface effects) have hindered integrating these effects in GMPEs and engineering design practice. Instead, the engineering community still relies gravely on 1D site response models that are not appropriate to capture basin edge physics when relevant. Although it has been shown in the past (Pilz and Cotton [2019]), and design codes (such as Eurocode 8 (CERN [2004])) have acknowledged the importance of local site effects, it is not yet properly taken into account. Currently, GMPEs take local site effects into account by utilizing V_{s30} and Z_1, ignoring the important role basin-edge effects have played in the previous earthquake (such as Adams [2000]). Such an approach would completely discard the mode conversion and strong spatial variability at the corner of a basin. Different approaches have been proposed to bridge this gap, among which is using aggravation factors. This method claims that one may multiply the 1D site response by a factor to approximately take basin effects into account for seismic analysis (Riga et al. [2016, 2018], Moczo et al. [2018]).

This chapter uses dimensional analysis to conduct a comprehensive numerical parametric study of 2D idealized basin geometries and material properties. Our goal is to identify and prioritize parameters that govern basin effects, which could help parameterize basin effects in ground motion models (GMM) and engineering design provisions. We wish to represent basin-edge effects better, and their essential contribution in basin surface response since although using V_{s30} and Z_1 is the standard practice to address local site effects, it is a more accurate way of incorporating the basin-edge effect is essential. The chapter is structured as follows: After verifying our numerical toolbox, we examine the behavior of semi-elliptical and half-cosine basins by varying the material properties, geometrical configuration, and input motion characteristics. To make the results applicable for general basin configurations, we present them in dimensionless form. Finally, to test our proposed parameterization, we simulate the Kathmandu Valley, Nepal, during the 2015 Gorkha Earthquake. Our simplified results compare favorably to long-period observations, suggesting that simple basin geometries could potentially be used to investigate and parameterize key ground motion characteristics associated with basin effects.

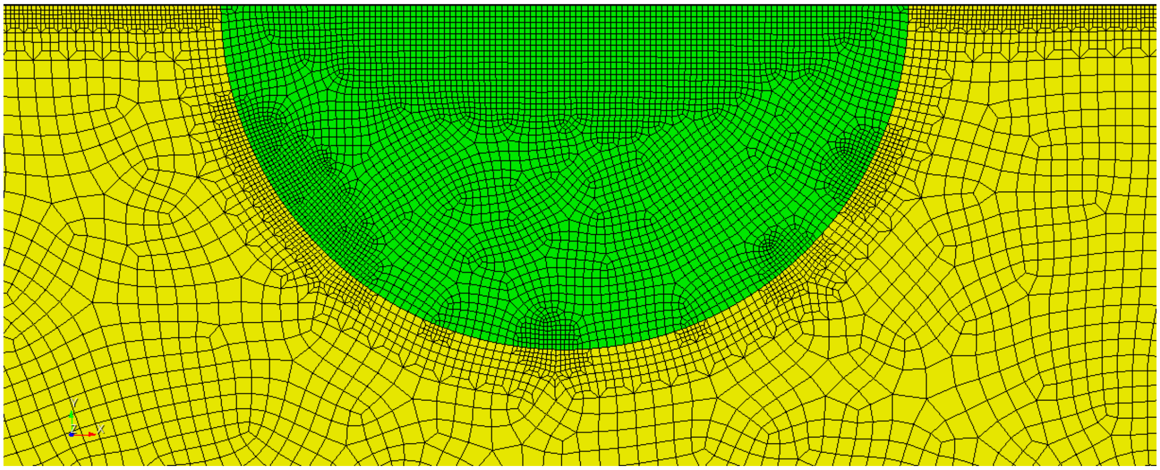

Figure 2.1: An example of discretized FE domain. The green area shows the basin and the yellow represents the bedrock. The domain is discretized using quad elements.

2.2 Description of Numerical Model

The idealized numerical model we used in this study is a 2D basin consisting of two elastic, isotropic, and homogeneous materials for bedrock and basin. We performed an analysis of wave propagation in a basin over halfspace using OpenSees, a FEM code that can solve the wave equation in a heterogeneous medium subjected to initial and boundary conditions using an implicit scheme (McKenna et al. [2000]). We discretized the numerical model by requiring 12 quad elements per shortest propagating wavelength to resolve the frequency range of interest, based on the dominant frequency of an incoming wave (Figure 2.1).

Free-field boundary conditions were placed along the side boundaries, at a distance greater than two times the dominant incident wavelength (λ_2, see Figure 2.6) from basin edges. Free-field (FF) boundary condition comprises S- and P-wave absorbing elements (also known as "Lysmer dashpots" (Lysmer and Kuhlemeyer [1969])), and free-field equivalent forces corresponding to 1D wave propagation conditions as shown in Figure 2.3 (Cundall et al. [1980]).

The dashpot coefficients for the tangential and perpendicular directions relative to the lateral boundaries, C_s and C_p, are estimated as follows:

$$C_s = \rho v_s \tag{2.1}$$

$$C_p = \rho v_p \tag{2.2}$$

where ρ is the density of the halfspace, and v_s and v_p are the shear and compressional wave velocities of the halfspace, respectively. Successively, the FF effective forces that represent the stress-field for 1D wave propagation conditions were computed as follows:

$$F_x = -(\rho C_p(V_x^m - v_x^{ff}) - \sigma_{xx}^{ff})\Delta A_y \tag{2.3}$$

$$F_y = -(\rho C_s(V_y^m - v_y^{ff}) - \sigma_{xy}^{ff})\Delta A_y \tag{2.4}$$

where F_x and F_y are perpendicular and tangential loads, respectively. V_x^m and V_y^m are nodal velocities in x and y directions computed at each time step during the FE analysis, v_x^{ff} and v_y^{ff} are FF velocities in x and y directions and σ_{xx}^{ff} and σ_{xy}^{ff} are the FF stresses in x and y directions, respectively. The last four quantities are calculated using D'Alembert's method for 1D wave analysis. ΔA_y is the element size in the vertical direction.

For incident motion, we used a unit amplitude vertically propagating plane SV wave of Ricker type (Ricker [1940]) (Figure 2.2, Eq. 2.5). While both SV and SH cases are important on basin surface response, the choice of SV versus SH is mostly due to the surface wave generation at basin corners. Input motion is applied as a shear force at the base of the numerical domain where absorbing boundary conditions (Lysmer dashpots) are prescribed. The force is calculated based on Eq. 2.6 where F_{input} and ΔA_x are input force and element size at the bottom, respectively.

$$Acc(t) = (1 - 2\pi^2 f_0^2 t^2)e^{-\pi^2 f_0^2 t^2} \tag{2.5}$$

$$F_{input} = \rho C_s \Delta A_x \int Acc(t)dt \tag{2.6}$$

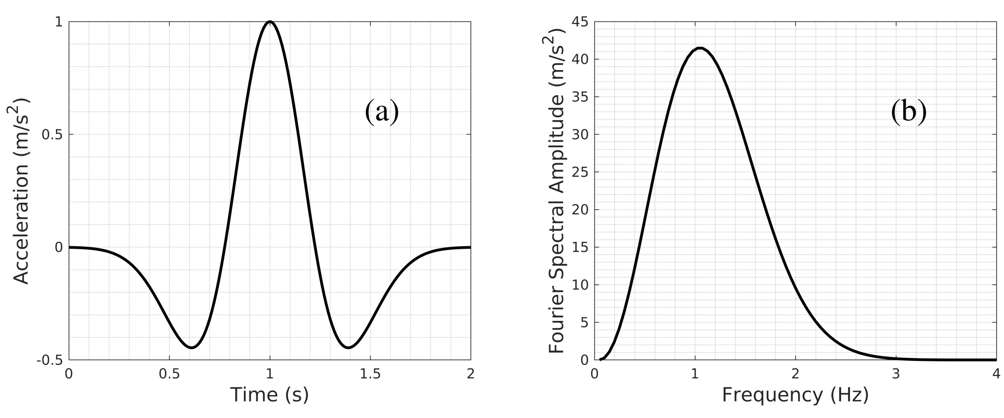

Figure 2.2: Acceleration input time history, a Ricker wavelet in a) time-domain and b) frequency domain.

Synthesizing the above, the vertical side boundaries would ideally respond as 1D columns subjected to vertically propagating shear waves, had there not been a scattered wavefield

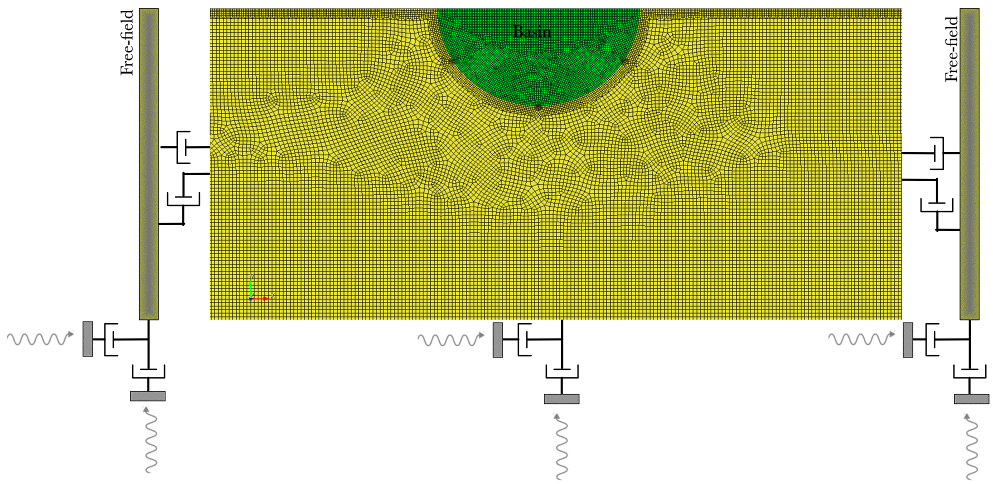

Figure 2.3: Schematic view of the FEM domain and boundary conditions.

(albeit weak in this case) that is leaking from the basin sediments at each reverberation. A schematic view of the numerical domain and prescribed boundary conditions is depicted in Figure 2.3.

2.3 Parametric Analysis

This section investigates the variation of surface ground motion with basin geometry, material properties, and input motion characteristics by performing a parametric study on two idealized configurations, Semi-Elliptical (SE) and Half-Cosine (HC). The SE basin is used as a frequently employed idealization that can easily be parameterized (Wong and Trifunac [1974], Trifunac [1971], Mossessian and Dravinski [1987], Al-Yuncha and Luzón [2000]). It is suitable to study the physics of wave propagation inside a basin by investigating the effect of dimensionless parameters presented later. Moreover, the SE-shaped basin represents cases that the basin corner has a relatively sharp angle, which happens when the fault rupture extends to the surface of the Earth with a sharp angle. The HC basin is a more realistic representation of the basin shape while remaining easy to parameterize for geometric and material properties. Eq. 3.2 gives the mathematical expression of the bedrock-sediment interface depth for an HC basin. Parameters b, D, and a are depicted in Figure 2.6.

$$\begin{cases} b & |x| \leq D/2 \\ \frac{b}{2}[1 + cos(\frac{\pi(x-D/2)}{a})] & D/2 \leq |x| \leq D/2 + a \\ 0 & |x| \geq D/2 + a. \end{cases} \tag{2.7}$$

The dimensionless parameter space for the problem can be derived using Buckingham's π theorem (Buckingham [1914]). For a dynamic problem in elastodynamics, three parameters are needed to define a material. Here, we use v_s (shear wave velocity, denoted β heretofore to avoid parameters with multiple indices), ν (Poisson's ratio), and ρ (density) as representative parameters for each material. In total, we study the effects of six parameters, namely β_1, ν_1 and ρ_1 of the basin sediments, and β_2, ν_2 and ρ_2 of the bedrock. In addition, a, b and $D + 2a$ are used to define geometry of a basin. Finally, f_0, the dominant frequency of input motion, is used to represent the excitation. Given the ten parameters and three characteristic parameters (length ($[L] = b$), mass ($[M] = \rho_2 b^3$) and time ($[T] = b/\beta_1$)) of the problem, Buckingham's theorem yields 7 dimensionless parameters ($\pi_1 - \pi_7$) defined as follows:

$$\pi_1 = \nu_1,\ \pi_2 = \nu_2,\ \pi_3 = \frac{a}{b},\ \pi_4 = \frac{\beta_2}{\beta_1},\ \pi_5 = \frac{f_0 b}{\beta_1},$$
$$\pi_6 = \frac{\rho_1}{\rho_2},\ \pi_7' = \frac{D+2a}{\lambda_1} = \frac{(D+2a)f_0}{\beta_1}. \tag{2.8}$$

Note that π_7' is derived by multiplying $\pi_7 = (D + 2a)/b$ and π_5. In terms of order of magnitude, the dominant dimensionless parameters of our problem are π_3, π_4, π_5, and π_7'. To reduce the computational cost, we perform the parametric study only for these four parameters and later show that the effects of π_1, π_2, and π_6 are negligible for the problem in hand. Unless otherwise stated, we assume $\pi_1 = 0.33$, $\pi_2 = 0.33$ and $\pi_6 = 1$, as per Kawase and Aki [1989].

In the following sections, we first present two verification examples of our numerical model and then examine the contribution of the dimensionless parameters' contribution. For clarity, we refer to π_3 as Aspect Ratio (AR), defined as a over b (see Figure 2.6); to π_4 as ζ, the dimensionless width of the basin defined as $(D + 2a)/\lambda_1$, where λ_1 is the dominant wavelength in the sediments defined as β_1/f_0; and to π_5 as η, the dimensionless frequency. To compare the various realizations of the parametric space, we normalize the peak acceleration amplitude on the ground surface by the peak amplitude on a rock outcrop referred to as amplification factor (AF). In addition, we utilize seismogram synthetics (SS) on the ground surface and vector field snapshots to represent the spatiotemporal variation of the wavefield.

2.3.1 Numerical Model Verification

We present two verification examples of our numerical models: (a) a semi-circular basin from Mossessian and Dravinski [1987], and (b) a trapezoidal basin from Kawase and Aki [1989]. Models are presented using dimensionless parameters explained earlier.

2.3.1.1 Semi-circular Basin: Mossessian & Dravinski (1987)

The first is a semi-circular basin, with geometry characteristics and material properties described in Mossessian and Dravinski [1987] and listed in Table 2.1. Mossessian & Dravinski used the indirect boundary integral method to compute the steady-state basin response and reported the Amplification Factor (AF) along the surface as the peak ground surface spectral amplitude normalized by the peak incident spectral amplitude (U_x/U_x^{inc}). Figure 2.4 compares the results by Mossessian & Dravinski to those of this study. To compare our synthetic time-domain results with the steady-state basin response of Mossessian and Dravinski [1987], we extracted the steady-state part of the ground surface displacement by neglecting the first few cycles of time-series and considered the rest for further processing. We then applied the Fast Fourier Transform (FFT) to the computed time-series and finally normalized it by the peak spectral amplitude of the incident motion. The comparison depicted in Figure 2.4 shows a very satisfactory agreement between the two studies.

Parameters						
π_1	π_2	π_3	π_4	π_5	π_6	π_7
0.333	0.333	1	2	0.5	0.66	1

Table 2.1: Material, geometry, and incident motion parameters for semi-circular basin in Mossessian and Dravinski [1987].

2.3.1.2 Trapezoidal Basin: Kawase & Aki (1989)

The second verification example is the trapezoidal basin response published by Kawase and Aki [1989]. Table 2.2 indicates the parameters we used to simulate this example. Figure 2.5 shows an excellent agreement of the two studies in the spatiotemporal domain.

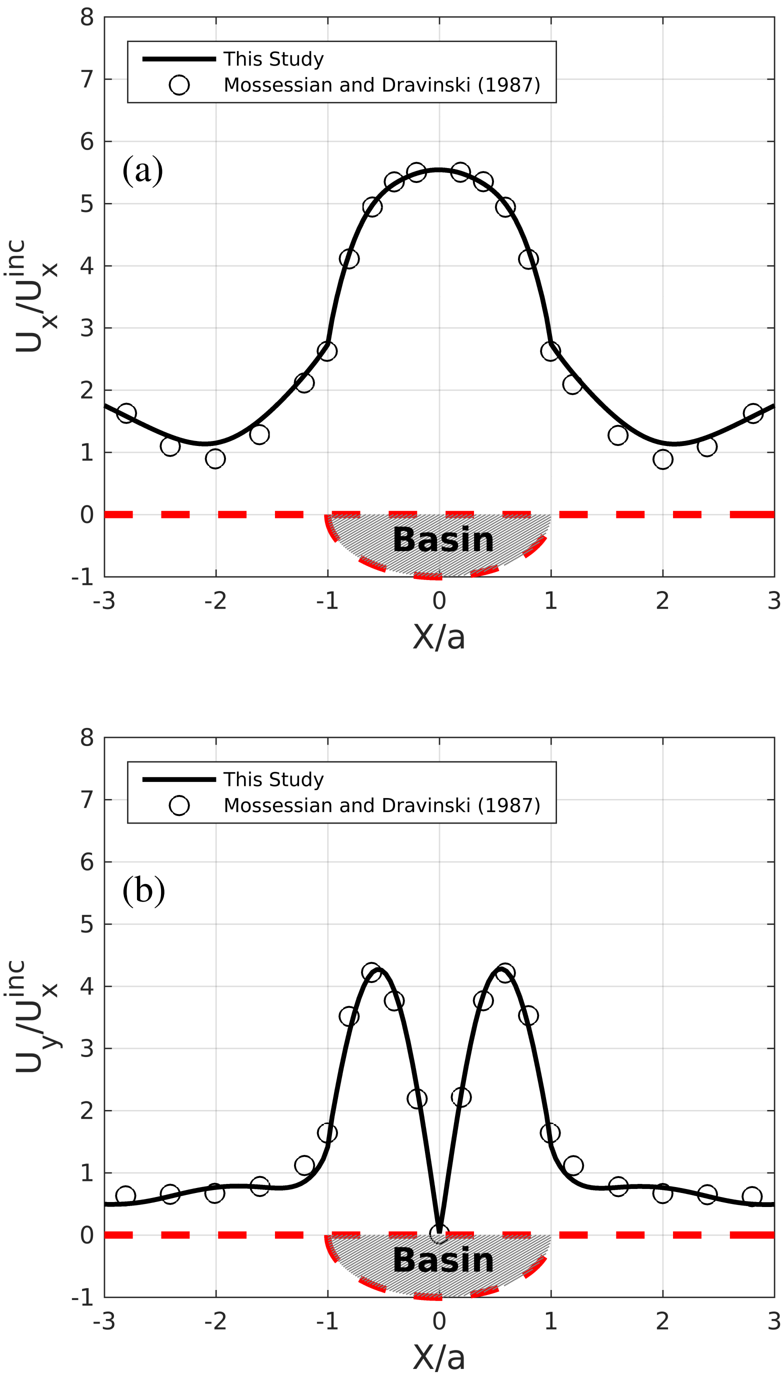

Figure 2.4: Surface AF in a) horizontal and b) vertical directions for semi-circular basin in Mossessian and Dravinski [1987].

Parameters						
π_1	π_2	π_3	π_4	π_5	π_6	π_7
0.333	0.333	2	2.5	0.25	1	2.5

Table 2.2: Material, geometry, and incident motion parameters for the trapezoidal basin in Kawase and Aki [1989].

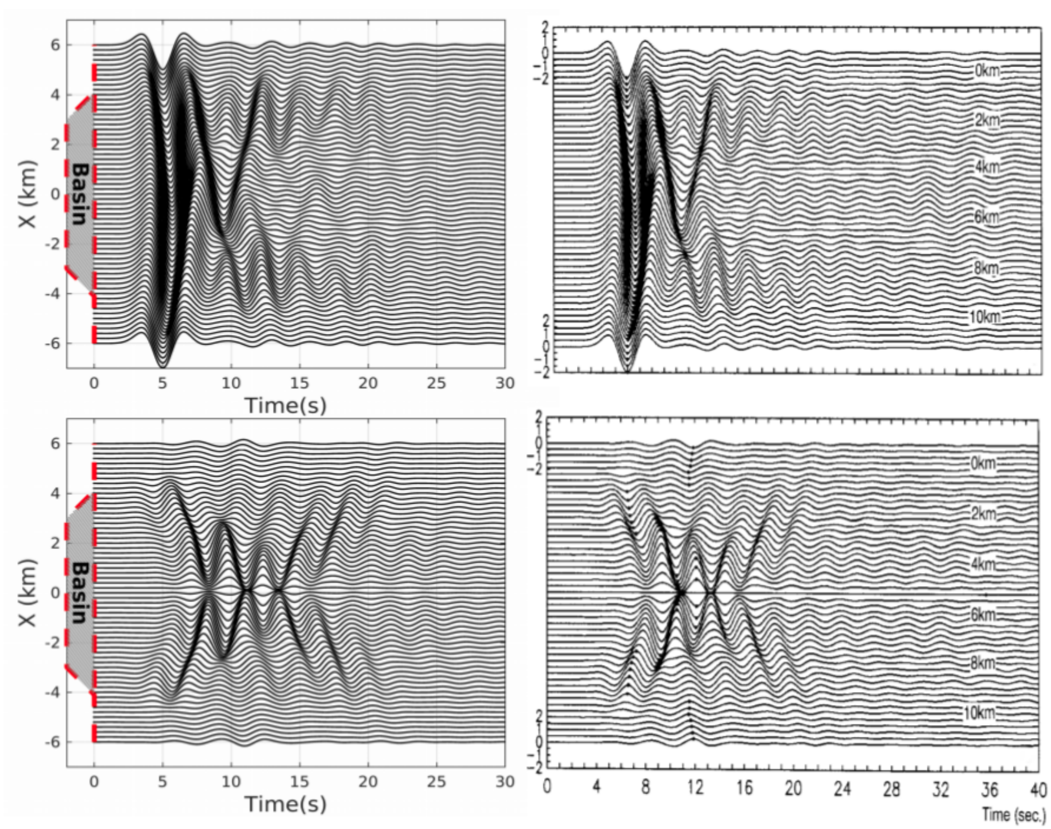

Figure 2.5: Comparison of ground surface seismogram synthetics in a, b) horizontal and c, d) vertical directions between this study (left) and Kawase and Aki [1989] (right). The figures on the right are extracted from Kawase and Aki [1989].

The two verification tests presented here, where we tested the code against two different geometries and material properties, serve as evidence of the capabilities and accuracy of the numerical model.

2.3.2 Results

In this section, we present the results of the parametric study for each basin geometry. Table 2.3 lists the dimensionless parameters and the range of values used in the following sections.

Parameters			
$\pi_3 = AR$	π_4	$\pi_5 = \eta$	$\pi_7' = \zeta$
0.5, 1, 2, 4	1.5, 2, 3.5, 5	0.125, 0.25, 0.5, 1, 2, 4	0.25, 0.5, 1, 1.5, 2, 2.6, 3.2, 3.8, 4.4, 5, 8, 12

Table 2.3: Parameter space considered in this study.

First, we show results from the SE basin, where we elaborate on the underlying physics of basin effects by first investigating the effects of the aspect ratio AR; followed by the impacts of dimensionless frequency, η. We also investigate the role of material contrast, β_2/β_1, and dimensionless width of the basin, ζ. Finally, we study the dimensionless parameters that we claimed have a lesser impact on the ground surface motion, namely π_1, π_2 and π_6. For the HC basin shape, a more realistic idealized geometry for studies of basin effects, we highlight the differences from the SE basin shape, stemming from the shape of basin edges. At the end of the HC section, we also present the effect of material (low-strain) damping on surface amplification. We finally demonstrate the effectiveness of our parameterization by comparing our long-period simplified simulations to the recorded ground motions at the Kathmandu Valley in Nepal during the M7.8 2015 Gorkha Earthquake.

2.3.2.1 Semi-Elliptical Basins

Figure 2.7 shows the maximum AF of the horizontal component of ground surface motion from the ensemble of SE basin analyses corresponding to $D = 0$, a narrow basin expected to be characterized by a complex 2D wavefield due to the short distance of the two basin edges. The effect of ζ will be discussed later in the chapter. Note the four parameters we will be using in the following sections with reference to Figure 2.6, $AR = a/b, \eta = bf_0/\beta_1$, $C = \beta_2/\beta_1$, and $\zeta = (D + 2a)f_0/\beta_1$.

Results show that for a given AR, the amplification factor generally increases with increasing material contrast β_2/β_1, similar to the observation for spectral amplification by

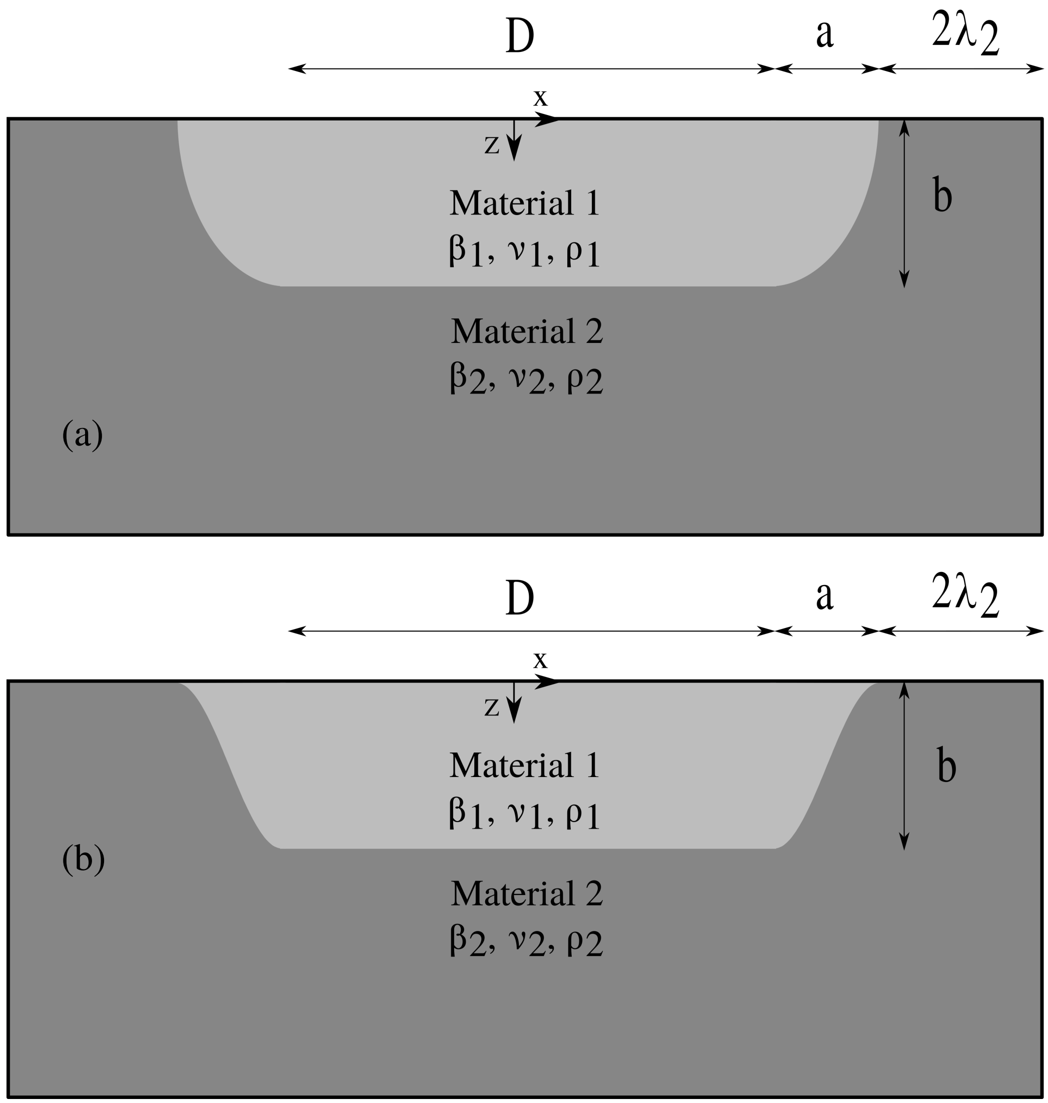

Figure 2.6: Schematic view of a) SE and b) HC basins. λ_2 is defined as β_2/f_0.

Narayan [2010]. This is not particularly surprising since high β_2/β_1 implies a higher percentage of energy entrapment in sediments and lower energy leakage. There are, however, a few results that merit further discussion: the case of $AR = 0.5$, $\eta = 4$ and $\beta_2/\beta_1 = 1.5$ (circled in the top left subfigure 2.7) is a deep basin with relatively stiff sediments subjected to high-frequency ground shaking. We observe a very high amplification (AF = 2.95) close to the maximum AF that we observed from the ensemble of simulations. As shown in Figure 2.8, this happens due to the synchronous arrival of direct waves and edge-induced surface waves at the center of the basin, where they constructively interfere. More specifically, Figure 2.8 illustrates the wavefield evolution in four stages outlined below:

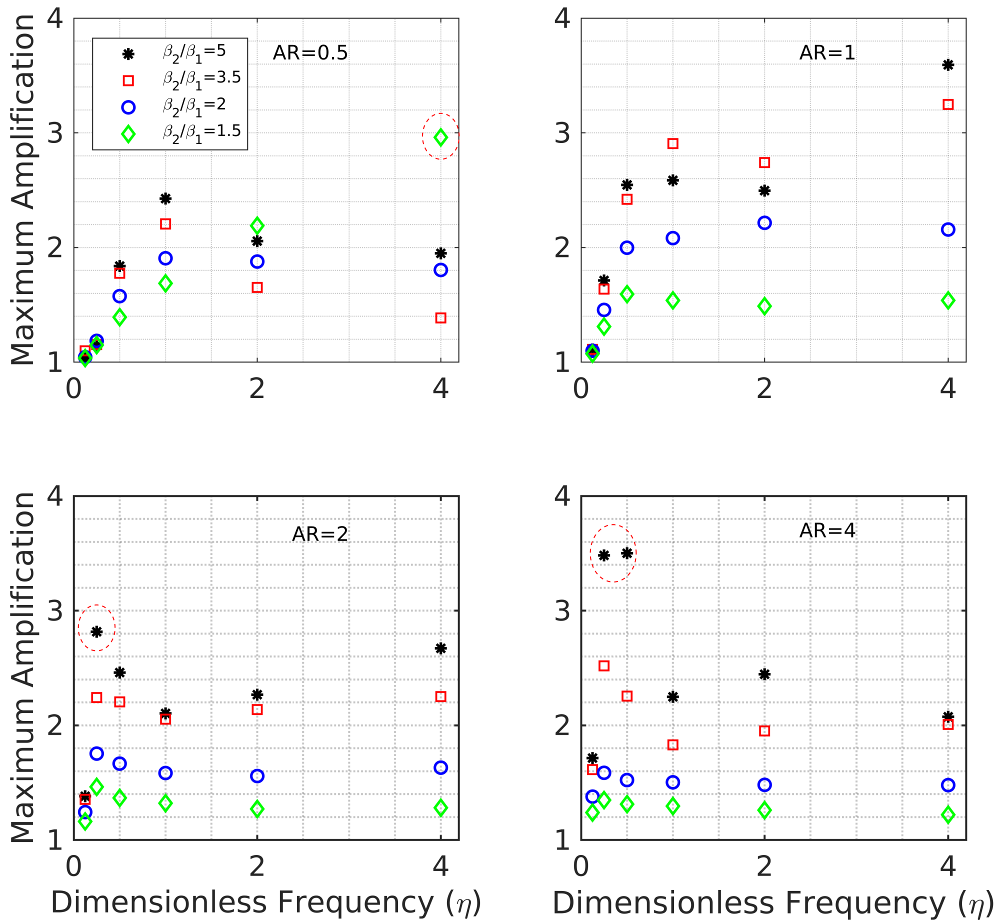

Figure 2.7: Maximum horizontal AF for all SE analyses. Red circles show unexpected results due to constructive wave interference.

a) The incident wave hits the deepest part of the basin. One can identify the onset of wavefield distortion in the basin. The sediment-rock material contrast plays an important role since it determines the amplitude of the seismic pulse that enters the basin and regulates the amount of time it takes to reach the basin surface.

b) Vertical-incident waves from the base, and laterally-propagating surface waves from basin edges travel toward the basin center.

c) Waves interact while waves propagate toward the basin center.

d) Maximum amplification occurs when they constructively interfere at the center.

On the opposite end, for a very shallow basin with very soft sediments, the case of $AR = 4$, $\beta_2/\beta_1 = 5$, and $\eta = 0.25$ to $\eta = 0.5$, a similar phenomenon of constructive interference in

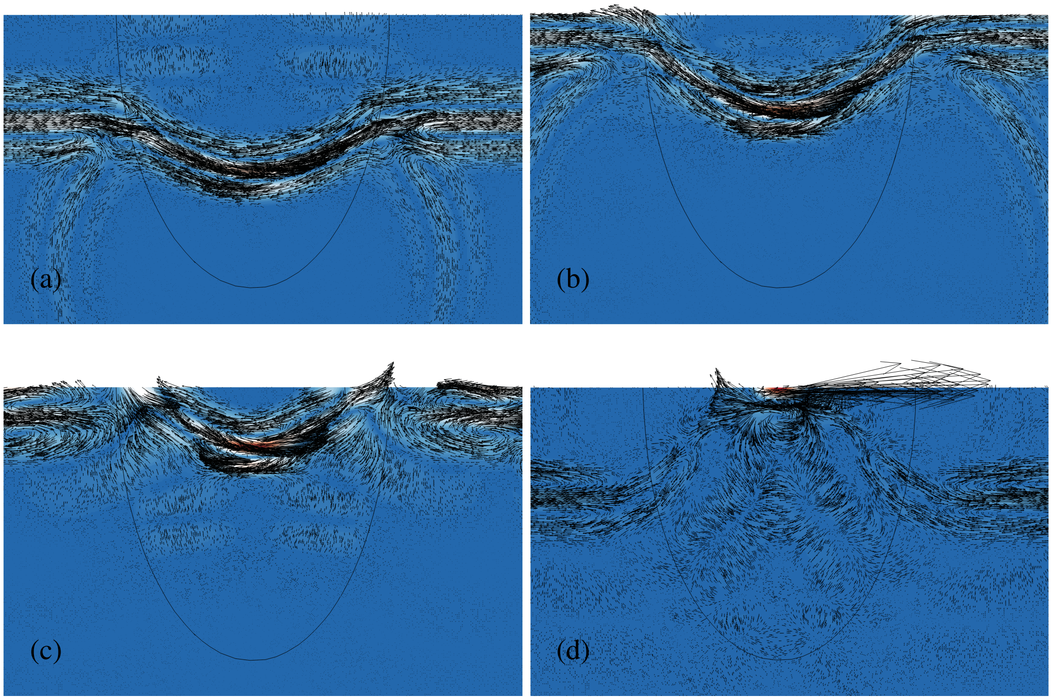

Figure 2.8: Snapshots of the wavefield for an SE basin with $AR = 0.5$ and $\beta_2/\beta_1 = 1.5$, subjected to vertically propagating shear waves of $\eta = 4$: a) incident wave enters the basin; b,c) body and surface waves travel towards the basin center; d) body and surface waves generate the maximum AF at the basin center.

the middle of the basin occurs, as shown in Figure 2.9. On the left, the spatial distribution of amplification is displayed where the maximum amplitude occurs in the middle. Looking at the seismogram synthetics, the maximum amplitude takes place at dimensionless time $t^* = 5$. In addition to high AF, due to material velocity contrast, we recognize the reverberations of trapped energy in the sediments, which in addition to significant AF, lead to prolonged motion duration.

Effect of Aspect Ratio (AR) AR defines the average slope of basin edges, which have been shown to dominate the response of most basins during seismic events (Kawase [1996]). In this subsection, we present results of surface amplification for various AR values. The spatial variations of horizontal and vertical amplifications are portrayed in Figures 2.10 (low frequency incident motion) and 2.12 (high frequency incident motion) for a set of aspect ratios, velocity contrasts, and dimensionless frequencies. Figure 2.11 illustrates the SS for the top panel of Figure 2.10, and helps to explain the observed surface amplification.

From these figures, one can observe a considerable variation associated with varying the

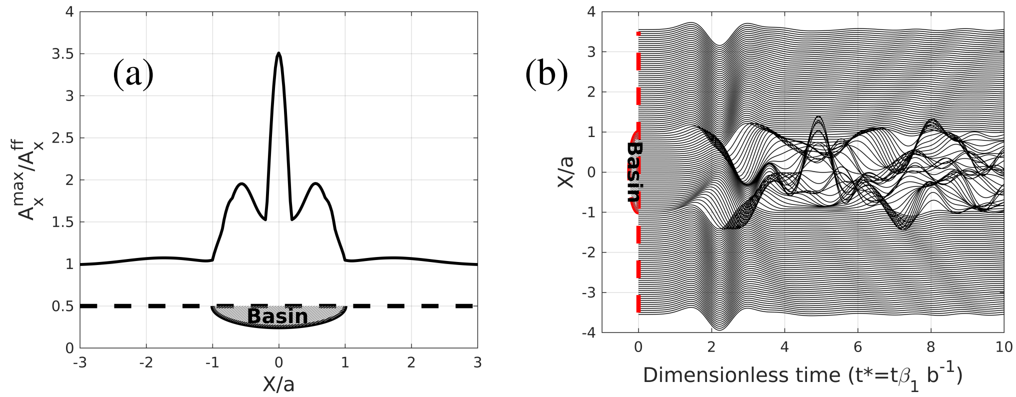

Figure 2.9: Result of model with $AR = 4$, $\eta = 0.5$ and $\beta_2/\beta_1 = 5$, a) AF and b) SS in horizontal direction.

AF in horizontal and vertical directions. Focusing on Figure 2.10, it is clear that for this particular setting, $AR = 1$ has the largest amplification in the horizontal direction for both material contrasts due to constructive interference of direct arrival of the incident wave and laterally propagating edge-induced surface waves, as can be seen in Figure 2.10-a and c. The wave interference and consequent peak amplification occur closer to the basin edges for shallower and deeper basins. The AF of the vertical component, which arises purely from mode conversion (recall that our input motion was a vertically propagating horizontally polarized SV wave), is generated primarily from edge-induced (Figure 2.11-d,f,h) surface waves except for $AR = 0.5$ (Figure 2.11-b). For the deepest basin, the basin edges are not playing as important a role as their shallower counterparts. Moreover, by comparing Figures 2.10-a and b, one can see that in locations that horizontal de-amplification happens, we observe an amplification in vertical direction. However, the energy also leaks to the bedrock area and will finally be scattered to the half-space.

Figure 2.12 shows how higher frequency input motion would affect the resultant wavefield while other parameters are the same as Figure 2.10. Increasing the frequency, in general, would result in a more localized interaction of basin and incident motion. This is projected in Figure 2.12 where higher amplification at basin corners happens over a shorter distance (see Figure 2.12-a and c). In addition, as a result of more localized interaction, the spatial variation of surface amplification is exacerbated (see Figure 2.10-b and d), which could cause severe damage to long components of the infrastructure system due to torsional particle motion. These results are in general agreement with Zhu and Thambiratnam [2016].

Based on the last three figures, the three parameters, namely the coupled behavior of basin geometry, material properties, and frequency content of the incident motion, govern the

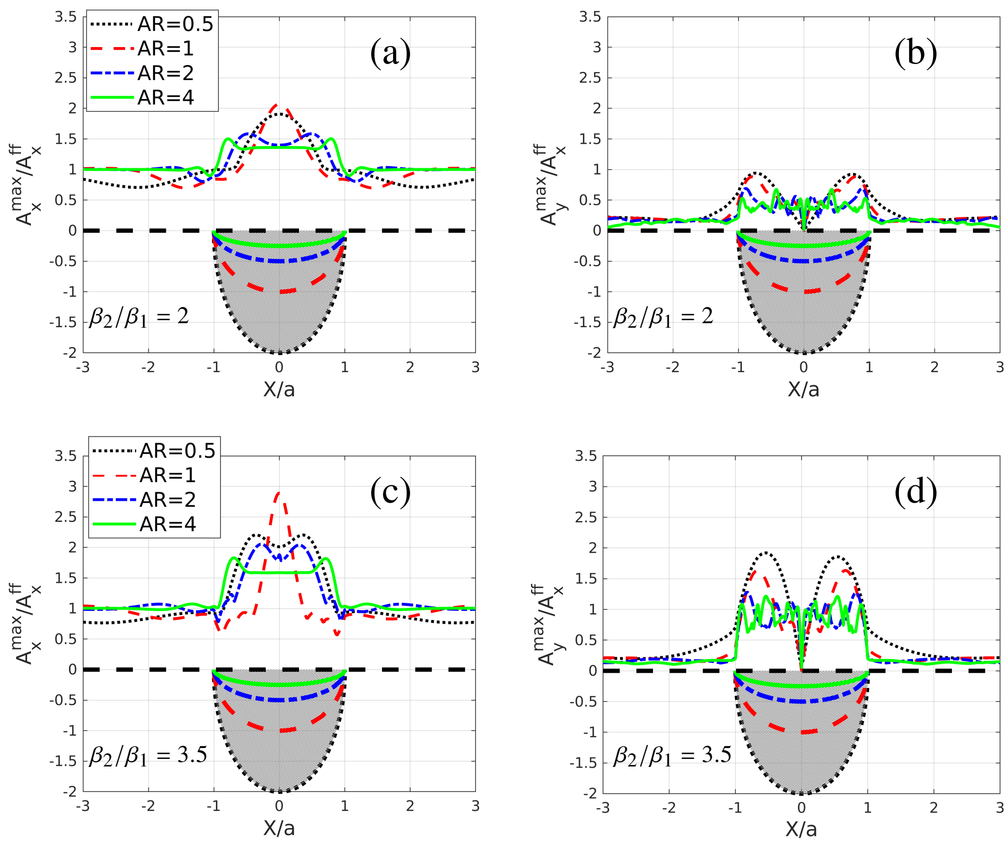

Figure 2.10: AF in a,c) horizontal and b,d) vertical directions for SE basin for a range of ARs, $\eta = 1$, $\beta_2/\beta_1 = 2$ (top panel) and $\beta_2/\beta_1 = 3.5$ (bottom panel).

surface ground motion in a basin. For the remainder of the chapter, we shall use $AR = 1$ as a point of comparison and investigate other parameters by keeping the aspect ratio constant.

Effects of Dimensionless Frequency (η) and Material Contrast (β_2/β_1) Figures 2.13 and 2.14 show the effects of dimensionless frequency (η) and material contrast (β_2/β_1) on the AF of surface ground motion for a basin with $AR = 1$. Recall that parameter η measures the basin response sensitivity to an incoming wave by quantifying the relative size of the basin to the incoming dominant wavelength. The physical meaning of the parameter is depicted in Figure 2.13, where, for $\eta \ll 0.5$ and $\eta \gg 4$, the basin is too small or too large compared to the incident wavelength, respectively. In the first case, the wave barely "sees" the basin (basin-bedrock medium behaves as a halfspace), and in the second case, the basin responds similarly to a 1D two-layer column. Therefore, $\eta = 0.125$ (wavelength 8 times larger than basin depth) results in a negligible vertical component since the basin is too small for the seismic wave to experience substantial mode conversion. This figure

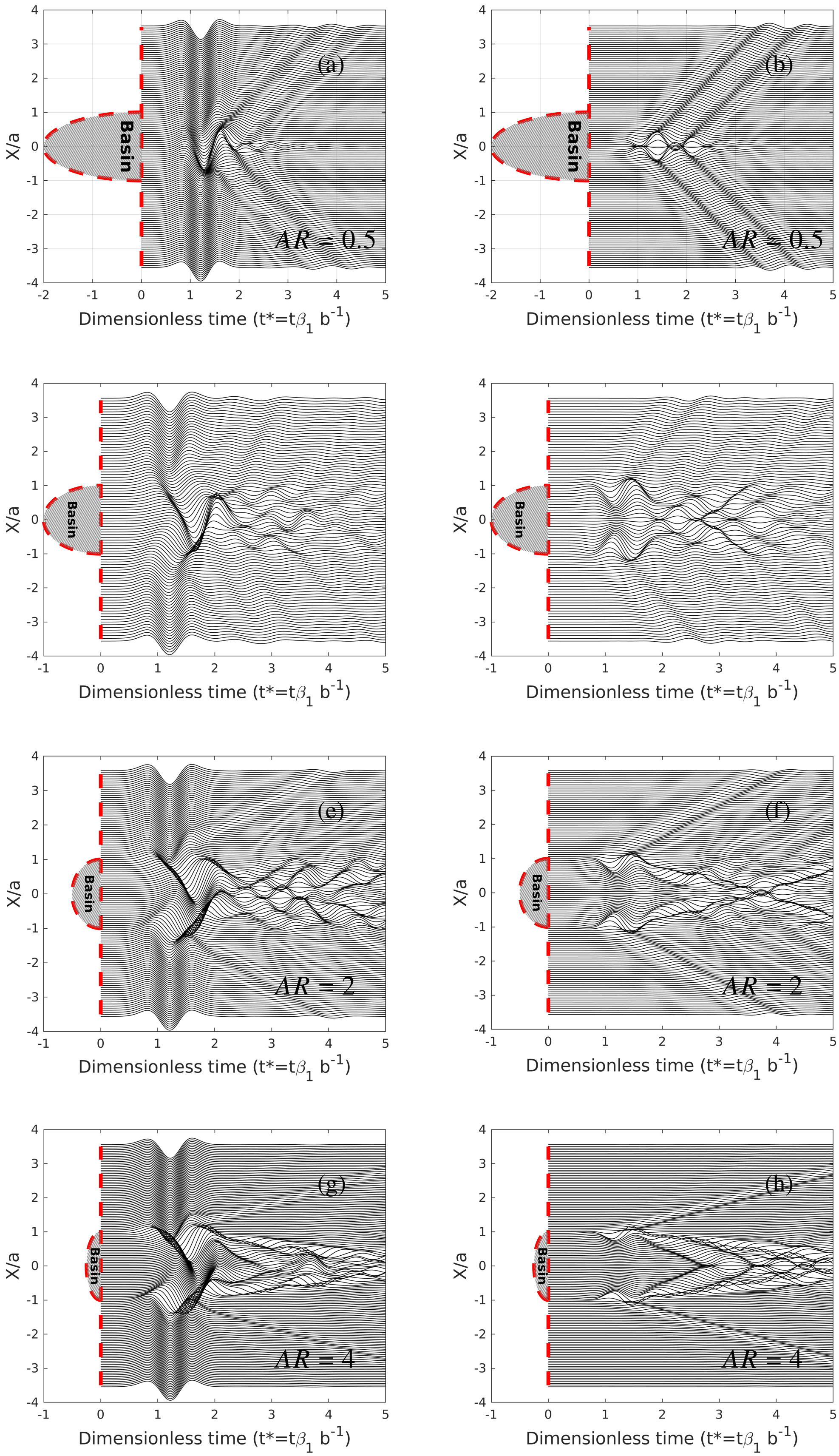

Figure 2.11: SS for $AR = 0.5$ (top panel), $AR = 1$ (second from top panel), $AR = 2$ (second from bottom panel) and $AR = 4$ (bottom panel) in a, c, e, g) horizontal and b, d, f, h) vertical directions. $\eta = 1$ and $\beta_2/\beta_1 = 2$ are assumed.

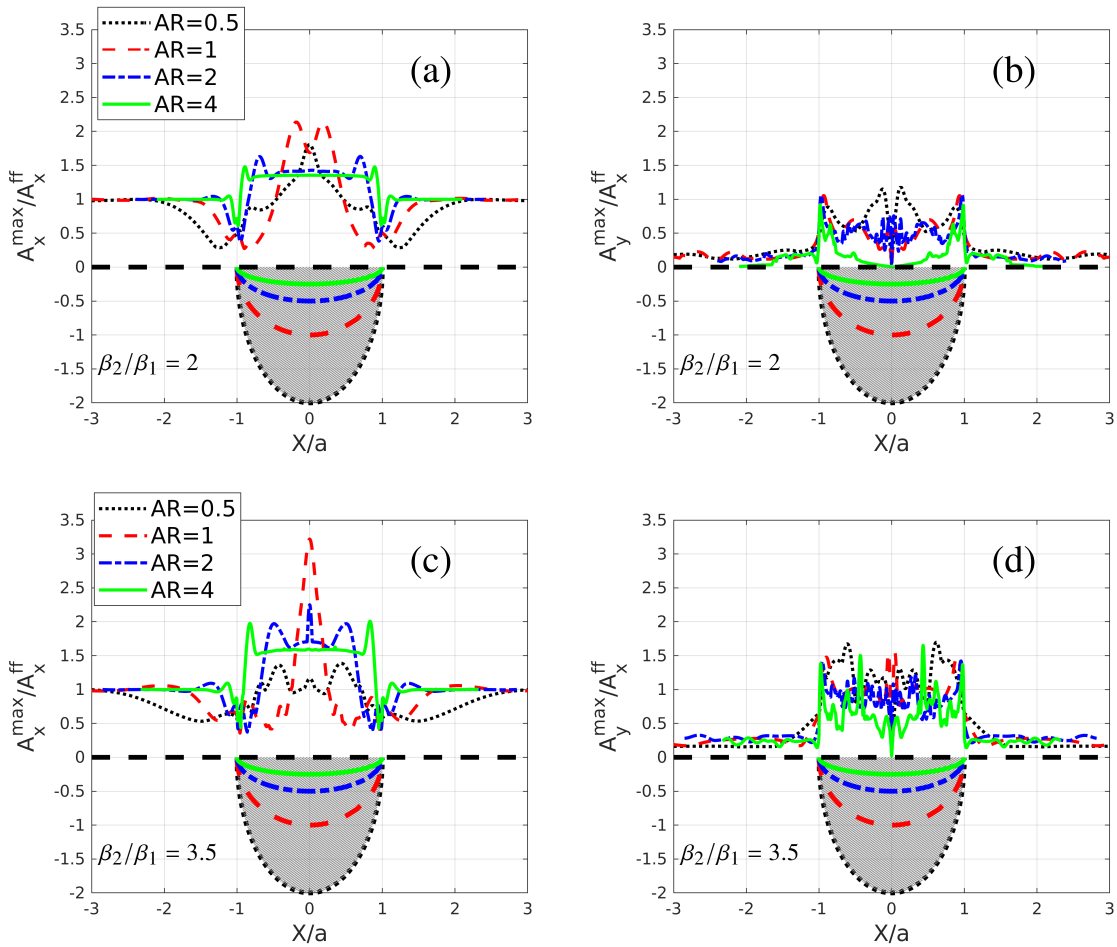

Figure 2.12: AF in a,c) horizontal and b,d) vertical directions for SE basin for a range of ARs, $\eta = 4$, $\beta_2/\beta_1 = 2$ (top panel) and $\beta_2/\beta_1 = 3.5$ (bottom panel).

also illustrates those mentioned above strong spatial variability of surface ground motion for higher frequencies. Moreover, due to the complexity of the wavefield in the basin, no specific η yields a maximum AF across the basin, which can be observed in both the horizontal and vertical components and is more pronounced near basin edges.

Figure 2.14 further details the case of $AR = 1$ by showing the effect of material contrast for different η, and thus illustrating the coupled effect of parameters of interest. The AF of the vertical ground motion component reaches a surprisingly high value. While the incoming wave is a plane SV-wave, the AF vertical component near the edges is comparable to the horizontal one. The spatial variability suggests that structures near the edges would experience not only strong transverse and vertical shaking but also rotational motion. In addition, higher frequency incident motions interact on a local scale with the geometry and material properties of the basin, which affect the ground motion characteristics over

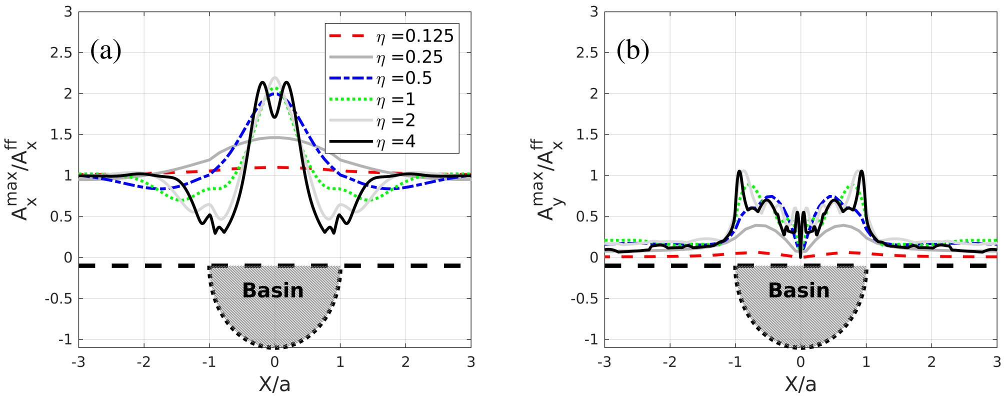

Figure 2.13: AF in a) horizontal and b) vertical directions for SE-shaped basin with AR=1 and $\beta_2/\beta_1 = 2$.

shorter distances. The opposite is true for longer wavelengths. For the case of $\eta = 0.5$, both horizontal and vertical AFs reveal that the incident motion interacts with the basin as a whole, a fact evidenced in the smooth spatial variation of AF across the basin. By looking through this figure, the localization effect of frequency increment is noticeable. For example, by comparing the AF in Figures 2.14-b and 2.14-d, one can see that Figure 2.14-d indicates a more complex amplification distribution due to higher frequency content.

Effect of Dimensionless Width (ζ) So far, we have investigated three parameters with $D = 0$ to observe the wavefield in a basin. We focus on edge-induced Rayleigh waves for this subsection by examining the effects of $D > 0$. Figure 2.15 shows the effect of the dimensionless width (ζ) on the spatial distribution of surface amplification on a SE basin. Note that the minimum value of ζ corresponds to its value for $D = 0$, namely $\frac{2a}{\lambda_1} = 2\eta AR$. By increasing ζ, the amplification decreases, and separation between two corners appears. This results in a nearly 1D response in the middle of the basin (denoted by a blue star in Figure 2.15) while the 2D effects dominate as one moves closer to the basin edges. This does not mean that the middle area of the basin will experience purely horizontal motion since the Rayleigh wave's traverse motion will still generate significant vertical movement. This phenomenon will be explained in more detail in a later section of this chapter.

Effect of Other Dimensionless Parameters In this subsection, we examine the effects of three dimensionless parameters we have not investigated yet (see Eq. 2.8), namely the Poisson's ratio of the sediments (ν_1) and the bedrock (ν_2), and the ratio of the mass density of the sediments to the bedrock ($\frac{\rho_1}{\rho_2}$). The range of values we consider is shown in Table 2.4. Figure 2.16 shows the effects of Poisson's ratio on the surface amplification for $\beta_2/\beta_1 = 2$

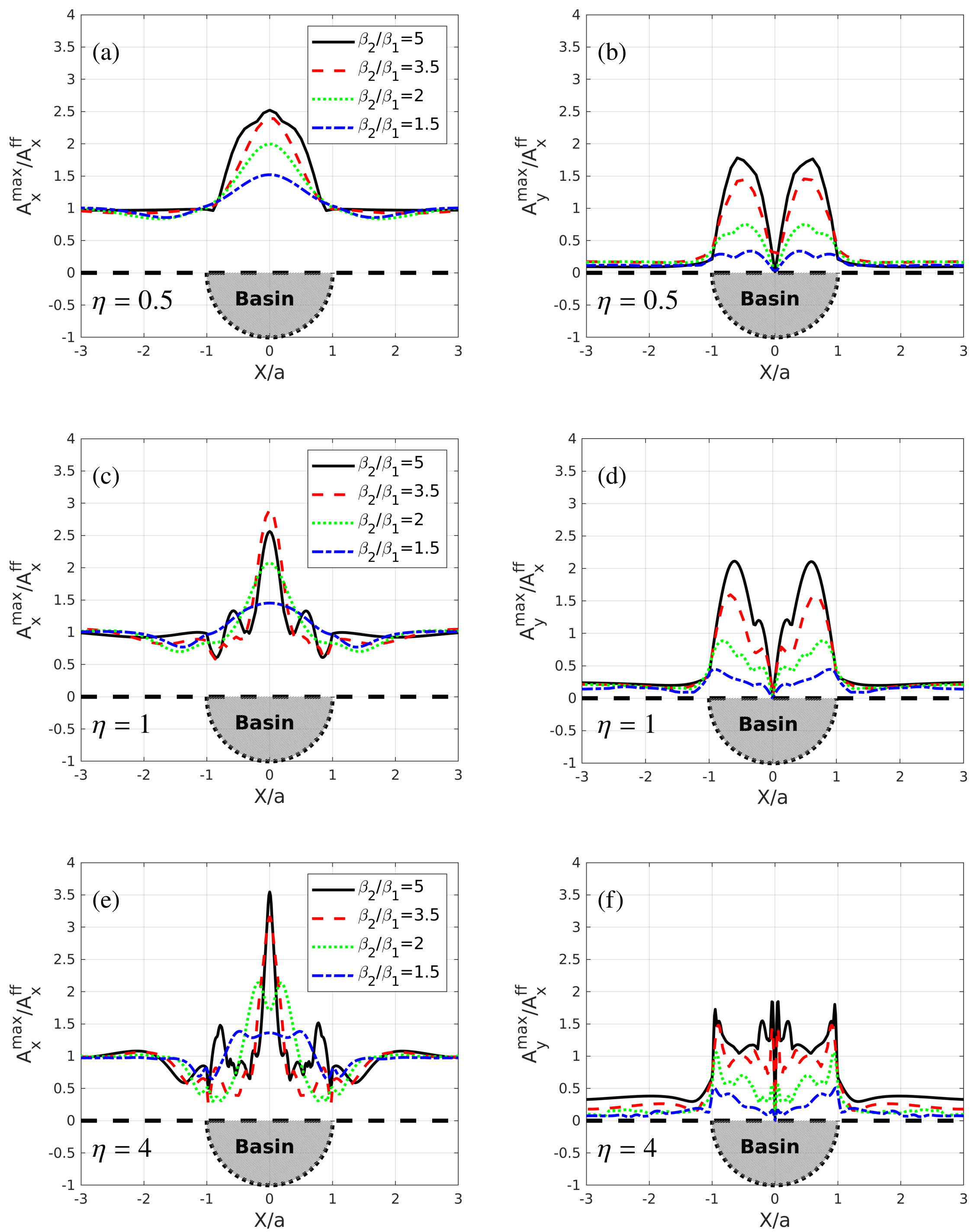

Figure 2.14: AF in horizontal (left panel) and vertical (right panel) directions for SE basin with AR=1 and a,b) $\eta = 0.5$, c,d) $\eta = 1$, e,f) $\eta = 4$. Three different ηs are shown to also show the coupled effect of material contrast and dimensionless frequency.

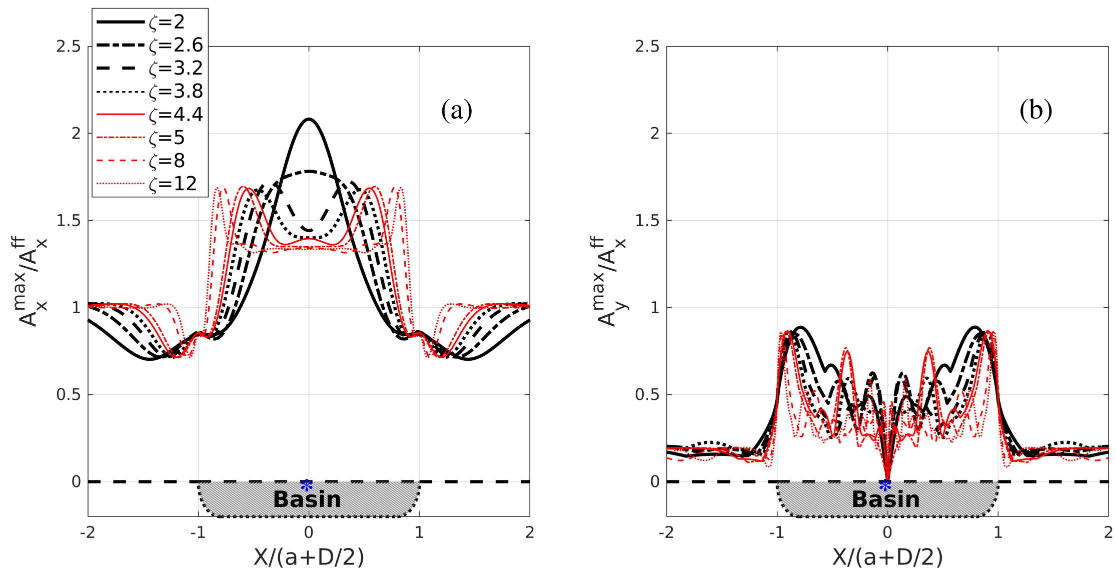

Figure 2.15: Effect of dimensionless width ($\zeta = (D+2a)/\lambda_1$) for SE basin for a) horizontal and b) vertical components. $AR = 1$, $\eta = 1$ **and** $\beta_2/\beta_1 = 2$ **are assumed.**

Parameters		
$\pi_1(\nu_1)$	$\pi_2(\nu_2)$	$\pi_6 = \rho_1/\rho_2$
0.25, 0.35, 0.45	0.2	$\frac{2}{3}$, 0.8

Table 2.4: Considered parameters for studying effects of π_1, π_2, and π_6.

and $\beta_2/\beta_1 = 3.5$, $\eta = 1$ and $AR = 1$. As can be readily seen, the effects of Poisson‘s ratio are negligible compared to the four main dimensionless parameters we discussed earlier. We should, however, note here that we expect the effects of Poisson’s ratio to be more pronounced for nearly incompressible material behavior ($\nu \approx 0.5$ or undrained loading conditions).

Similarly, Figure 2.17 shows the effects of density contrast (ρ_2/ρ_1) on the spatial variability of peak amplification, for the case of an SE basin with $\eta = 1$ and $AR = 1$. Results are shown for two velocity contrasts $\beta_2/\beta_1 = 2$ and 3.5. As can be seen, the effects of density contrast are on the order of 5% in the vicinity of the peak horizontal and vertical amplification, which are still considered of secondary importance compared to the four parameters investigated earlier.

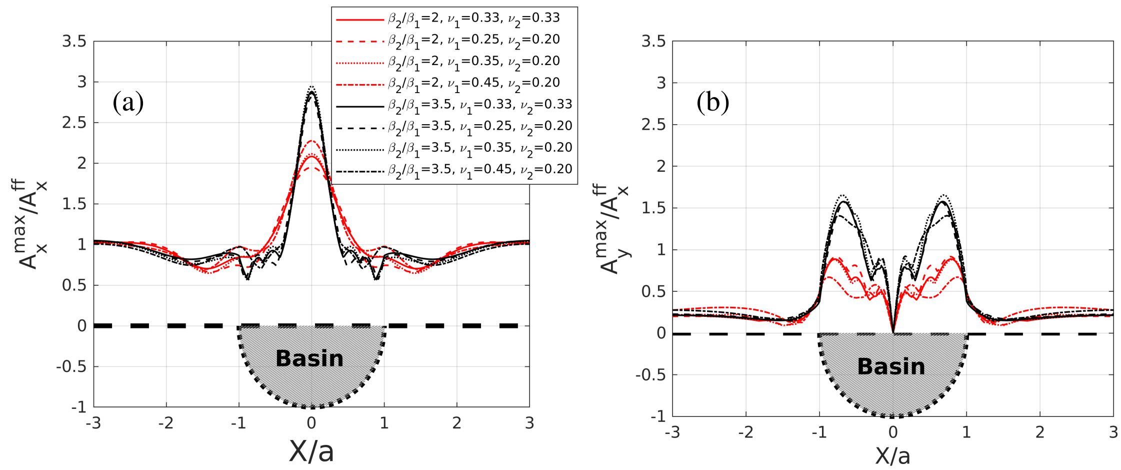

Figure 2.16: Effect of ν on surface ground motion for two different β_2/β_1 values, for SE basin with $\eta = 1$ and $AR = 1$ in a) horizontal and b) vertical directions.

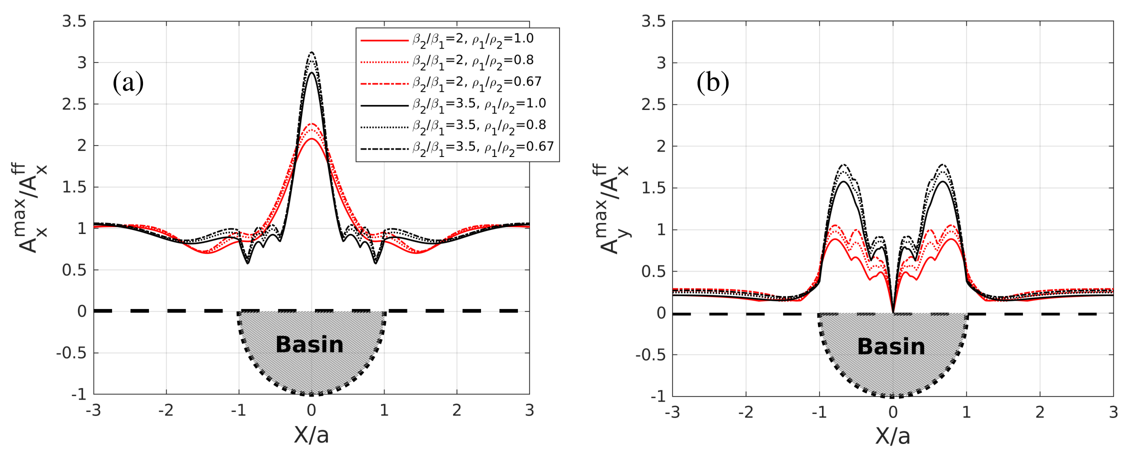

Figure 2.17: Effect of ρ_1/ρ_2 on surface ground motion for two different β_2/β_1 values, for the case of an SE basin with $\eta = 1$ and $AR = 1$ in a) horizontal and b) vertical directions.

2.3.2.2 Half-Cosine Basins

Although SE models have been widely used as idealized basin geometries (Trifunac [1971], Dravinski [1982]), their sharp corners do not resemble realistic basin edges. In more realistic scenarios, one would expect landscape evolution processes, such as weathering and alluvial or fluvial deposits, to lead to a more gradual transition from rock to sediments near the basin edges. Given the critical role of edges in the focusing and diffraction phenomena that govern basin effects (see Figure 2.18), we here study a more realistic idealized basin shape adopted from the geomorphology literature and referred to as Half-Cosine (HC) (see Figure 2.6).

Figure 2.18 compares the particle motion of two basin geometries (SE and HC) near the edge with otherwise identical aspect ratios, impedance contrasts, dimensionless width, and frequency. The bottom row schematically depicts the geometry of the basin edge and the location where the comparison is taking place. As can be seen, the wavefield is affected by the basin edge geometry (and convexity). The particle motion change would be even more pronounced for higher frequency components. Note that the edge geometry caused a horizontal shift in the wavefield, and it seems that each point on the SE basin corresponds to a further point in HC. For example, points 4 and 4^* have similar particle motions.

For the rest of this section, we focus on the parameters directly affected by edge geometry, namely AR and ζ. Although η and β_2/β_1 have been shown to alter the basin's wavefield significantly, their effects do not differ significantly for a given AR and ζ; results are thus demonstrated for the case of $\eta = 1$ and $\beta_2/\beta_1 = 2$, similarly to SE geometry.

Effect of Aspect Ratio (AR) The effects of AR for HC basins are depicted in Figure 2.19. The impact of edge convexity manifests in the spatial distribution of AF. As can be seen, by changing the basin geometry, the separation of edges does not happen as fast as it happened in the case of the SE basin (Figure 2.10) because of gradual variation of the basin-bedrock interface depth over distance. This shows how a more realistic basin geometry could affect the amplification variation in a basin, especially for shallower ($AR > 1$) configurations that are more prevalent in urban environments.

Effect of Dimensionless Width (ζ) Figure 2.20 shows the effect of ζ on the surface ground motion in the horizontal and vertical directions. We consider a range of ζ that captures the response of narrow and wide basins. Results illustrate the fading effect of basin edges on the amplification factor close to the basin center. This does not mean that the basin middle would behave as a purely 1D column due to Rayleigh waves traverse propagation within the

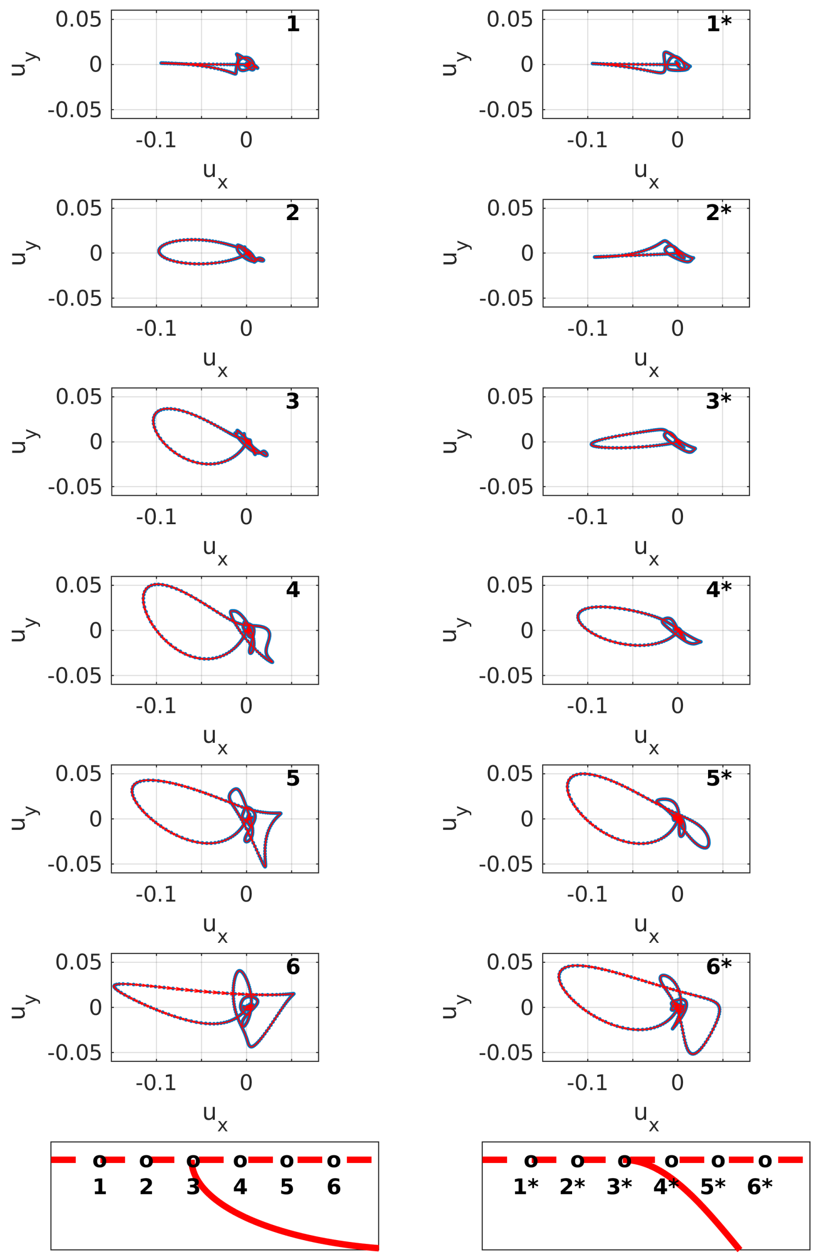

Figure 2.18: Particle motion comparison for SE and HC basins in the vicinity of basin edge. $AR = 1$, $\eta = 1$ and $\beta_2/\beta_1 = 2$ are assumed.

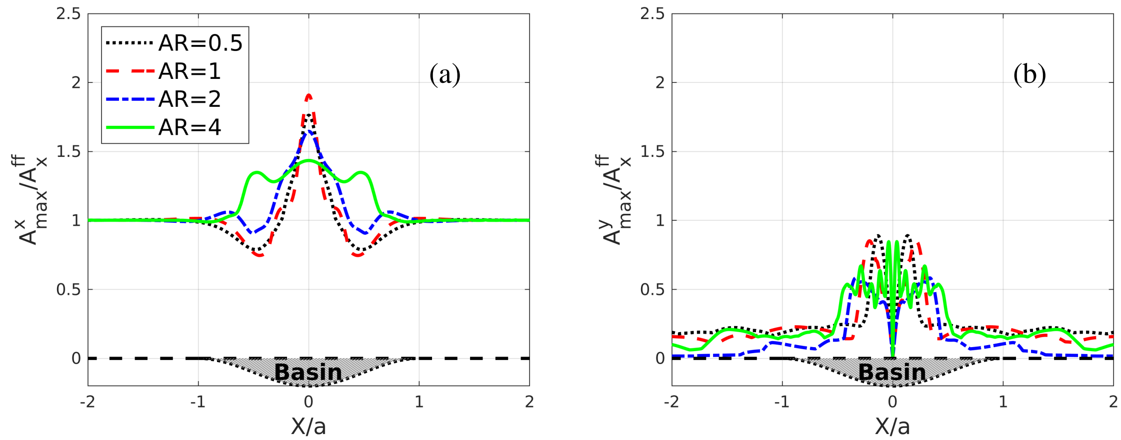

Figure 2.19: AF for different ARs of HC basins of $D = 0$, $\eta = 1$ and $\beta_2/\beta_1 = 2$ in a) horizontal and b) vertical directions.

basin which mainly contributes to the vertical component of surface ground motion. As can be seen, for separation $\zeta \geq 5$, the corner half-cosines have minimal influence in shaping the horizontal amplification, evidenced by a uniform spatial distribution of AF over the central part of the basin.

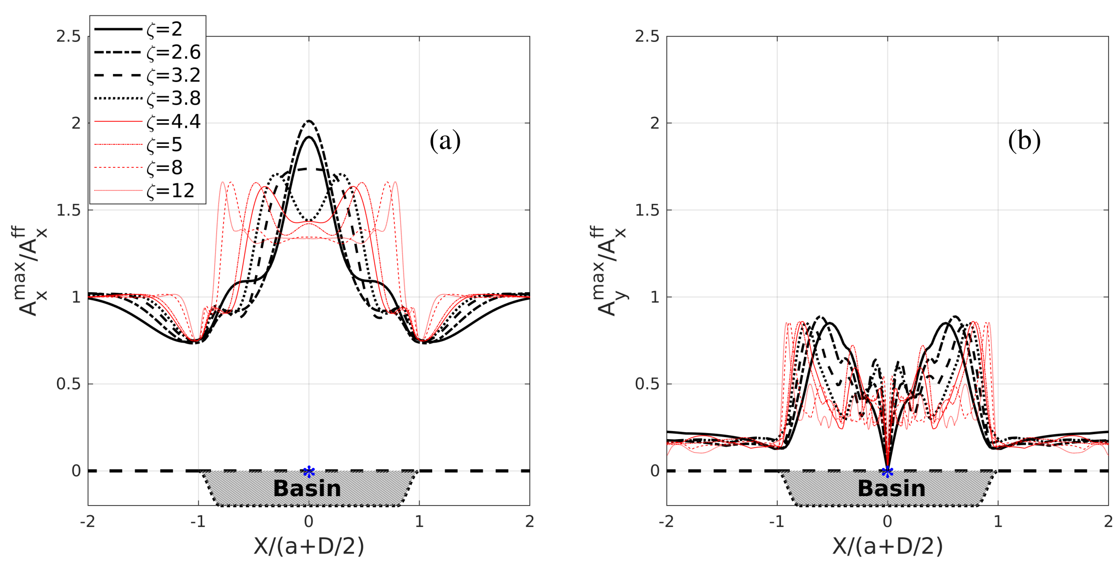

Figure 2.20: Effect of dimensionless width (ζ) on the surface amplification in a) horizontal and b) vertical directions. $AR = 1$, $\beta_2/\beta_1 = 2$ **and** $\eta = 1$ **are assumed.**

.

Results of the midpoint response for an HC basin are next compared, for representative ζ, to the analytical solution of a 1D two-layered linear elastic soil column (Tsai and Housner

[1970]) subjected to a vertically propagating SV Ricker wave. Figure 2.21 compares the acceleration time series, Fourier, and response spectra at the basin midpoint calculated from 2D wave propagation simulations for $\zeta = 3, 5, 9$, and 12 to the corresponding response of a horizontally stratified 1D layered model. As expected, by increasing ζ, the basin center (denoted by a blue star in Figure 2.20) increasingly responds like a 1D column as the two basin edges separately. However, even for the case of $\zeta = 12$, edge-induced surface waves traveling horizontally are evident as late arrivals in the midpoint signal, an effect that 1D site response approximations are not able to capture.

Effect of Damping In reality, during large earthquakes, the soft sedimentary deposit would undergo considerable deformation that causes wavefield attenuation. In this article, we have so far studied the coupling effects of geometry, material contrast, and frequency content without the attenuating contribution of material damping (low-strain assumption). At this strain range, we use Rayleigh damping and change its parameters to match the frequency range of interest. Figure 2.22 shows a comparison between two configurations with $AR = 1$ and $AR = 4$; $\eta = 1, \beta_2/\beta_1 = 2$ and a range of realistic damping values. Two damping values $\xi = 2.5\%$ and 5% are considered, and the resultant amplification curve is compared with the no-damping condition. In order to calibrate Rayleigh damping parameters, $f_{min} = 0.15$ (Hz) and $f_{max} = 3.5$ (Hz) are used while the dominant frequency of input motion is $f_0 = 1$ (Hz) and the fundamental frequency of the soil column corresponding to the deepest part of the basin is $\frac{\beta_1}{4b} = 0.25$ (Hz). For the range of geometries and damping values studied here, results are affected by low-strain attenuation in the horizontal direction only at the midpoint of the basin (and no more than $AF \leq 20\%$, and are practically unaffected in the vertical direction). We should, however, highlight that results are shown only for $\eta = 1$, and that higher frequency ground motions are expected to be more strongly affected by low-strain damping effects.

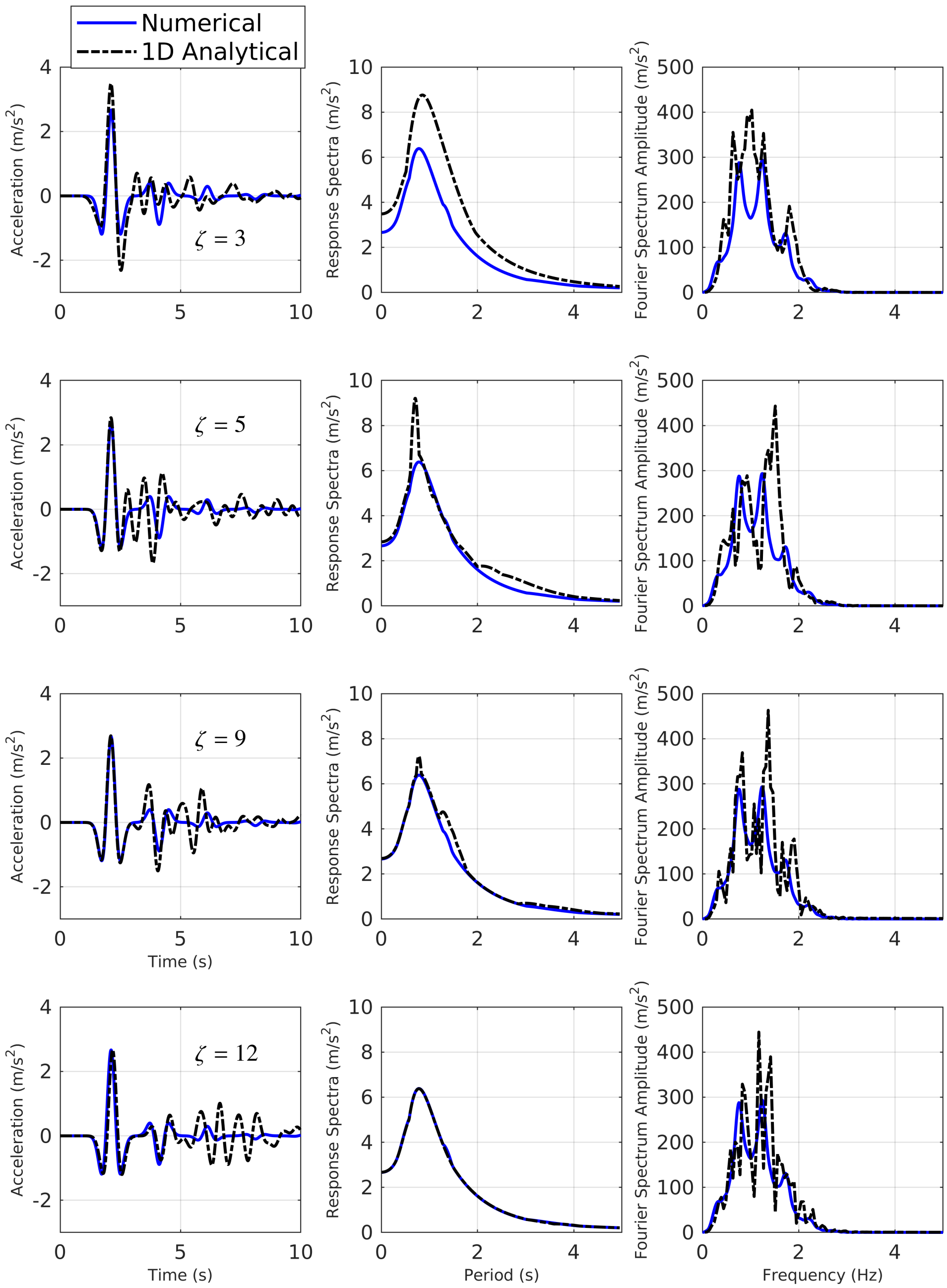

Figure 2.21: Comparison of the 1D analytical solution with the numerical results at the basin center. The ζ value is shown on the figure. $AR = 1$, $\eta = 1$ and $\beta_2/\beta_1 = 2$ are assumed.

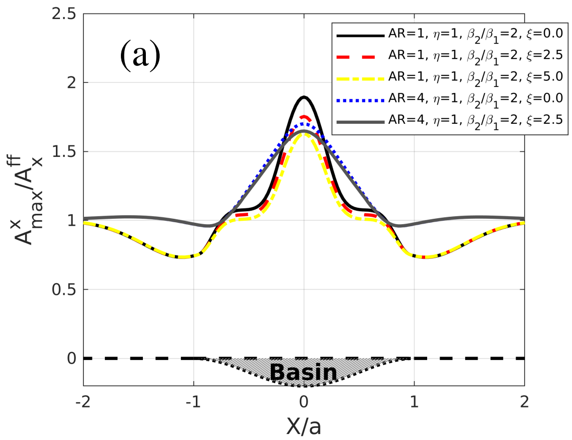

Figure 2.22: Effect of damping of surface AF in a) horizontal and b) vertical directions. We assumed two different damping parameters ($\xi = 2.5$ and 5.0), $\eta = 1$, and $AR = 1$ and 4.

Finally, wavefield snapshots for an HC basin with $AR = 1$, $\beta_2/\beta_1 = 2$ and $\zeta = 3$ are shown in Figure 2.23. The middle rectangle-like part of the basin behaves similarly to a 1D column before the edge-generated surface waves arrive. At the same time, the corner half-cosines where surface waves originated from amplifying the wavefield via focusing. Although the surface wave characteristics differ from the case of the SE-basin due to differences in edge geometry, the same general four-stage wavefield evolution can be observed here as well: (a) body wave arrival, followed by (b-c) surface wave generation at the edges, followed by (d) interaction of body and surface waves in the middle, followed by (e-f) horizontal and vertical wave reverberations in the basin and energy leakage towards the halfspace. The characteristic rotational wave pattern at the base of the basin shown in Figure 2.23-f is referred to as the "breathing zone" (Momoi [1980]), a region where energy transfer occurs between the scattered P- and S-wavefields.

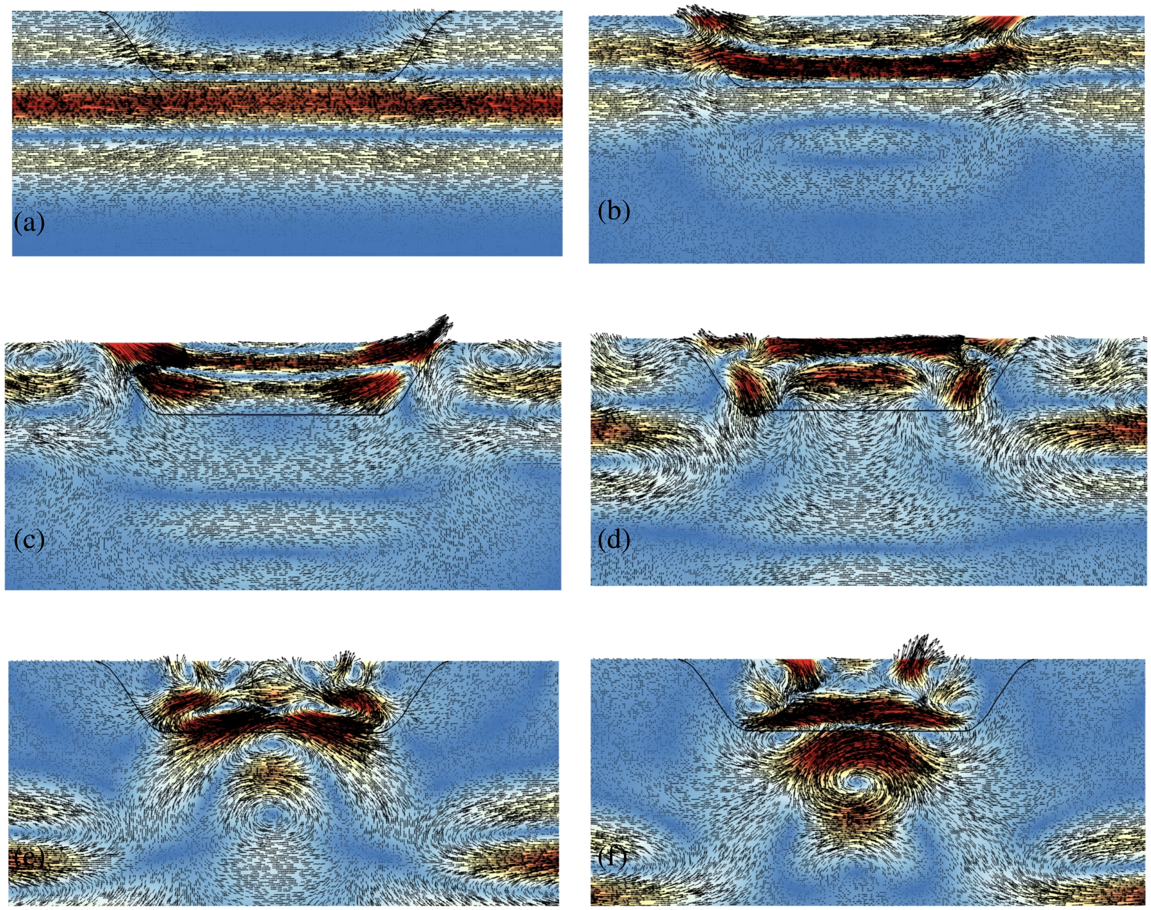

Figure 2.23: Snapshots of total wavefield for HC basin with AR=1, $\zeta = 3$, $\eta = 1$, and $\beta_2/\beta_1 = 2$. The trapezoidal black line shows the basin boundary.

HC basins with large ζ are an appropriate representation of wide shallow basin geometries, similar to the trapezoidal geometry used by Kawase and Aki [1989] to study basin effects in Mexico City. In the following section, we use an HC idealized geometry to analyze basin effects in Kathmandu, Nepal, that were observed during 2015 M_w 7.8 Gorkha Earthquake.

2.4 Basin Effects in Kathmandu, Nepal: A Simplified Model Approximation

During the 2015 M_w 7.8 Gorkha Earthquake (Asimaki et al. [2017]), macroseismic observations and recorded evidence strongly showed that basin effects had played an essential role in the characteristics of strong-motion recordings and the distribution of damage (or lack thereof). To test how simplified models can capture complexities of basin effects, we here approximate the Kathmandu basin with an HC idealized model. The model was selected

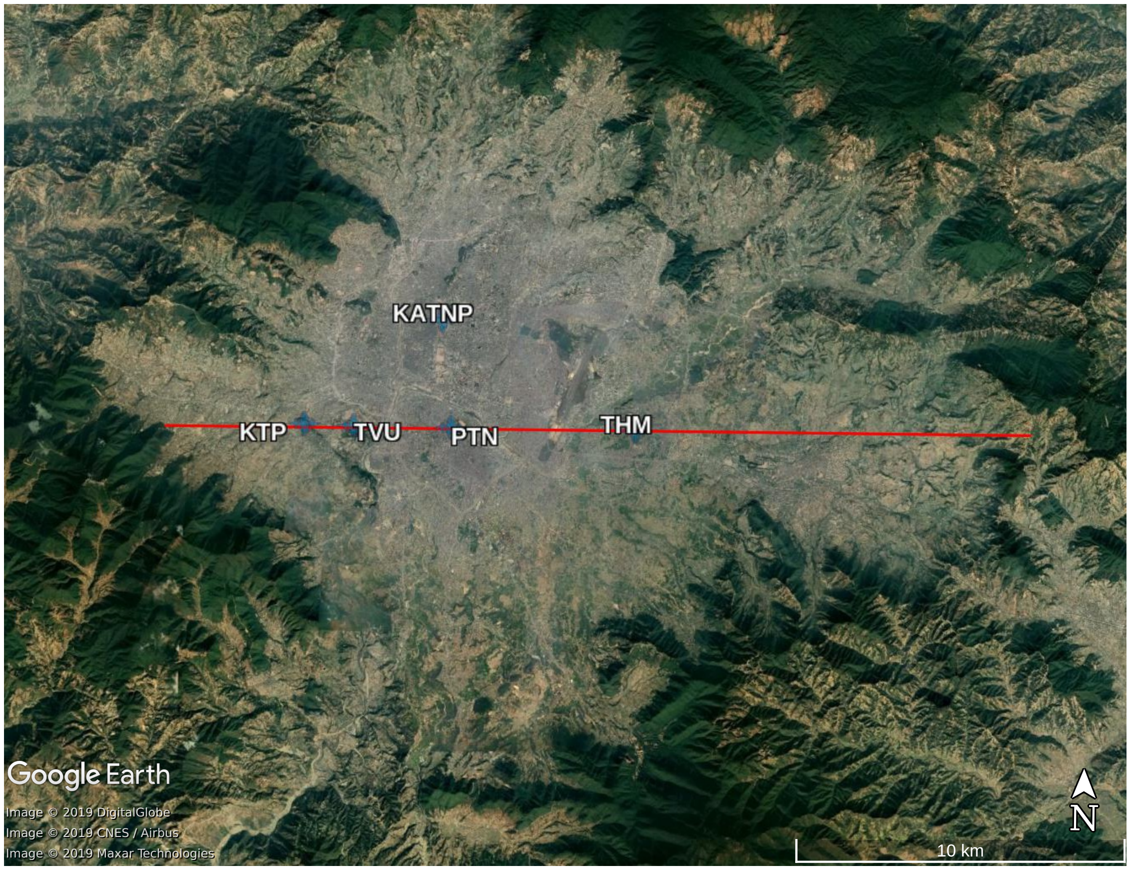

Figure 2.24: A plan view of Kathmandu basin. The location of strong ground motion stations is shown by their name. The red line shows the cross-section used by Ayoubi et al. [2018] and is used in this study.

to match the geometry of the top 0.5 km of basin sediments and is shown in Figure 2.25 (see Ayoubi et al. [2018] for more detail). The cross-section of the basin corresponds to the red line shown in Figure 2.24. Hokkaido University and Tribhuvan University installed the strong ground motion stations depicted in the same figure, and they reported the recorded accelerations during the mainshock (Takai et al. [2016]). These records will be used to evaluate the accuracy of the idealized model presented in this study.

To estimate the basin response of the idealized model, we use a train of two plane SV Ricker wavelets as shown in Figure 2.26-a, to excite a range of resonant modes of the basin. The "Data" in Figure 2.26-b shows the incident excitation used for numerical analysis by (Ayoubi et al. [2018]), and we are trying to resemble it using two Ricker wavelets. The input motion is derived using de-convolution of East-West component of recorded acceleration at KTP (see Figure 2.25) by assuming a 1D column of depth b. By summing the two

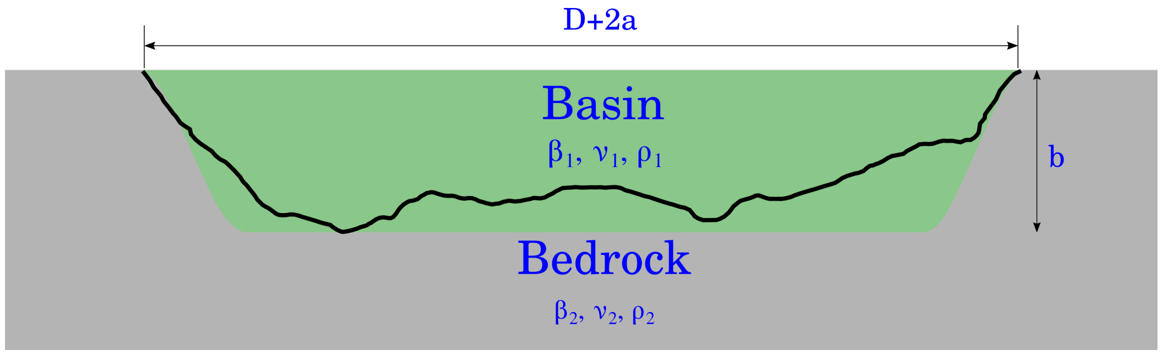

Figure 2.25: A HC-shaped basin is used in this study. The dashed line shows the basin's realistic geometry, which was used to find the corresponding simplified version in the current study.

Ricker wavelets, we cover a wider range of frequencies. In Figure 2.26-b, we show the Low Frequency (LF, in dotted blue line) and High Frequency (HF, in dashed red line) components of input motion. These two are summed to produce the incident plane wave that the idealized basin is subjected to ("Sum Incident Motion" in the Figure 2.26-a and b). The time series of each wavelet and the "Sum Incident Motion" are shown in Figure 2.26-a.

We assume that the basin is made of an elastic isotropic material with properties listed in Table 2.5. The bedrock properties are adopted from Wei et al. [2018], and the basin shear wave velocity is calculated using 1D velocity profiles published by Bijukchhen et al. [2017] beneath the strong motion stations shown in Figure 2.24. The profiles are shown in Figure 2.27. We average the three profiles to estimate a 1D approximation of the sedimentary structure inside the basin. This 1D approximation is later used to calculate the weighted average shear wave velocity for the simplified basin model.

Parameters						
π_1	π_2	π_3	π_4	π_5	π_6	π_7
0.333	0.2441	3.6	6.4	0.312	0.79	11.15

Table 2.5: Basin and halfspace parameters with reference to dimensional analysis of section 2.3.

Figures 2.28 and 2.29 show results of our analysis. Figures 2.28-a and 2.28-b portray surface AF of horizontal and vertical components, respectively. Basin edge effects can be readily observed in the form of localized ground motion amplification (more than 3 with respect to the free field) and strong spatial variability. This happens due to a complex wave interaction inside the basin. Such a complex spatiotemporal variation of the wavefield can

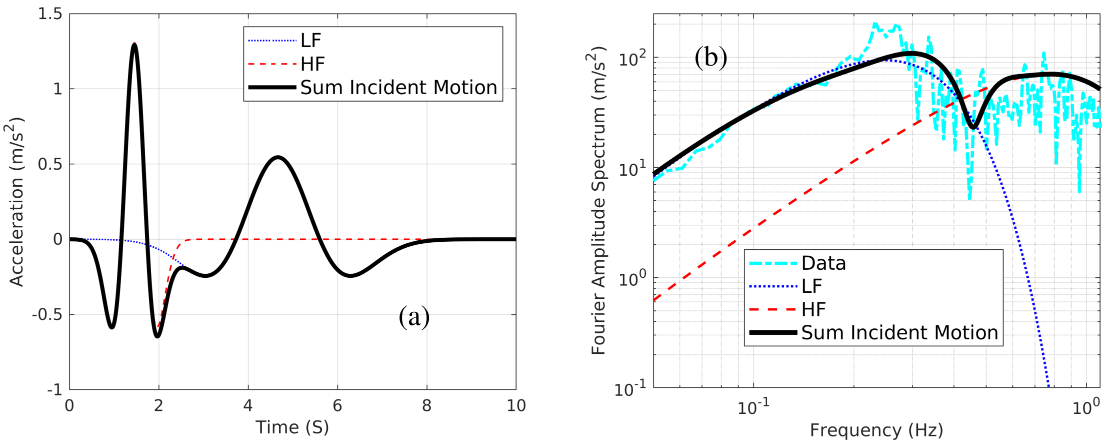

Figure 2.26: Fourier spectral amplitude of incident motion from Ayoubi et al. [2018] (dashed cyan line) and the current study (thick black line). The low frequency (LF, shown in dotted blue line) and high frequency (HF, shown in red dashed line) show two Ricker wavelets that are combined to derive the input for the numerical simulation.

be better perceived by seismogram synthetics of Figures 2.28-c and 2.28-d. An elongated motion, a strong vertical component, and a constructive wave interference are among the reasons for such a complicated behavior. Note that the input motion we use here is a train of two Ricker wavelets, and this complexity would be further accentuated in the case of a broadband seismic incident motion.

Figure 2.29 shows a comparison between the amplification factor in the frequency domain for the simplified basin of this study and the ground motion recordings from a strong-motion array in Kathmandu during the M_w 7.8 Gorkha mainshock (Takai et al. [2016]). Note that a comparison between waveforms (time-series) would not be possible since we use a synthetic input (a train with two Ricker wavelets, Figure 2.26) instead of a broadband earthquake acceleration. Moreover, the comparison is not shown for $> 1Hz$ since the model cannot capture a high-frequency portion of surface ground motion due to the lack of detailed stratigraphy and material information that would manifest in high frequency. As can be seen, the simplified HC basin model can capture the characteristics of the complex ground motion records with acceptable accuracy in the frequency range of $< 1\ Hz$. We should also highlight that the response at station TVU is governed by basin edge effects due to its proximity to the outskirts of the basin; thus, in the absence of detailed geometry representation of the basin edge, the predictive capabilities of the idealized model in Figure 2.29-a are less clear than in the case of Figures 2.29-b and -c.

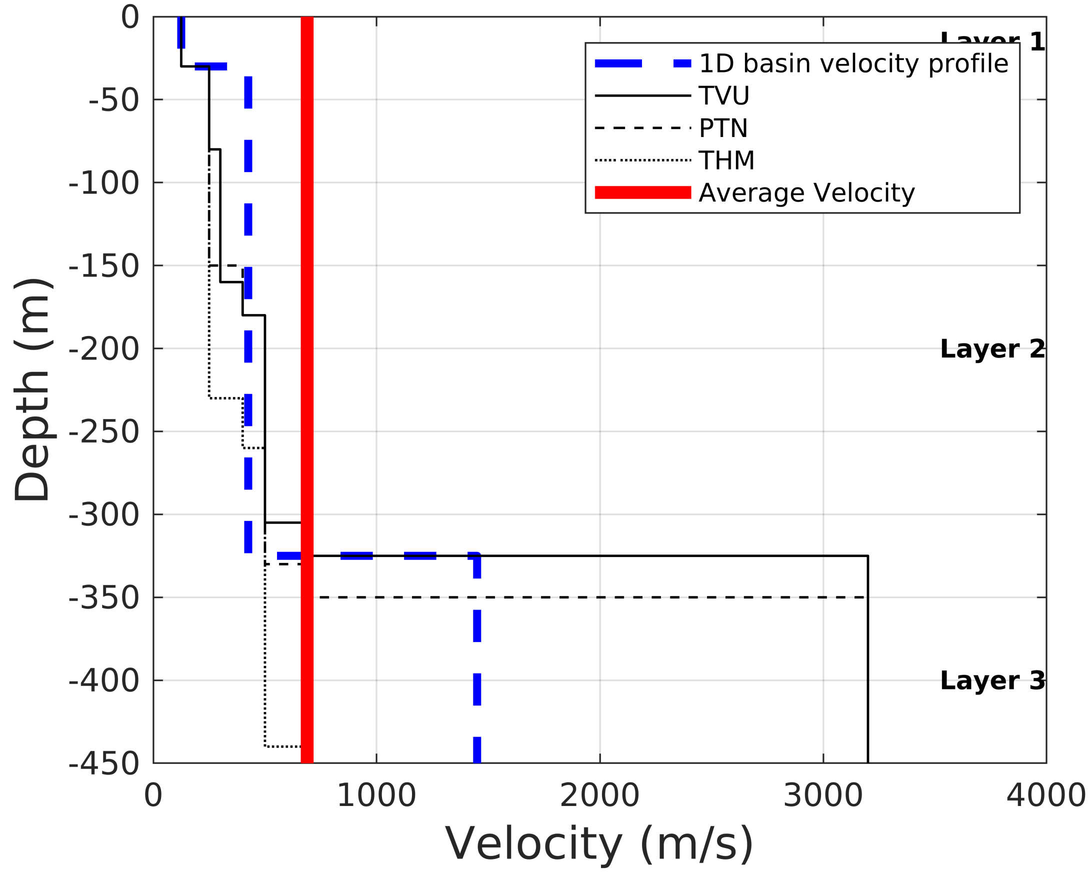

Figure 2.27: Black lines show the 1D velocity profiles by Bijukchhen et al. [2017]. The blue line shows the averaged and smoothed velocity. We temporally averaged the "1D basin velocity profile" (blue line) to obtain a single value for the shear wave velocity of the basin (red line).

2.5 Summary

This chapter performed an extensive parametric study to examine the coupled effects of material properties, interface geometry, and ground motion characteristics on the ground surface response of sedimentary basins. The simulations were carried out only for the case of vertically propagating SV wave of Ricker type. For all the simulation, we ignored the impact of source and incident angle in order to simplify the problem in hand. Our goal is to prioritize the parameters affecting the surface ground motion associated with basin effects by limiting the number of parameters that can reasonably take basin effects into account for seismic design codes and GMPEs. These could be used to devise a spatially varying aggravation factor curve for a specific site or could also be used as inputs to train a neural network to analyze surface motion on a basin. However, the output of these simulations are not able to account for how the source parameters, including incident angle

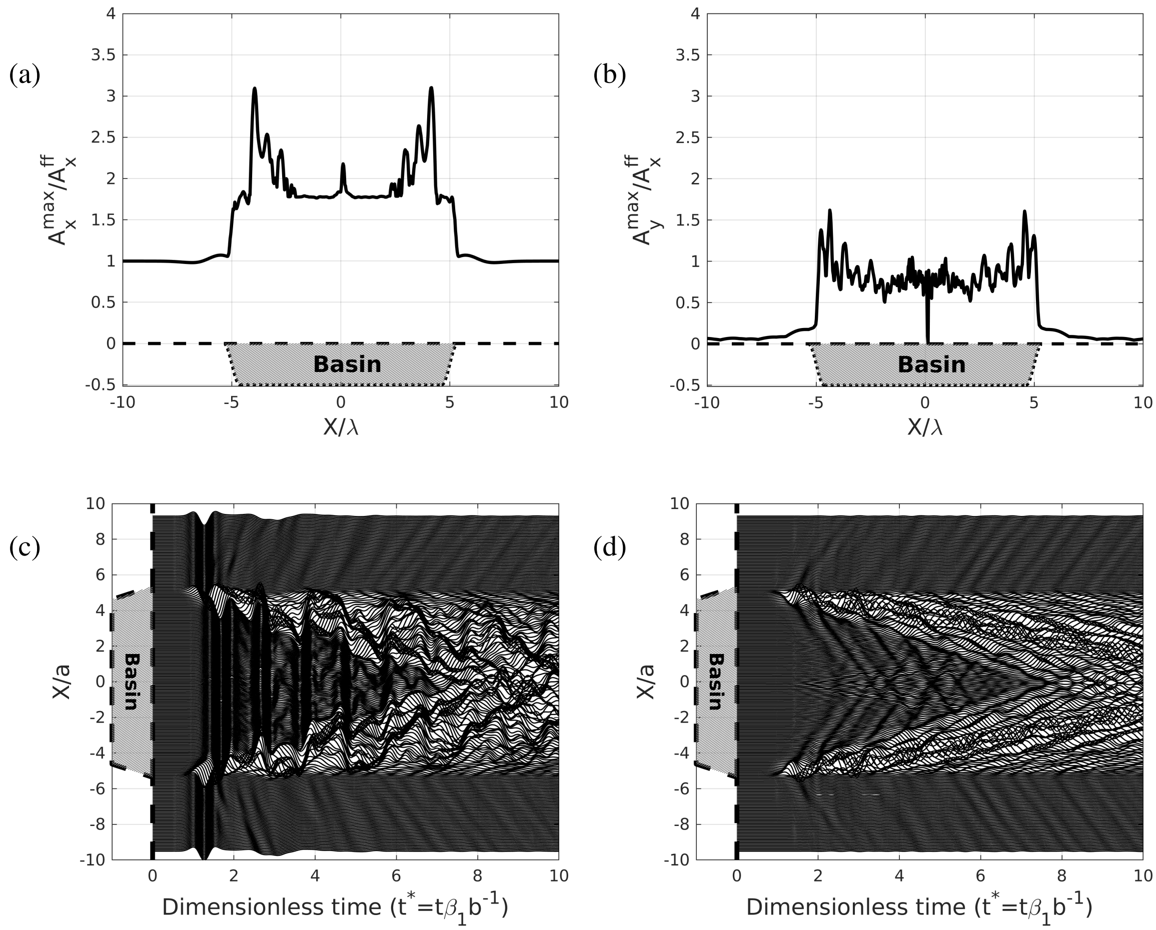

Figure 2.28: Kathmandu Basin response: a) Horizontal AF, b) vertical AF, c) Horizontal SS, and d) Vertical SS.

and distance from the basin, would impact the basin response. It was shown that in Gorkha Earthquake, the earthquake source was producing high-frequency response in a down-dip location and the long distance between the location of high-frequency component of the rupture and Kathmandu city was one of the main reasons that surface response was mainly low-frequency signal inside the basin (Avouac et al. [2015]). Such an observation is not feasible based on the set of simulations performed in this chapter.

We first investigated a simple dipping layer. The calculated surface motion shows that the coupled effect of material contrast and basin-edge can drastically change the wavefield compared to a flat ground with no irregular subsurface and produce a substantial vertical motion even when the incident motion is purely horizontal. We then defined two idealized geometries (Semi-Elliptical, SE, and Half-Cosine, HC). We studied their effects for elastic media subjected to vertically propagating SV waves of Ricker type using four dimensionless

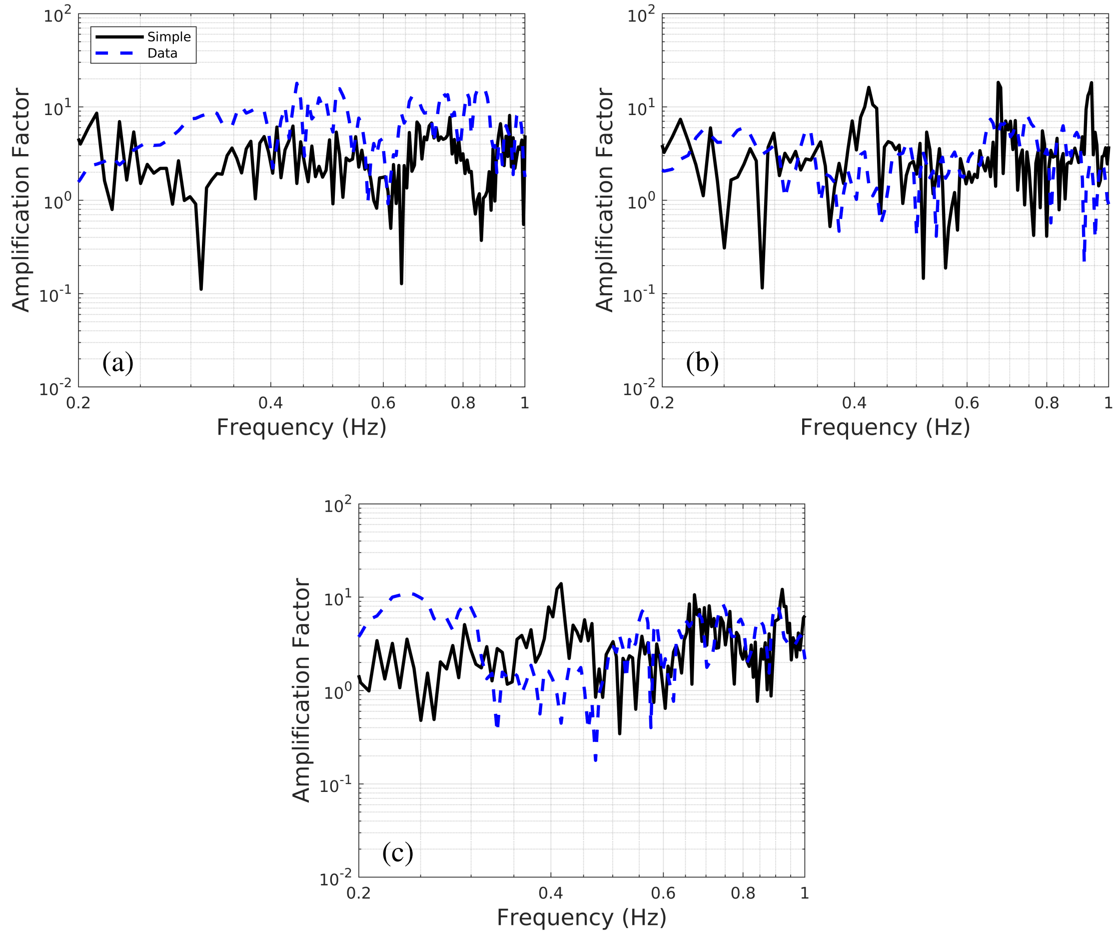

Figure 2.29: Comparison of simple HC basin ("Current Study"), and recorded motion during the mainshock from Takai et al. [2016] for a) TVU station, b) PTN station, and c) THM station.

parameters: aspect ratio (AR), dimensionless frequency (η), material contrast (β_2/β_1), and dimensionless width (ζ). Note that the materials assumed to be homogeneous for all the simulations of this chapter. Although depth dependency is an important aspect of realistic basin analysis, it is not something that is taken into consideration in practice. There are a couple of reasons for that: 1) the level of required information in order to include depth dependency of material is significantly higher than a homogeneous case. In some regions with sufficient soil material testing, empirical shear wave velocity profiles was developed (for example for California (Shi and Asimaki [2018])). However, this is not universal as most regions lack enough information in order to generate such curves. 2) If there exists a well-defined velocity profile for a basin, one is able to perform a deterministic numerical simulation specific to the region. The use of a generic dimensionless framework to calculate surface response of a basin is of less importance in such situations.

We first studied AR, a key parameter in describing the geometry of basin edges. We observed that the location and magnitude of maximum horizontal amplification depend on AR; and that for the same AR, SE and HC edge geometries can yield different amplification patterns. The parameter η measures the relative size of a basin to the dominant wavelength. For lower values of η, an incoming wave treats the basin as a whole (very low η motions completely "miss" the basin). In contrast, very high η motions interact only locally with the basin edges. By increasing η, the spatial variation of amplification factor (both horizontal and vertical) enhances, and the AF changes over shorter distances. Our results show that $\eta = 0.125$ had the most negligible impact on the amplification factor, and the response approximated half-space conditions. We next considered material contrast between soil and rock (β_2/β_1), a parameter that controls the energy that enters the basin and regulates the wave speed in each medium. Increasing material contrast generally resulted in a higher amplification factor due to the entrapment of earthquake waves within the basin and longer duration. Last, we considered the dimensionless width parameter (ζ) and showed that it could change the wave interference pattern by separating the whole basin into two 2D problems (corner half-cosine). We observed that for $\zeta \geq 5$, the basin behaves as two decoupled dipping layers with minimal interactions. Finally, we showed that the edge geometry plays a significant role in shaping the surface motion and basin wavefield and recommended a cosine-shaped basin edge for idealized basin simulations.

Our results show that dimensionless frequency, material velocity contrast, and aspect ratio are the most influential among the seven dimensionless parameters we investigated. The dimensionless width (ζ) was shown to be less effective than the three parameters mentioned above, which is expected since it stands as a proxy for lateral wave reverberations while the scenarios we examined involved vertically propagating incidence. Other dimensionless parameters such as density contrast, Poisson's ratio, or low-strain damping were shown to play a secondary role in this case. This conclusion can be crucial in developing parameterizations to integrate complex, non-1D phenomena such as basin effects in data-driven models such as ground motion prediction equations (GMPEs).

In the last section of the chapter, we approximated the shape of the Kathmandu basin, Nepal, with an idealized HC 2D basin and studied its response compared to the 2015 M_w 7.8 Gorkha Earthquake observations. We presented the amplification factor computed and recorded on the four strong ground motion stations in the basin and showed that even a simplified model could reproduce key features of the recordings associated with basin effects. We asserted that a more complex model would be required to study the physics of the phenomenon in more detail by incorporating source effects, 2D or 3D basin geometry models, layering, and nonlinear site response.

Our findings show that basin effects can satisfactorily be captured by proxies of three parameters, η, β_2/β_1, and AR. Currently, the most up-to-date GMPEs incorporate basin (really, 1D site) effects through the use of V_{s30} (average shear wave velocity in top 30 meters) and Z_1 (depth to shear wave velocity 1 km/s). At the same time, there is evidence that the two parameters can be correlated within the confines of similar geologic units (Abrahamson and Silva [2008]). This would ignore the important contribution of basin-edge effects that significantly altered the basin surface response during past earthquakes. Our experience shows that parameters η or β_2/β_1 could help improve GMPE parameterization for both 1D and non-1D conditions while including a basic measure of basin geometry such as AR should be investigated as a means of decreasing aleatory uncertainty associated with site effects in sedimentary basin settings.

Chapter 3

Time-series Estimation Using Neural Network: Application of Basin Effects

Although design codes and GMPEs have acknowledged the importance of basin effects, they have not yet fully incorporated the phenomena. This is primarily due to the lack of seismic data on sedimentary deposits and the complexity of the problem. The current state of practice is to use the shear wave velocity of the top 30 m (V_{s30}) of a soil column, and the depth at which the shear wave velocity reaches 1000 $^m/_s$ (Z_1) to take basin effects (and local site effects in general) into account. However, combining these two parameters is insufficient to capture $2D$ and $3D$ effects, especially the basin edge effect, as mentioned in the previous chapter. To reconcile the issue, some suggest using a multiplicative factor to modify the output, which is site-specific and requires generating aggravation curves for every site. Hence, a more accurate and generic procedure is needed to better incorporate basin effects for seismic analysis. In this chapter, we propose a new approach by which one will be able to estimate surface ground acceleration time-series in a basin with a minimal computation cost and few input parameters. We train a Neural Network (NN) to compute the transfer function of acceleration time-series at a location. Three input parameters are needed for the estimation: the basin-to-bedrock shear wave velocity ratio, the aspect ratio of the basin, and the dimensionless location. These parameters define an idealized-shaped basin and the location at which the time-series are to be computed. We will show that the model performs well compared to a full-fidelity FE simulation (ground truth) and generalizes well for input parameters outside of the training dataset. Moreover, we will also use the model for the case of Kathmandu Valley, Nepal, during the 2015 $M_w 7.8$ Gorkha Earthquake to test its generalizability similar to Chapter 2.

Contents of this chapter

3.1 Introduction

GMPEs relate an intensity measure at a site to parameters that define the source, path, and site characteristics. Douglas [2019] made a summary of GMPEs for the past 55 years and showed that the Peak Ground Acceleration (PGA) is the most common intensity measure that has been used in GMPEs while Peak Ground Velocity (PGV) and response spectra are second and third. While methods like aggregation factor (Riga et al. [2016, 2018]) have been proposed to take basin effects into account, GMPEs and design codes gravely rely on 1D site response by using V_{s30} and Z_1, to account for local site effects in their framework. This procedure cannot fully capture the wave interference within a basin (Ayoubi et al. [2021]) and in particular basin-edge effects.

The inclusion of site effects in design codes and GMPEs has always been a challenge due to the complexity of the phenomena and the lack of empirical data. Nowadays, with the advancement of computational resources and data analytics, synthetic data is an alternative that can be used to back up empirical information. Using Finite Difference (FD) and Finite Element (FE) methods to perform a full-fidelity analysis is one alternative to simulate a complex geometry subjected to a seismic scenario. Such an approach, although accurate, is computationally expensive and requires a lot of information about the geometry and material properties in a basin. A more efficient method is to use an aggravation factor. An aggravation factor is a multiplier applied to the result of 1D site response to approximate 2D effects in a seismic hazard assessment (Riga et al. [2016, 2018]). However, aggravation factors are site-specific and require a new set of synthetic or empirical data for each site or region. Therefore, a generic (not site-specific) procedure that is able to simultaneously take into account the complex wave interference in a basin and have a negligible computational cost is beneficial for seismic hazard analysis. The importance becomes pronounced when a fast and accurate calculation of basin response is desirable, such as in Earthquake Early Warning (EEW) systems (Minson et al. [2019]).

In past years, there has been a surge in the application of Machine Learning (ML) and Neural Networks (NN). ML techniques have shown significant success in image classification (Vasuki and Govindaraju [2017]), natural language processing (Jozefowicz et al. [2016]), computation vision (Voulodimos et al. [2018]), to name but a few (LeCun et al. [2015]). In seismology and earthquake engineering, they have been used to tackle complex problems as well, namely phase picking (Mousavi et al. [2020]), earthquake data inversion (Yang and Ma [2019]), structural health monitoring (Bao et al. [2019]), among others. In this chapter, we train a NN model on synthetic data through which one is able to generate a time-series of surface acceleration at a specific location on the surface of an idealized-shaped basin. We define basin geometry, material properties, and earthquake frequency content similar to the previous chapter in a dimensionless form. We particularly use shear wave velocity contrast, aspect ratio, and dimensionless location as three input parameters to train a NN. The model's output is the transfer function defined as the Fourier transform of surface acceleration time-series divided by the Fourier transform of rock outcrop. In the following sections, we first introduce the numerical toolbox. We then detail the data generation, data processing, and architecture of NN. We next describe the training details. Finally, we discuss the accuracy of the trained model and evaluate its performance using a test data set and applying it to a realistic scenario.

3.2 Data Generation and Methods

In this section, we focus on the data collection and training NN models. The data is generated synthetically using FE simulations (§ 3.2.1). For data generation, we follow a procedure based on the results of the previous chapter. In the last chapter, we performed a comprehensive parametric study to evaluate the importance of each parameter on observed acceleration on the surface of an idealized basin subjected to vertically propagated plane SV wave of Ricker type. We concluded that three dimensionless parameters (using Buckingham's PI theorem (Buckingham [1914])) are of primary importance on basin surface acceleration and variation. These dimensionless parameters are:

$$\pi_1 = AR = \frac{a}{b}, \quad \pi_2 = C = \frac{\beta_1}{\beta_2}, \quad \pi_3 = \eta = \frac{b f_0}{\beta_1}. \tag{3.1}$$

Figure 3.1 shows a representation of each parameter. f_0 is the dominant frequency of the incoming Ricker wavelet. We studied $AR = 0.5, 1, 2, 4$, $C = 1.5, 2, 3.5, 5$, and $\eta = 0.125, 0.25, 0.5, 1, 2, 4$. AR shows how shallow or deep a basin is and quantifies the basin corner angle, directly correlated with the basin-edge effect. C takes material contrast into account and measures the amount of energy entrapment inside a basin. Lower values of C result in a large entrapment. Finally, η demonstrates the relative size of a basin to the incoming wavelength, where small and large values make the incoming wave "blind" to the basin. As mentioned in Chapter 2, there are other parameters than the three mentioned above that impact the accuracy of basin analysis even in an idealized scenario. However, due to practicality and ease of use, these parameters are chosen to train a NN.

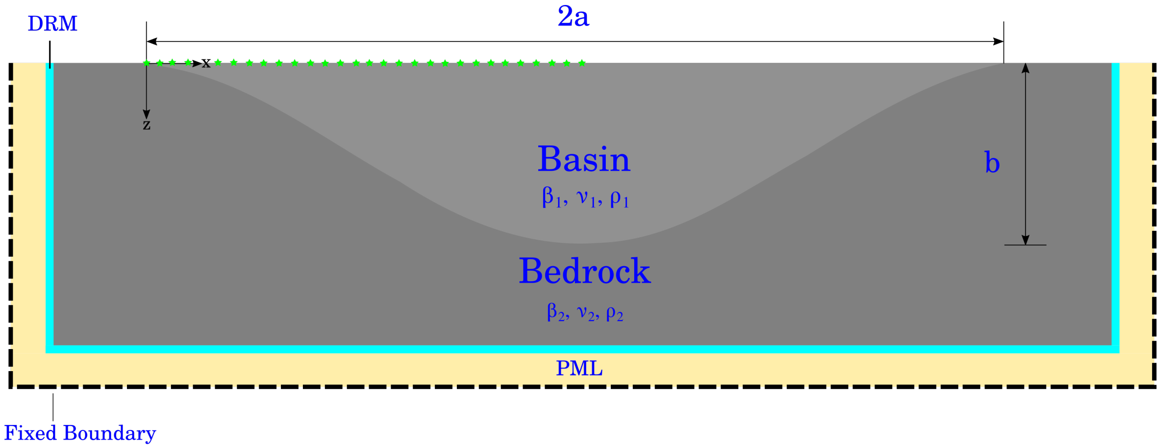

Figure 3.1: Schematic view of FEM domain together with DRM layer and PML boundary condition. The coordinate system is located at the basin corner.

3.2.1 Details of Numerical Toolbox

We perform a set of FEM simulations to generate the synthetic data for training the NN. The simulations are carried out using SeismoVLAB (Kusanovic et al. [2020]) in a 2D elastic, isotropic, and homogeneous medium. SVL is an open-source, easy-to-use, fast, and extendable C++ finite element code that is designed to optimally perform linear and nonlinear wave-propagation simulations in meso-scale. The software offers various options such as dynamic solvers for time-domain analyses of inelastic problems, Perfectly Matched Layer (PML) to efficiently mimic realistic scenarios. More information about the code can be found on its website: `https://seismovlab.com/`.

The domain includes two materials to demonstrate basin and bedrock. Basin is geometrically symmetric and follows a half-cosine shape as explained in the previous chapter, similar to Figure 3.1. We discretize the domain using quad elements, where 15 elements per shortest wavelength are used to satisfy the CFL condition. The input motion is applied using Domain Reduction Method (DRM), and the Perfectly Matched Layer (PML) is prescribed at side and bottom boundaries to absorb scattering waves. The PML (yellow area in Figure 3.1) is prescribed with a thickness of 25 elements to assure the total absorption of scattered waves. Each numerical model is defined using two dimensionless parameters (C, AR) related to basin material properties and geometry. We also define $\hat{x} = {}^{x}/_{a}$ to consider location of interest on a basin surface. The interface of basin and bedrock follows Eq. 3.2 as a function of x:

$$b(z) = \frac{b}{2}[1 + cos(\frac{\pi x}{a})] \qquad |x| \leq a. \tag{3.2}$$

Note that in Chapter 2, we introduced a parameter D as in Figure 2.6. We omit D in this chapter and assume $D = 0$. The medium is subjected to a vertically propagating plane SV wave. The input is prescribed as DRM components along a one-element stripe shown by cyan in Figure 3.1. The input motion is a Ricker wavelet with dimensionless frequency (η) between zero and 5 for all the models. Dimensionless frequency is defined as $\eta = {}^{fb}/_{\beta_1}$, where f shows the frequency range of incoming motion. This is a difference between the current and the previous chapter. Here, instead of defining a single dimensionless frequency (η), we define a range of η for each model.

3.2.1.1 Data Set and Preprocessing

For training, synthetic data is generated by performing a set of numerical simulations and various dimensionless parameters, namely $AR = {}^{a}/_{b}$, and $C = \beta_1/\beta_2$ (see Figure 3.1 for each parameter). Note that in this study, we assume a fixed range of η for all models ($0 \leq \eta \leq 5$). We randomly chose parameters in a range of $0.5 \leq AR \leq 15$, and $0.1 \leq C \leq 1.0$ and perform a FEM simulation.

On the surface of a basin, 20 locations are selected, spanning from a basin corner to the basin center due to symmetry (green stars in Figure 3.1). The x coordinate of each location is normalized by a, meaning basin corner has $\hat{x} = x/a = 0$ and center has $\hat{x} = 1$. Simulations are performed for a fixed duration of 150 $[sec]$ assuming the vertical distance between the bottom DRM strip and deepest part of a basin is the same in all models. Simulations stop when the amplitude of acceleration is negligible. This guarantees roughly the same wave arrival time to the basin for all the models. Therefore, for each set of (AR, C, $\hat{x}$), a unique acceleration time-series with $\eta \in [0, 5]$ with the length of 150 $[sec]$ is obtained. For training, instead of learning time-series directly, we learn transfer function corresponding to a $\hat{x}$ on the basin surface. The transfer function is defined as:

$$TF(AR, C, \hat{x}) = \frac{FFT(AR, C, \hat{x})}{FFT_{ff}} \tag{3.3}$$

where $TF(AR, C, \hat{x})$ is transfer function at location $\hat{x}$ on surface of a basin with AR and C, $FFT(AR, C, \hat{x})$ is the complex Fourier transform of a time-series (using fft algorithm), FFT_{ff} shows complex Fourier transform of rock outcrop. Decomposing the transfer function into its amplitude and phase vectors, we will develop one separate model for each of them. Note that the network for training phase vectors does not take into account the circular nature of the phase, i.e. there is a 2π periodicity. Due to the capability of NN to learn complex systems, this should not an issue. After generating the dataset, we use 80%, 10%, and 10% of data for training, validation, and testing, respectively.

As can be seen in Eq. 3.4, given each input (x_{i1}, x_{i2}, x_{i3}, matrix X), we want to predict amplitude (shown by a_{ik}, matrix A) and phase (shown by p_{ik}, matrix P), where F shows a mapping from a set of input to either amplitude (mapping F_1) or phase array (mapping F_2).

$$F(X) = F(\begin{bmatrix} x_{11} & x_{12} & x_{13} \\ x_{21} & x_{22} & x_{23} \\ \vdots & \vdots & \vdots \\ x_{n1} & x_{n2} & x_{n3} \end{bmatrix}) = (\begin{bmatrix} a_{11} & a_{12} & \dots & a_{1d} \\ a_{21} & a_{22} & \dots & a_{2d} \\ \vdots & \vdots & \ddots & \vdots \\ a_{n1} & a_{n2} & \dots & a_{nd} \end{bmatrix}, \begin{bmatrix} p_{11} & p_{12} & \dots & p_{1d} \\ p_{21} & p_{22} & \dots & p_{2d} \\ \vdots & \vdots & \ddots & \vdots \\ p_{n1} & p_{n2} & \dots & p_{nd} \end{bmatrix}) = (A, P) \tag{3.4}$$

To do that, we train two separate models F_1 (Eq. 3.5) and F_2 (Eq. 3.6) to estimate amplitude and phase values, respectively.

$$F_1(x_{i1}, x_{i2}, x_{i3}) = [a_{i1}, a_{i2}, a_{i3}, \dots, a_{id}] \tag{3.5}$$

$$F_2(x_{i1}, x_{i2}, x_{i3}) = [p_{i1}, p_{i2}, p_{i3}, \dots, p_{id}] \tag{3.6}$$

Finally, the $TF(AR, C, \hat{x})$ is calculated as

$$TF(AR, C, \hat{x}) = F_1(x_{i1}, x_{i2}, x_{i3}) \times \exp(iF_2(x_{i1}, x_{i2}, x_{i3})). \tag{3.7}$$

This equation gives us a complex transfer function for the range of dimensionless frequency of interest ($0 \leq \eta \leq 5$). To reconstruct the time-series, focusing on positive frequencies, we assume zero values for $\eta > 5$. Given that the transfer function corresponds to a real-valued time-series, the real part should be symmetric about 0 dimensionless frequency. In contrast, the imaginary part of the transfer function should be anti-symmetric about the 0 dimensionless frequency. By constructing the real and imaginary part of the transfer function for positive dimensionless frequencies, we use the properties mentioned above of a real-values signal to reconstruct the negative frequency components and take an inverse Fourier transform to obtain the time-series at location $\hat{x}$ of the model with AR and C.

Before training, we preprocess the training data sets (X, A, and P). For features (X), we normalize them to have zero mean and unit variance to help with the convergence of the optimization method. For amplitude (A) and phase (P) data sets, we have found that performing a matrix factorization helps with the training process. We apply a Singular Value Decomposition (SVD) on both amplitude and phase matrices (Eq. 3.8 shows a representation of SVD). We decompose the matrix into a coefficient ($U\Sigma$) and basis (V^T) matrices. We do not include the basis matrix in the learning and only learn coefficients for a given set of input parameters. We assume that our basis matrix for training data provides an appropriate n-dimensional space representing the training data, as well as validation and test data sets. Later for testing, we use the same basis as the training dataset to assess the performance of the trained models on out-of-sample cases. Note that while SVD is generally used to obtain a lower rank representation of a matrix, we use all the data and do not discard any dimension.

$$A = U\Sigma V^T =$$

$$\begin{array}{cccccc} u_1 & & u_r & u_{r+1} & & u_m \end{array} \qquad\qquad\qquad\qquad\qquad\qquad\qquad\qquad$$
$$\begin{pmatrix} \Big| & & \Big| & \Big| & & \Big| \\ \Big| & \cdots & \Big| & \Big| & \cdots & \Big| \\ \Big| & & \Big| & \Big| & & \Big| \end{pmatrix} \begin{pmatrix} \sigma_1 & & & & \\ & \ddots & & & \\ & & \sigma_r & & \\ & & & \ddots & \\ & & & & \sigma_m \end{pmatrix} \begin{array}{c} \begin{pmatrix} \text{———} \\ \\ \text{———} \\ \text{———} \\ \\ \text{———} \end{pmatrix} \end{array} \begin{array}{l} v_1^T \\ \\ v_r^T \\ v_{r+1}^T \\ \\ v_n^T \end{array} . \tag{3.8}$$

3.2.2 Training the Neural Network

We use a Neural Network model to retrieve a time-series given three parameters as input (Eq. 3.9). This is going to be done through learning amplitude and phase of the corresponding transfer function

$$[Amp, Pha] = [F_1(AR, C, \hat{x}), F_2(AR, C, \hat{x})] \tag{3.9}$$

where Amp and Pha stand for amplitude and phase of a transfer function, respectively. In this study, both $Amp \in R^{251}$ and $Pha \in R^{251}$ for the dimensionless frequency range of 0 to 5 where each entry of the vectors corresponds to a specific dimensionless frequency. Since each entry of Pha and Amp corresponds to a specific dimensionless frequency, we do not

No.	Parameters		
	AR	C	$\hat{x}$
1	2.25	0.3	1
2	12.0	0.5	0.5
3	0.5	0.5	0.0

Table 3.1: Parameters to be used to test the models. All models are chosen from a holdout data set. Model #3 will be used with a new input motion.

include a frequency array in the learning process. For the network architecture, we use Residual Network (ResNet) units (He et al. [2016]). After hyper-parameter tuning, we use a batch size of 32, and Adam optimization algorithm (Kingma and Ba [2014]) with a learning rate of 2.5×10^{-3}. The network consists of an input layer of size 3, and three hidden layers. We use the same network architecture for training both amplitude (Amp) and phase (Pha).

Figure 3.2 shows the convergence of networks for training and validation data sets for each model. We early-stop the learning for Amp at 150 and for Pha at 150 epochs to prevent overfitting. The performance of the models and their generalization ability will be discussed in the next section.

3.3 Results and Discussion

This section first assesses model performance by choosing two cases from a holdout test data set. In addition, an example with a new input motion will be shown that is different from the input motion used for generating synthetic data (i.e., single Ricker wavelet). We also perform a case study to assess the seismic response of Kathmandu Valley, Nepal, during the 2015 M_w7.8 Gorkha earthquake and compare the results of trained models versus the recording, similar to the previous chapter.

3.3.1 Testing the Model

To assess the model's generalization ability, we use a hold-out (test) dataset. Our goal is to evaluate the performance of trained models in estimating TF, time-series, and corresponding response spectra. We separate the test into three categories. The first category comes directly from the hold-out data set. The second category includes one new FEM simulation with a more complex input motion.

Figure 3.3 shows the results of the first two cases of Table 3.1. The left column shows the

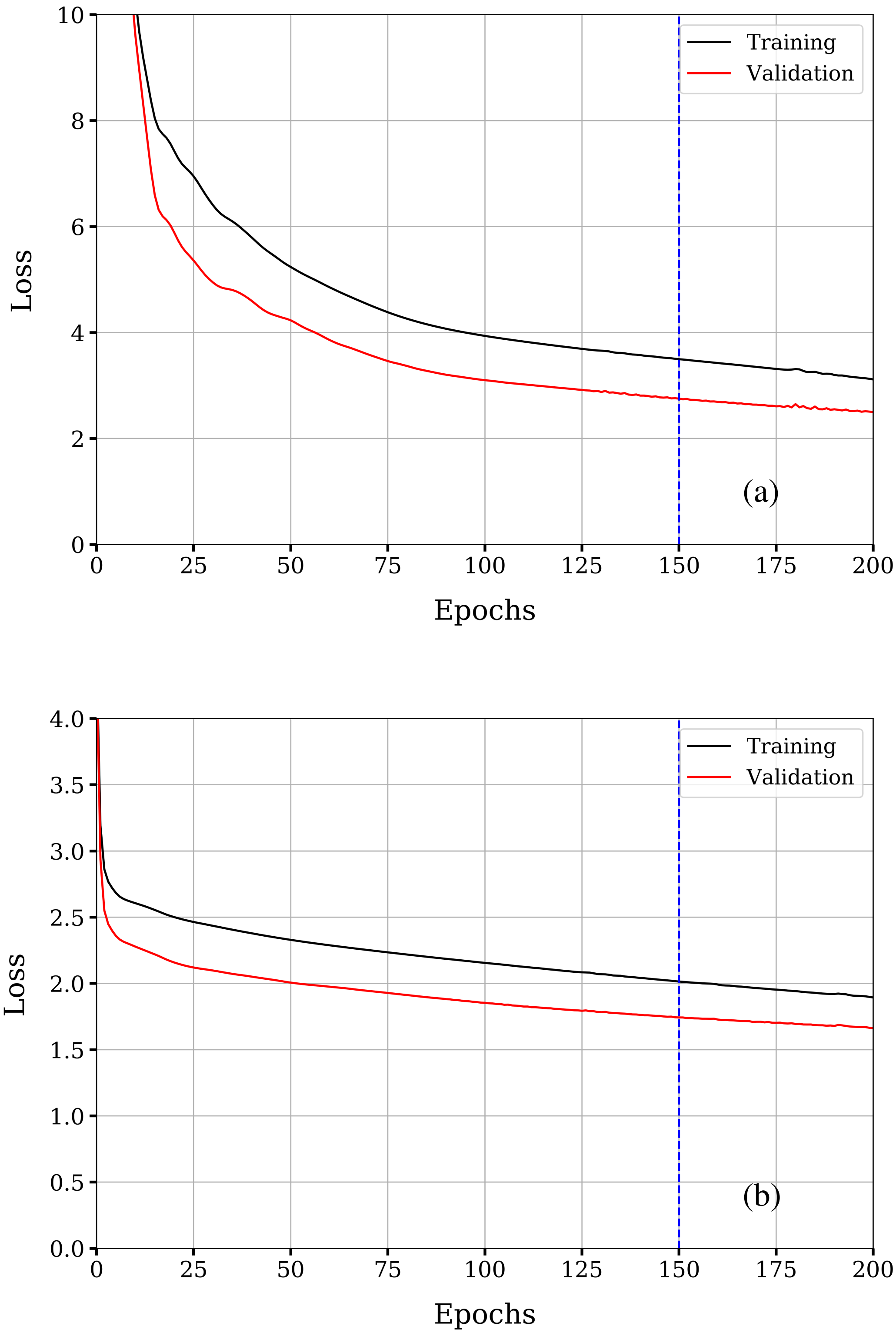

Figure 3.2: Convergence of two networks that are trained for learning amplitude and phase of transfer functions, a) amplitude, b) phase.

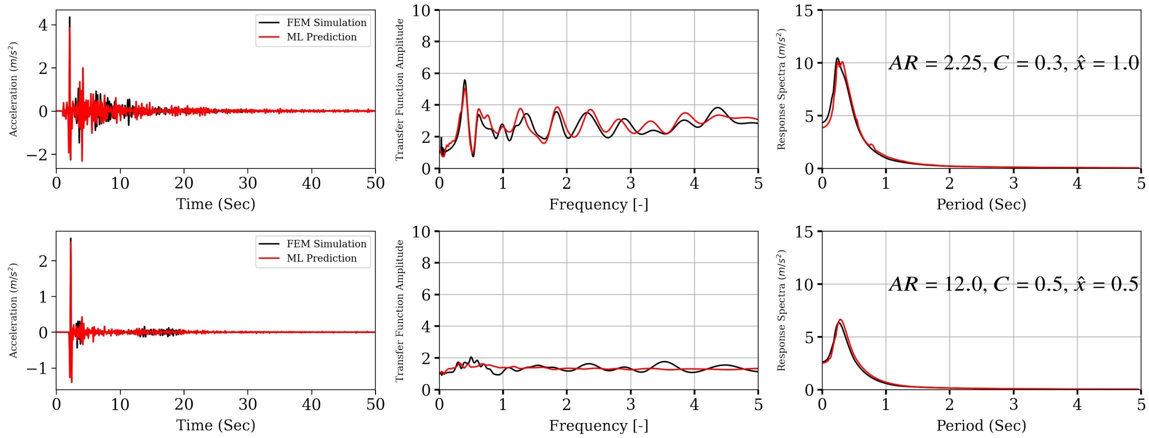

Figure 3.3: Comparison of NN results versus the FE simulations from test data set. Left column shows the time-series, middle columns shows transfer function amplitude, and right column shows acceleration response spectra. Model properties are shown on the right subfigures.

estimated time-series, the middle column portrays the amplitude of the transfer function, and the right column shows the response spectra of the estimated time-series. The black line indicates the ground truth (FEM results) in all the subfigures, and the red line shows ML prediction. The accuracy in these cases is satisfactory in comparison to the FEM results. For time-series, the overall trend and PGA are reconstructed accurately. In addition, we can capture variation in frequency and most of the picks for the amplitude of transfer function (this is the direct output of ML models). Not capturing all the picks does not significantly impact the reconstructed time-series as seen in the left column. This could be done by deploying a more complex model, but it could have resulted in overfitting. Finally, for the response spectra, the comparison shows a good performance of the models. The model can capture the values and the variation over different periods correctly. Note that the response spectra of acceleration is calculated from the reconstructed time-series of the left column.

For the second part, we want to investigate whether the trained models can generalize well. Therefore, we perform a new FEM simulation with input values drawn from the test set. The input motion to be used for the test is a Ricker train consisting of three Ricker wavelets with dominant frequencies of 1 $[Hz]$, 2 $[Hz]$, and 3 $[Hz]$, as is shown in Figure 3.4. Figure 3.5 shows the output of the trained model versus the FE simulation results. The columns are similar to Figure 3.3. Similar to the previous figure, we observe a satisfactory comparison between the ML predictions and FEM simulations. This shows that the model is capable of learning transfer functions accurately. Note that due to the linear nature of the problem, the reconstructed time-series could have been obtained by superposition of different models subjected to a single Ricker input.

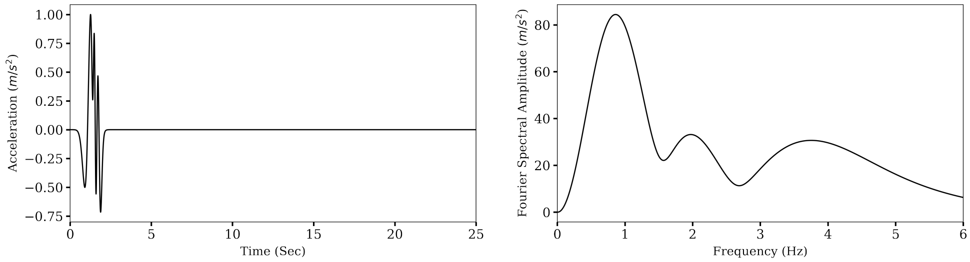

Figure 3.4: The new input motion that is used for testing the trained models. It consists of three Ricker wavelets with dominant frequencies of $1\ [Hz]$, $2\ [Hz]$, and $3\ [Hz]$, and different lags in time.

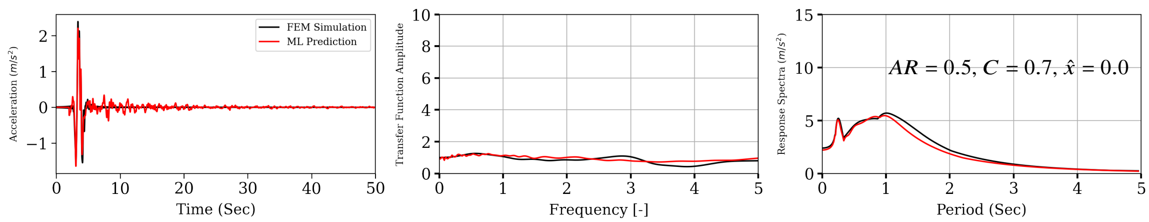

Figure 3.5: Comparison of NN results versus the FE simulations for a new set of parameters. The outputs are similar to Figure 3.3. The input is shown in Figure 3.4.

We apply the approach we have laid out throughout this chapter to a realistic scenario in the following subsection.

3.3.2 Kathmandu Basin, Nepal During the 2015 Gorkha Earthquake

As a final test, to assess the capability of our approach in capturing basin effect in a realistic scenario, we apply it to estimate the surface ground response in the Kathmandu basin, Nepal, during the 2015 $M_w 7.8$ Gorkha Earthquake. In Chapter 2, we performed a parametric analysis to study the capability of a homogeneous linear elastic basin to capture the surface acceleration associated with the mainshock of the Gorkha Earthquake. We concluded that a simple idealized-shaped model is able to capture some characteristics of surface motion in a low-frequency range. However, we also mentioned that such a model could not provide an accurate insight in a high-frequency range since the model is too simplistic. Therefore, a heterogeneous basin with an arbitrary geometry may be a more suitable model for higher frequencies. In Figure 3.6, the light green area is the idealized model we used in Chapter 2, and we fit a cosine-shaped model to it as shown by dark green (by removing the parameter D). Hence, we have a model with the same width, depth, and shear wave velocity. We use the dimensionless parameters from Chapter 2 to compute the three parameters needed for NN models. We then compare the Fourier spectral amplification amplitude of surface stations and compare it with the seismogram recordings

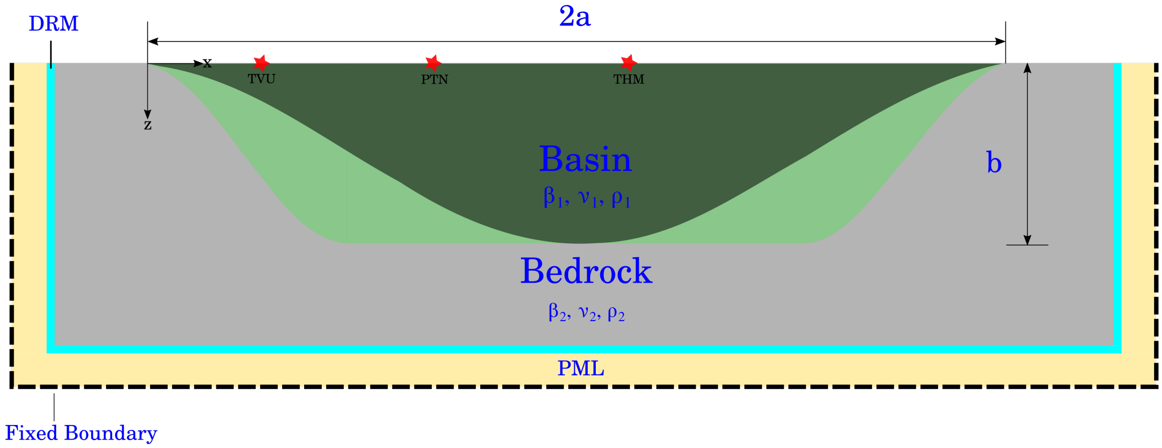

Figure 3.6: Schematic view of the basin we use for Kathmandu basin case study in this chapter versus Chapter 2. The dark green shows the geometry we use in this chapter. The light green is the one we used before.

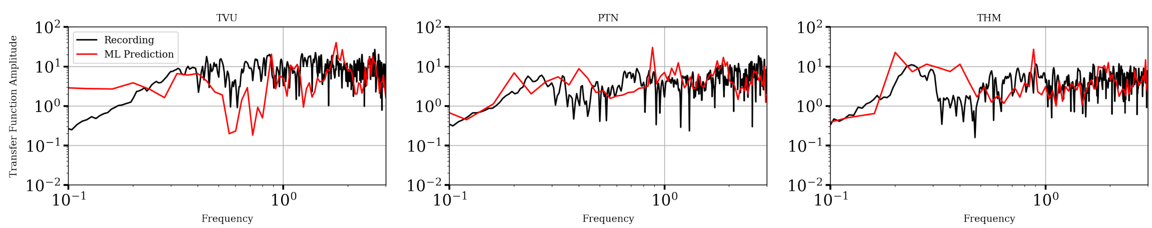

Figure 3.7: Comparison of results of current study versus recorded motion of Takai et al. [2016] at TVU (left), PTN (middle), and THM (right) stations.

at the three strong ground motion stations in the basin.

Figure 3.7 shows a comparison between the Fourier spectral acceleration amplification on basin surface for recorded data and the output of NN models. The amplification (similar to the transfer function we have used so far) is defined as the Fourier spectral amplitude at a location in the basin divided by rock outcrop Fourier spectral amplitude. Running the full fidelity FE simulation takes $\sim$ 3 hours on 4 cores of Intel(R) Xeon(R) CPU E5-2687W v3 @ 3.10 GHz, while calculating the output of the current study takes 0.8 $[sec]$. As can be seen, the estimation of current models is similar to the recordings. The other benefit of our ML models is that we can go to higher frequency ranges.

3.4 Algorithm to Generation Time-series

In section § 3.2.2, we provided mapping to obtain the transfer function of a system through which one is able to obtain time-series given three parameters as input. Algorithm 1 demonstrates the procedure we used in the § 3.2.2.

Algorithm 1 Time-series estimation.

1: The **initialization step**: Compute the dimensionless parameters for a site. In a general case, having width, depth, shear wave velocity of basin and bedrock suffices to obtain three input parameters.

$$AR = \frac{a}{b}, C = \frac{\beta_1}{\beta_2}, \hat{x} = \frac{x}{a}$$

see Figure 3.1 for the definition of each parameter.

2: The **input selection step**: Choose a time-series as a input motion acceleration.

3: The **prediction step**: Multiply the complex Fourier transform of input motion with the obtained transfer function from NN models to compute the Fourier transform of surface acceleration time-series.

4: The **inverse step**: Perform an inverse Fourier transform to obtain the time series at location $\hat{x}$.

3.5 Conclusion

In this chapter, we trained a Neural Network model to estimate surface ground acceleration associated with basin effects. We generate a synthetic data set of 2D basin simulations, assuming basin material is homogeneous linear elastic, and the geometry follows as idealized cosine-shaped. Our trained models were shown to perform well versus the full-fidelity FE simulations while it takes a fraction of a second in computational time. We concluded that the models are generalizable by performing two sets of testing. First, we assessed model performance for both a single Ricker input and a Ricker train by choosing some cases from a holdout test set. We also examined model performance in a realistic scenario by comparing the results of this chapter versus recordings of the 2015 $M_w7.8$ Gorkha earthquake. Our results show a satisfactory performance of the current approach.

Chapter 4

Monte Carlo Simulation to Study the Spatial Variation of Ground Motion Associated with Basin Heterogeneities

While past two chapters address how we are able to better incorporate basin effects in the seismic studies, a question still remains about how we can better simulate basin effects in cases with limited amount of data. This chapter presents the use of correlated random fields to study basin effects. We use a 2D finite element analysis of an idealized-shaped basin subjected to a vertically propagating SV plane wave and investigate the spatial variation of SGM associated with basin effects by assuming a correlated random field to represent basin material. We generate a random medium by adding perturbations to a homogeneous domain with various correlation lengths, coefficient of variations, and autocorrelation functions to evaluate their contribution to SGM. Our results show a difference between the output of homogeneous and stochastic models, where we conclude that the former would not represent basin response, especially in the high-frequency regime correctly. Among the parameters we consider, the coefficient of variation has the most influential impact on surface acceleration. We observe that increasing this parameter decreases the mean value of surface amplification while its standard deviation increases. In addition, correlation length affects the standard deviation of surface acceleration, but it does not significantly impact the mean amplification. As for the autocorrelation function, where we consider von Karman, Gaussian, and exponential, the results show that the trend of surface amplification does not change by choosing a different autocorrelation function. Finally, by comparing the 2D basin versus 1D layered medium, we show that one cannot accurately capture basin response by using a 1D analysis for seismic hazard quantification.

Contents of this chapter

4.1 Introduction

Numerical studies of basin effects require a detailed geotechnical and geological information as SGM rely on several parameters, namely bedrock depth (Dravinski [1982]), the frequency content of earthquake (Wong and Trifunac [1974]), material properties of basin and bedrock (Bard and Bouchon [1980]), among others (Ayoubi et al. [2021]). However, due to the limited availability of testing and empirical data, simplifying assumptions regarding geometry and material properties is widely adopted. In the bulk of the studies, a basin with homogeneous material (or a layered basin with a discrete velocity profile) is assumed (for example Moczo et al. [2018], Narayan and Kumar [2009]), and a single deterministic analysis is performed to analyze ground motion, similar to Chapter 2. This neglects the inherent heterogeneity in soil, and even a parametric study cannot fully account for it. This becomes important where an accurate simulation of a basin in high frequency is of interest.

Probabilistic modeling techniques and Monte Carlo (MC) simulations have been used in earth sciences (for example Frankel and Clayton [1984], El Habar et al. [2019]) and can address the issue mentioned above by gauging the uncertainty arising from soil material spatial variability, and testing and statistical errors (Popescu [2008]). In seismology, earthquake source modeling (Frankel and Clayton [1984], Mai and Beroza [2002], Zielke et al. [2017], Nakata and Beroza [2015]) and ground motion analysis (Frankel and Clayton [1984], Frankel et al. [2018]), among others, have been the primary usage of probabilistic approaches. On the other hand, engineers perform probabilistic studies to analyze liquefaction, site responses, to name but a few (Boore [2003], Assimaki et al. [2003], Rota et al. [2011], El Habar et al. [2019]). These studies generate a correlated velocity random field to take material heterogeneity into account. For site effects application, the main focus has been on 1D wave propagation, or a rectangular 2D medium (Rota et al. [2011], El Habar et al. [2019]), and the lack of such analysis for basin configuration is noticeable.

In a basin setting, two types of interaction are of interest. The first one occurs when a wave interacts with the basin as a whole (low-frequency interaction, as discussed in Chapter 2). The second one happens when a seismic wave interacts with heterogeneities within a basin (high-frequency interaction). The second interaction results in a different basin response depending on the frequency and size of stochastic features (Takemura et al. [2015]). The wave-basin interaction is easier to simulate, as has been done mainly in the literature (Kawase and Aki [1989], Narayan and Kumar [2009], Gelagoti et al. [2012], Ayoubi et al. [2021]). We followed the same approach in previous chapters, while wave-heterogeneities interaction is what most studies miss due to computational challenges, practicality, and insufficient geotechnical information. Neglecting the heterogeneities within a basin cannot

Basin Properties			Bedrock Properties		
Shear Velocity	Density	Poisson's ratio	Shear Velocity	Density	Poisson's ratio
$[\frac{m}{s}]$	$[\frac{kg}{m^2}]$	$[-]$	$[\frac{m}{s}]$	$[\frac{kg}{m^2}]$	$[-]$
250	2000	0.333	500	2000	0.333

Table 4.1: Basin and bedrock material properties in background medium.

be fully justified since it is known that small-scale heterogeneities can impact seismograms drastically through the broadening of body waves (Saito et al. [2005]), distortion of radiation pattern (Sawazaki et al. [2011]), and elongation of surface motion (Aki and Chouet [1975]).

This chapter analyzes the spatial variation of SGM associated with basin heterogeneities using a stochastic approach. We consider a 2D elastic basin overlying a bedrock subjected to a vertically propagating SV plane wave of the Ricker type. The basin geometry is assumed to be a generic form (half-cosine shaped like Chapter 3). We use a correlated random field to take the spatial variability of materials into account in the numerical simulations. Parameters such as correlation lengths, autocorrelation function (ACF), and coefficient of variation of a random field are varied to evaluate their impact on SGM. In the following sections, we first explain the correlated random field generation procedure. Next, we present the results and demonstrate how each parameter would affect the spatial variation of SGM. Finally, we show a comparison versus 1D analysis, which is the state of practice.

4.2 Monte Carlo Simulation

In this section, we first explain the FEM model. Next, we detail the random field generation procedure. The random field is generated on top of a homogeneous basin. This homogeneous background is called "background medium/model" throughout this chapter.

4.2.1 Finite Element Model

We are going to use SVL (Kusanovic et al. [2020]) similar to Chapter 3. We use elastic materials to represent a basin and bedrock. We neglect damping in the basin to prevent exhausting high-frequency energy of the seismic wave and better represent the impact of features on SGM. For the basin configuration, we choose a generic cosine-shaped basin, similar to Figure 4.1. Table 4.1 shows the material properties of the background medium, which will be used to generate the correlated random field (details in § 4.2.2).

The geometry of the basin is derived based on the dimensionless analysis performed in

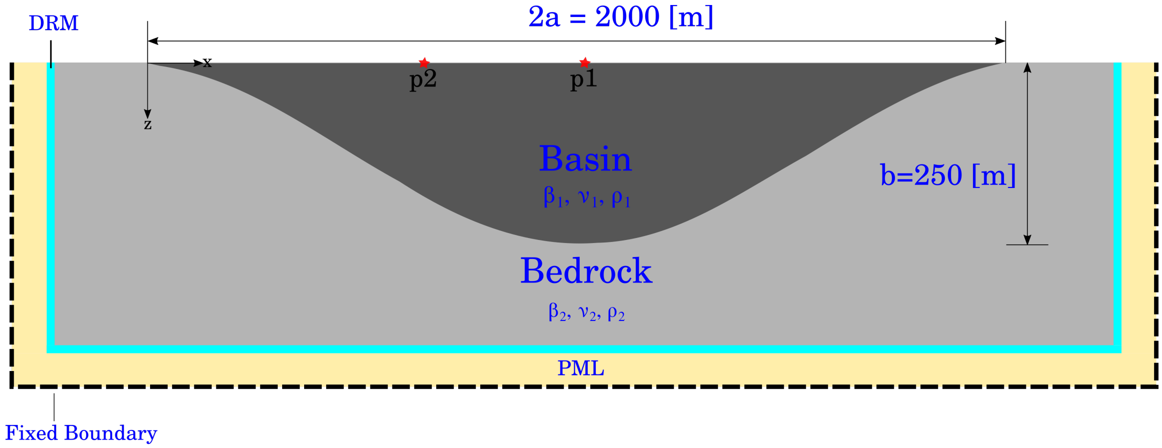

Figure 4.1: The numerical domain. The dark gray area represents the basin. The light gray shows the bedrock. Cyan and yellow regions demonstrate DRM and PML, respectively. The external boundary is fixed. Two red stars show the location at which we will show results later in this chapter: in the basin middle, halfway between center and corner.

Chapter 2. We use following dimensionless parameters to define the model: aspect ratio $AR = a/b = 4.0$, material contrast $C = \beta_2/\beta_1 = 2.0$, density ratio $\rho_2/\rho_1 = 1.0$, Poisson's ratio of basin $\nu_1 = 0.333$, and Poisson's ratio of bedrock $\nu_2 = 0.333$. The input motion is shown in Figure 4.2 which is a Ricker wavelet with the dominant frequency of $5\,Hz$. We expect two separate interactions that might occur inside a basin, namely 1) wave-basin interaction and 2) wave-features interactions in horizontal and vertical directions. The reason for choosing $5\,Hz$ as the dominant frequency of the input motion is the availability of sufficient energy at both low and high frequencies. This means that the Fourier spectral amplitude of input motion has enough energy to interact with the heterogeneities inside a basin.

We use 15 quad elements (each having size of dx) per shortest wavelength in a domain to resolve maximum frequency to discretize the numerical domain. We also satisfy CFL < 0.25 condition by assuming $dt = 0.005$. Perfectly Matched Layers (PML) with a length of $25 \times dx_{bedrock}$ are prescribed at the side and bottom boundaries to absorb scattered wavefield. The outer boundary of PML is fixed. Finally, the input motion is applied using Domain Reduction Method (DRM) at the cyan shaded region of Figure 4.1.

4.2.2 Random Field

In a deterministic scenario, due to a lack of sufficient information about soil mechanical properties, one needs to either assume fixed material properties for a basin or adopt a layered velocity profile. However, the Earth's crust is far from being homogeneous or isotropic, the reason we are using a random field to describe the material inside a basin. This does not

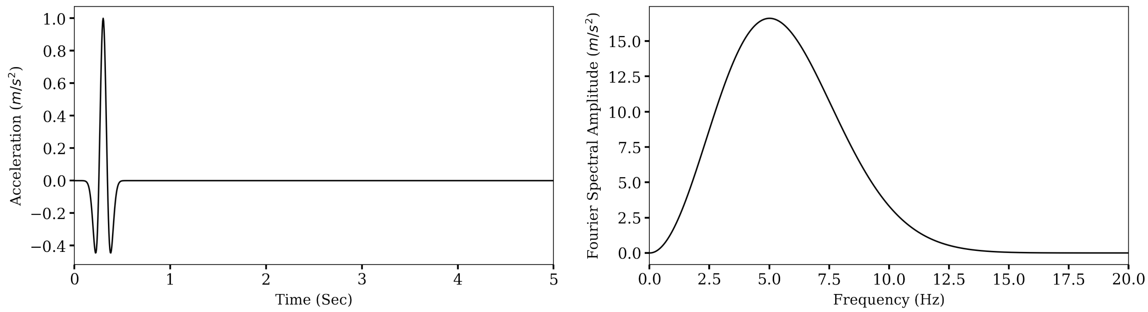

Figure 4.2: Input acceleration time-series (left) and corresponding Fourier spectral amplitude (right).

mean that the basin is a fully randomized medium while correlations exist. The correlated random field we are using in this chapter requires 5 parameters, namely 1) mean (μ), 2) Coefficient of Variation (COV), 3) Autocorrelation functions (ACF), and correlation lengths in 4) horizontal (θ_x) and 5) vertical (θ_z) directions. In practice, for a geotechnical application, skewed distributions are used for shallow layers and a symmetric distribution for deep (Popescu et al. [1998]). In this study, given the depth of the basin, we utilize a symmetric distribution. In addition, due to the arbitrary geometry of the basin (as opposed to a rectangular domain), we use Karhunen-Loève expansion to generate a correlated random field (Harbrecht et al. [2015], Pezzuto et al. [2019]). Similarly to Pezzuto et al. [2019], Algorithm 2 shows the procedure to generate a correlated random field.

Algorithm 2 Generation of a correlated random field.

1: The **initialization stage:** Define random field parameters:

$$\mu, COV, ACF, \theta_x, \theta_z.$$

2: **Correlation matrix generation:** Generate the correlation matrix (M) based on the FE mesh nodes and above parameters. If there are n nodes in a basin, $M \in R^{n \times n}$.

3: **Calculating eigenvalues and eigenvectors of M:** Calculate eigenpairs (λ_i, ϕ_i) of correlation matrix M, where λ_i is i-th eigenvalue and ϕ_i is the i-th eigenvector.

4: **Estimating correlated random field:** The correlated random field can be calculated as:

$$V_s(x) = \mu + \sigma \Sigma_{i=1}^{m} \sqrt{\lambda_i} Z_i \phi_i \tag{4.1}$$

where Z_i is an independent sample drawn from the standard normal distribution. m is estimated using the Cholesky decomposition.

The following subsections detail different components of correlated random field generation of Algorithm 2.

4.2.2.1 von Karman Autocorrelation Function

The correlation structure of a random field can be characterized using an ACF in the spatial domain or its power spectral density (PSD) in the Fourier domain (Mai and Beroza [2002]). In this study, we use von Karman (Ishimaru [1978]) ACF as shown in Eq. 4.2 (Mai and Beroza [2002]). von Karman ACF is an appropriate choice for solid Earth material (Savran and Olsen [2016]), and we use it as the main ACF in this chapter

$$C(r) = \frac{G_H(r)}{G_H(0)} \tag{4.2}$$

where $G_H(r) = r^H K_H(r)$. Here, H is the Hurst exponent (we assume $H = 0.1$), K_H is the modified Bessel function of the second kind (order H). r is called the characteristic length and is given as a function of horizontal and vertical correlation lengths $r = \sqrt{\frac{x^2}{\theta_x^2} + \frac{z^2}{\theta_z^2}}$.

Having set the ACF, the remaining four parameters will be discussed in the following subsection. We will also discuss the impact of ACF on SGM in § 4.3.4 by considering two other ACFs, namely Gaussian and exponential.

4.2.2.2 Statistical Parameters

Table 4.2 shows values for the parameters mentioned before. To generate the random medium, we use Gaussian distribution similar to Frankel and Clayton [1984]. We define the distribution using mean μ and coefficient of variation ($COV = \sigma/\mu$, is the standard deviation). The combination of values of Table 4.2 are used to study the effect of horizontal and vertical correlation lengths, and COV. $\mu = 250\,m/s$ (taken from background medium), $COV = 0.2,\ 0.3,\ 0.4$, $\theta_x = 50\,m$, 100, $200\,m$, and $\theta_z = 20\,m$, $40\,m$ are used. Moreover, based on the frequency content of input motion, the values of θ_x and θ_z provide an impact on the resultant surface response at different frequency ranges, as will be discussed later. These values result in 13 separate numerical models as shown in Table 4.2. The parameters are chosen to cover a reasonable range of values based on the geometry of the basin and introduce a sufficient variation in material properties in a basin. In the table, the first 5 models has $COV = 0.2$. Models 6 and 7 are added to better represent the impact of COV when moving from $COV = 0.2$ to $COV = 0.4$. The last 6 models have $COV = 0.4$.

4.2.2.3 Statistical Significance of Monte Carlo Simulation

An essential parameter in doing Monte Carlo simulation is the number of realizations to guarantee statistical significance. In this chapter, we measure statistical significance by

No.	Properties			
	μ (m/s)	COV	θ_x (m)	θ_z (m)
1	250	0.2	50	20
2			100	20
3			100	40
4			200	20
5			200	40
6		0.3	100	20
7			200	20
8		0.4	50	20
9			50	40
10			100	20
11			100	40
12			200	20
13			200	40

Table 4.2: Statistical parameters for different models of this study.

repeating the simulations until the convergence rate (CR, Eq. 4.3) is less than 5% for a specific intensity measure (IM) of interest. We examined PGA similar to El Habar et al. [2019]. PGA is chosen for model #3 for representation given that it has parameters that would provide the worst-case scenario.

$$CR = \frac{|IM_i - IM_{i+1}|}{IM_i} \tag{4.3}$$

where i is the realization number. Figure 4.3 shows the variation of the mean and standard deviation of PGA in percent in the middle of the basin of model #3 from Table 4.2. To assure the statistical significance of all models in our analysis, we use 50 realizations. Note that basin configuration is helping with the statistical significance. This is the reason why a higher realization number is necessary for non-basin geometries. For example, in El Habar et al. [2019], 100 realizations are used to satisfy the 5% criterion.

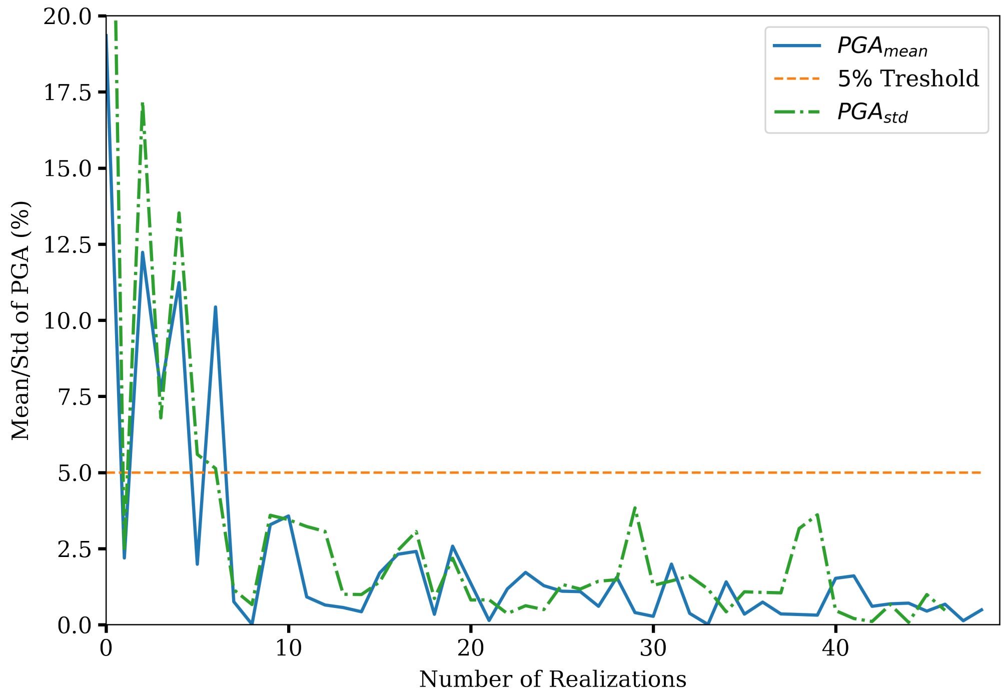

Figure 4.3: Convergence of the Monte Carlo simulation for mean and standard variation of PGA at the middle of #3 basin.

4.3 Results

In this section, we present the results of the numerical simulations. We elaborate on them by examining both time domain and frequency domain responses. We define the time domain amplification factor as PGA at each point of basin surface divided by the far-field PGA (it is 2 due to the doubling effect). In addition, seismogram synthetics of surface motion is also shown to represent the spatio-temporal variation of SGM better. On the other hand, the frequency domain amplification factor is defined as the amplitude of the Fourier transform of a time-series divided by the corresponding Fourier transform amplitude of rock outcrop. We also assess the impact of stochastic patches on Arias Intensity and the fundamental frequency of a basin. Comparisons are made by considering a point at the center of the basin ($p1$), see Figure 4.1). In the first subsection, we study one realization from each model #1, #2, #3 together with the background model. Note that *benchmark* is a stochastic case while the *background* is a homogeneous model. We use the benchmark model to observe how a stochastic model differs from the background model. Next, we examine different statistical parameters that shape a correlated random field (Table 4.2) by studying the ensemble of realizations both in time and frequency domains.

4.3.1 Benchmark

As the benchmark example, we use one realization from three models and compare the results with the background model. The models are $\theta_x = 100\,m$, $\theta_z = 20\,m$, $COV = 0.2$ (model #2), $\theta_x = 50\,m$, $\theta_z = 20\,m$, $COV = 0.2$ (model #1), and $\theta_x = 100\,m$, $\theta_z = 20\,m$, $COV = 0.4$ (model #3). These examples are used to portray the effect of a random medium on SGM and how it is different from the background model. We specifically focus on COV and θ_x here, and we leave θ_z and ACF for a later section. Each column of Figure 4.4 shows responses corresponding to the top-row velocity profiles (Figure 4.4-a). As can be seen, the left column shows the background model, the second from left is model #2, the second from the right is model #1, and the right column shows model #3. Note that these realizations are examples of possible correlated random fields, and the results do not speak for the ensemble of realizations. The background model is a homogeneous basin, and the value of shear wave velocity equals the values in Table 4.1. By comparing one realization versus the other two, one can see the effect of θ_x and COV in the random field generation. Increasing θ_x results in a stretched stochastic patches in a basin (comparison of model #1 and model #2) while increasing COV results in a more pronounced shear wave velocity variation in a basin (comparison of model #1 and model #3). These changes will directly impact the wave interference in a basin. For the comparison, we will consider point $P1$ of Figure 4.1.

Figure 4.4-b demonstrates horizontal and vertical time-series at $p1$. It turns out that the amplitude of horizontal and vertical acceleration is lower than the background model due to the scattering effect of heterogeneity patches. Given the horizontally polarized input motion, the accentuated vertical component is of importance for all the realizations. This will introduce a torsional motion in the basin which could impact long infrastructure components, such as pipelines. In addition, an elongation in time-series duration is observable, especially for model #3, which is in addition to the fact that even a homogeneous basin would increase the duration of oscillation on the surface compared to the rock outcrop. Therefore, adding the heterogeneities will exacerbate the situation. This phenomenon happens for both horizontal and vertical components.

Figure 4.4-c portrays the surface amplification in time-domain. As was defined before, it shows the division of PGA at each point on basin surface with respect to PGA of rock outcrop in x direction (which is twice the input PGA). This figure better quantifies the spatial variation of surface amplification. While the middle points show both lower (model #3) or higher (model #2) amplification with respect to the background model in the horizontal direction, the SGM is exacerbated due to the existence of a randomized medium as we

move toward basin edges. In addition, a significant amount of amplification occurs in the vertical direction in the basin center while the input motion is purely horizontal. These observations are a testament to the insufficiency of a homogeneous representation to fully take variation and magnitude of SGM into account, where the asymmetry and large variation of amplification with distance better resemble what is observed in Nature. Note that the computational cost is the main drawback of such an analysis in practice. In this study, since we are using 50 realizations, each model of Table 4.2 has 50 times more computational cost than the background model on average.

Lastly, Figure 4.4-d and Figure 4.4-e demonstrate the surface seismogram synthetic in horizontal and vertical directions, respectively. A relatively noticeable difference between randomized and background models is the "activation" of more local interactions and accentuated reverberation. As can be seen, more intense oscillations happen on the basin surface in the stochastic case, which is due to the fine-scale stochastic features. This could have a significant impact on structures and infrastructure components that would not be affected by the low-frequency component of the seismic wave.

Figure 4.5 demonstrates the difference between each realization by focusing on their relative behavior with respect to the rock outcrop in the frequency domain. This figure portrays the Fourier spectral amplification. The Fourier spectral amplification is defined as the division of the Fourier transform of a time-series in a specific location ($p1$ in this case) with respect to the corresponding Fourier transform on the rock outcrop. In this figure, each column shows the results of the corresponding realization at the top, including the background model, similar to Figure 4.4. In Figure 4.5-b, the general trend of amplification is similar between background model and realizations, which demonstrates the impact of basin geometry on the surface response. As was seen in Figure 4.4, it also depends on the location at which the results are being plotted, and the response varies as one moves along the basin. Stochastic patches also impact a basin's fundamental frequency, which will be explained in a later section. Finally, Figure 4.5-c shows a response similar to Figure 4.4-d except here Fourier spectral amplification is portrayed. The symmetry in the background model no longer exists in stochastic cases. A more considerable amplification at basin edge exists for stochastic cases, which does not exist in the background model. This is a confirmation of the previous observations of Figure 4.4-c, in which a significant amplification happened at basin corners.

In the following subsections, we examine the impact of statistical parameters on SGM. COV is studied in § 4.3.2, Correlation lengths (θ_x and θ_z) in § 4.3.3, and ACF in § 4.3.4. The following figures are being discussed in later sections: 1) mean and standard deviation of Fourier spectral amplification with respect to the rock outcrop; 2) similar to Fourier spectral

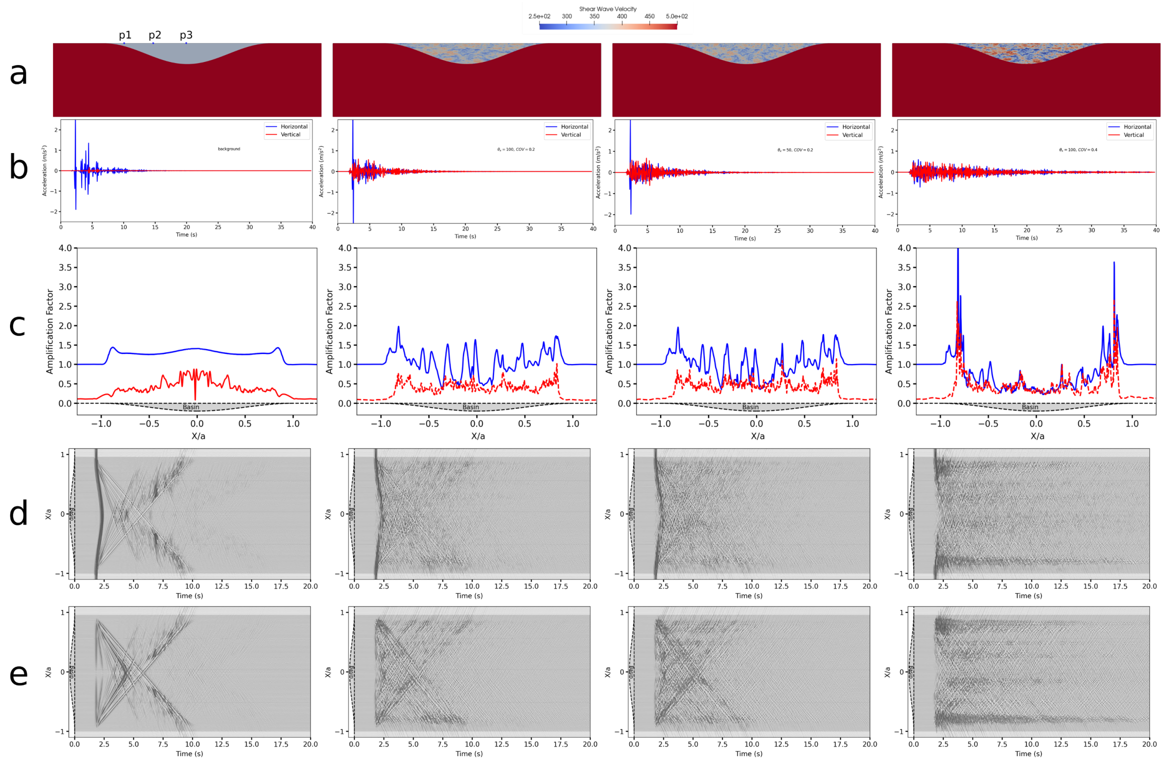

Figure 4.4: Comparison between homogeneous and stochastic models: a) Background model and one realization of model #2 **(**$\theta_x = 100\,m$**,** $\theta_z = 20\,m$**,** $COV = 0.2$**), model** #1 **(**$\theta_x = 50\,m$**,** $\theta_z = 20\,m$**,** $COV = 0.2$**), model** #3 **(**$\theta_x = 100\,m$**,** $\theta_z = 20\,m$**,** $COV = 0.4$**), b) acceleration time-series at point** $p1$**, c) surface amplification in horizontal and vertical directions, d) seismogram synthetic for surface acceleration in horizontal direction, e) seismogram synthetic for surface acceleration in vertical direction.**

amplification, response spectra amplification and its standard deviation will be discussed; 3) significance duration ratio is computed with respect to the background medium. Significance duration is defined as the duration between 5% and 95% of final Arias Intensity; 4) fundamental frequency ratio is computed by dividing the fundamental frequency of the stochastic model with respect to the background medium.

4.3.2 Effect of Coefficient of Variation

COV affects the range of velocity variation by defining the standard deviation in the random field as shown in Algorithm 2. By increasing COV, the random field would take a wider range about the mean. This introduces larger shear wave velocity contrasts within a basin, which results in more scattering. For example, given the mean shear wave velocity of $250\,{}^{m}/_{s}$ (see Table 4.1), $COV = 0.2$ results in standard deviation of $50\,{}^{m}/_{s}$ while $COV = 0.4$ introduces a standard deviation of $100\,{}^{m}/_{s}$. Such a difference would significantly impact the shear wave velocity values in a basin and basin response under seismic loading.

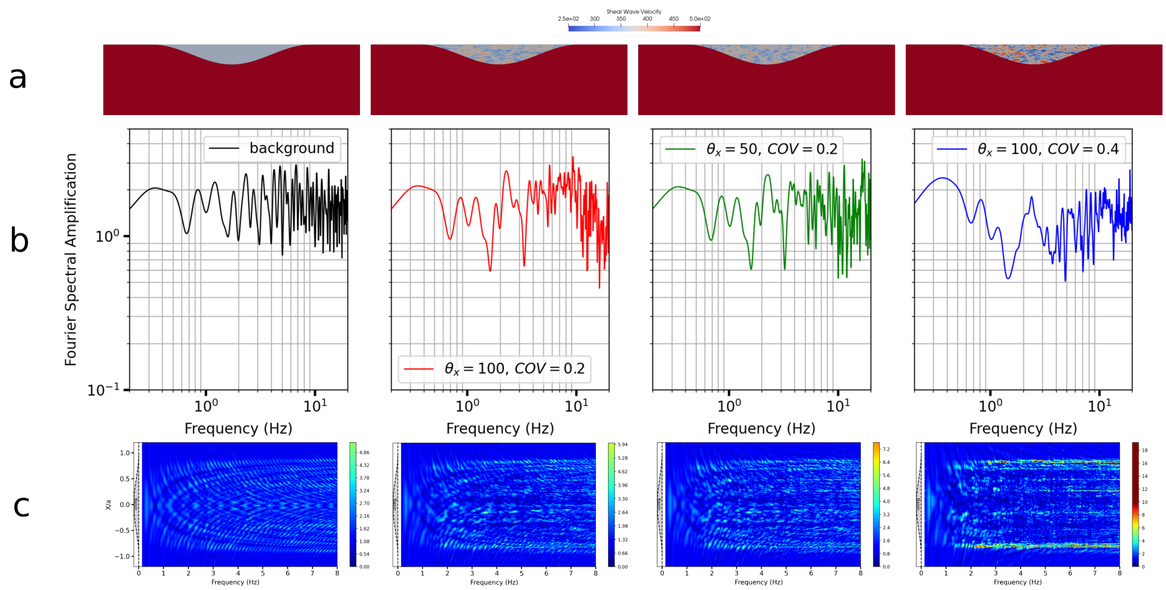

Figure 4.5: Similar to Figure 4.4: a) realizations, b) Fourier spectral amplification with respect to rock outcrop, and c) equivalent of seismogram synthetics of Figure 4.4-d except that it shows Fourier amplification at different frequencies. The colorbar is capped at 10.

Figures 4.6 and 4.7 show the Fourier spectral amplification and standard deviation. Figure 4.6 is divided into two sub-figures, one covering the frequency range of 0.1 Hz to 0.8 Hz and the other 0.8 Hz to 10 Hz. In these figures, we focus on three models in addition to the background. For most of the analysis of this study, model #2 is the benchmark, and for each statistical parameter, the impact is investigated by changing values with respect to this model. By holding θ_x and θ_z fixed, and changing COV, in Figure 4.6-a, one can see that the fundamental frequency of basin moves toward lower frequency as we increase COV. This can be attributed to the higher variation of shear wave velocity in the basin, resulting in an accentuated lateral propagation of the seismic wave. The changes in the fundamental frequency will be better quantified in Figure 4.9. Lower COV value results in a medium that is more similar to the background model, which is the reason that responses of models with $COV = 0.2$ better resembles the background medium than $COV = 0.3, 0.4$. In Figure 4.6-b, the background medium shows more oscillatory amplification in comparison to the mean of stochastic models. However, the advantage of a stochastic simulation is to provide a range in which the amplification value could happen, i.e., considering the standard deviation is an essential part of the analysis. Given that the shear wave velocity values are generated using Gaussian distribution, $\pm 2\sigma$ (σ is the standard deviation.; we limit velocity values to be within $\pm 2\sigma$ of μ.) of mean is probable to happen for each model. This could result in a higher amplification than the background model.

Figure 4.7 shows the standard deviation of Fourier spectral amplification. Regardless of the

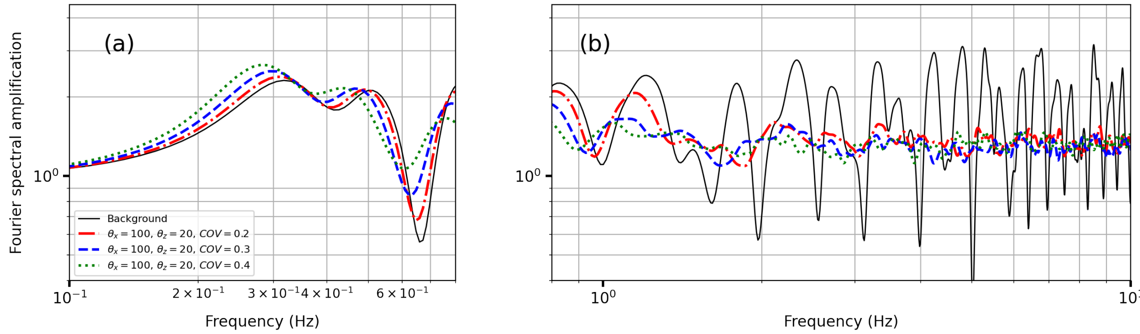

Figure 4.6: Mean Fourier spectral amplification at point $p1$ for three models with $\theta_x = 100\ [m], \theta_z = 20\ [m]$ and different COVs. Background model is shown in black. Fourier spectral amplification is defined as the ratio of Fourier transform of acceleration time-series at point $p1$ with respect to the rock outcrop. a) frequency range of $0.1\ [Hz]$ to $0.8\ [Hz]$, b) frequency range of $0.8\ [Hz]$ to $10.0\ [Hz]$.

frequency range, models with higher COV have a higher standard deviation in frequencies less than 2 $[Hz]$. This is due to the enhanced shear wave velocity variation inside the basin. By moving toward higher frequencies, the impact of the range of shear wave velocity values becomes less pronounced as in higher frequencies; all the heterogeneities would interact with the seismic wave inside the basin, which will produce a high enough standard deviation for surface amplification.

Figure 4.8-a is similar to Figure 4.6 except that it shows the mean response spectra amplification and its standard deviation. Response spectra amplification shows a cleaner representation of low-period (high-frequency). As can be seen, by adding stochasticity to the basin, the amplification decreases. Higher values of COV will result in a de-amplification. Figure 4.8-b shows the standard deviation of response spectra amplification, and similar to Figure 4.7, it shows that a more considerable value of COV would result in a higher standard deviation.

To further quantify the impact of COV on significance duration and fundamental frequency of basin, Figure 4.9 demonstrates the two outputs as a ratio with respect to the background medium. The circles show the mean in this figure, and bars demonstrate 1 standard deviation from the mean. Figure 4.9-a shows the significant duration ratio. As previously mentioned, significance duration is defined as the time between 5% to 95% (T_{5-95}) of Arias Intensity final value. As can be seen, increasing COV results in a higher mean and standard deviation, which can be explained by enhanced scattering of seismic waves for larger COV. $COV = 0.2$ shows almost $1.5 - 2$ increase and $COV = 0.4$ has values as high as $5 - 6$ times the background model. $COV = 0.4$ shows a strong reverberating effect due to heterogeneities which significantly elongate the shaking duration. Figure 4.9-b, on the

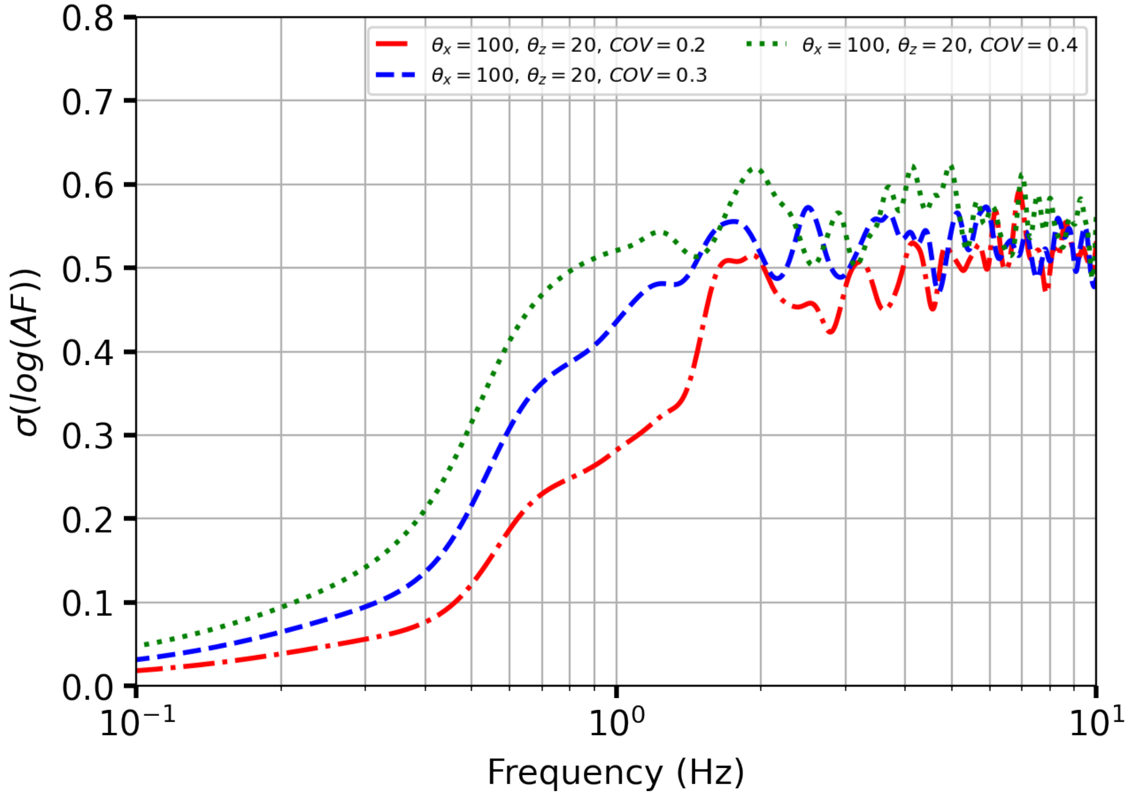

Figure 4.7: Standard deviation of natural logarithm of Fourier spectral amplification of models in Figure 4.6.

other hand, demonstrates the fundamental frequency (f_0) ratio. Increasing COV results in a lower f_0, as was mentioned before. The trend of the mean ratio seems to be almost linear as a function of COV and does not change due to correlation lengths. Note that although the mean f_0 ratio decreases as COV goes up, the standard deviation of the ratio increases. This figure shows that the fundamental frequency can go as low as 0.9 times the background medium.

4.3.3 Effect of Correlation Length

The next component of a correlated random field that we will examine is the correlation lengths in horizontal (θ_x) and vertical (θ_z) directions. As was shown previously, we consider different values for each direction, namely $\theta_x = 50$, 100, 200 m and $\theta_z = 20$, 40 m. The values are chosen based on two criteria: 1) the size of patches is large enough to be "seen" by the seismic wave, and 2) we have enough patches in the basin in each direction. The second criterion is to ensure enough interaction between the seismic waves and heterogeneities. θ_x and θ_z show the distance from a point above which two points are not correlated. Changing the size of patches affects the interaction of seismic waves (patches behave as

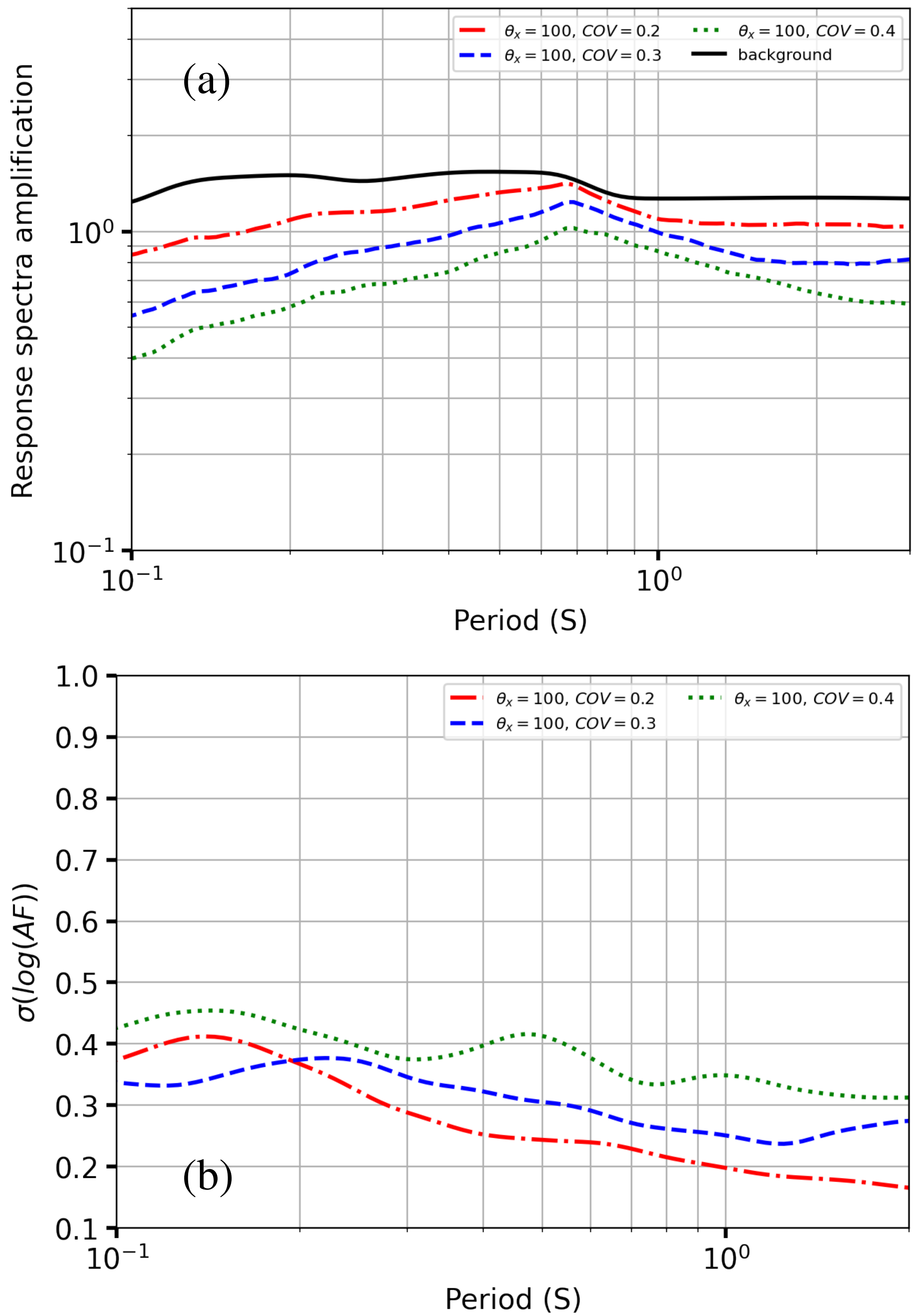

Figure 4.8: Response spectra amplification for point $p1$ for three models with $\theta_x = 100\ [m], \theta_z = 20\ [m]$ and different COVs: a) Mean and b) standard deviation.

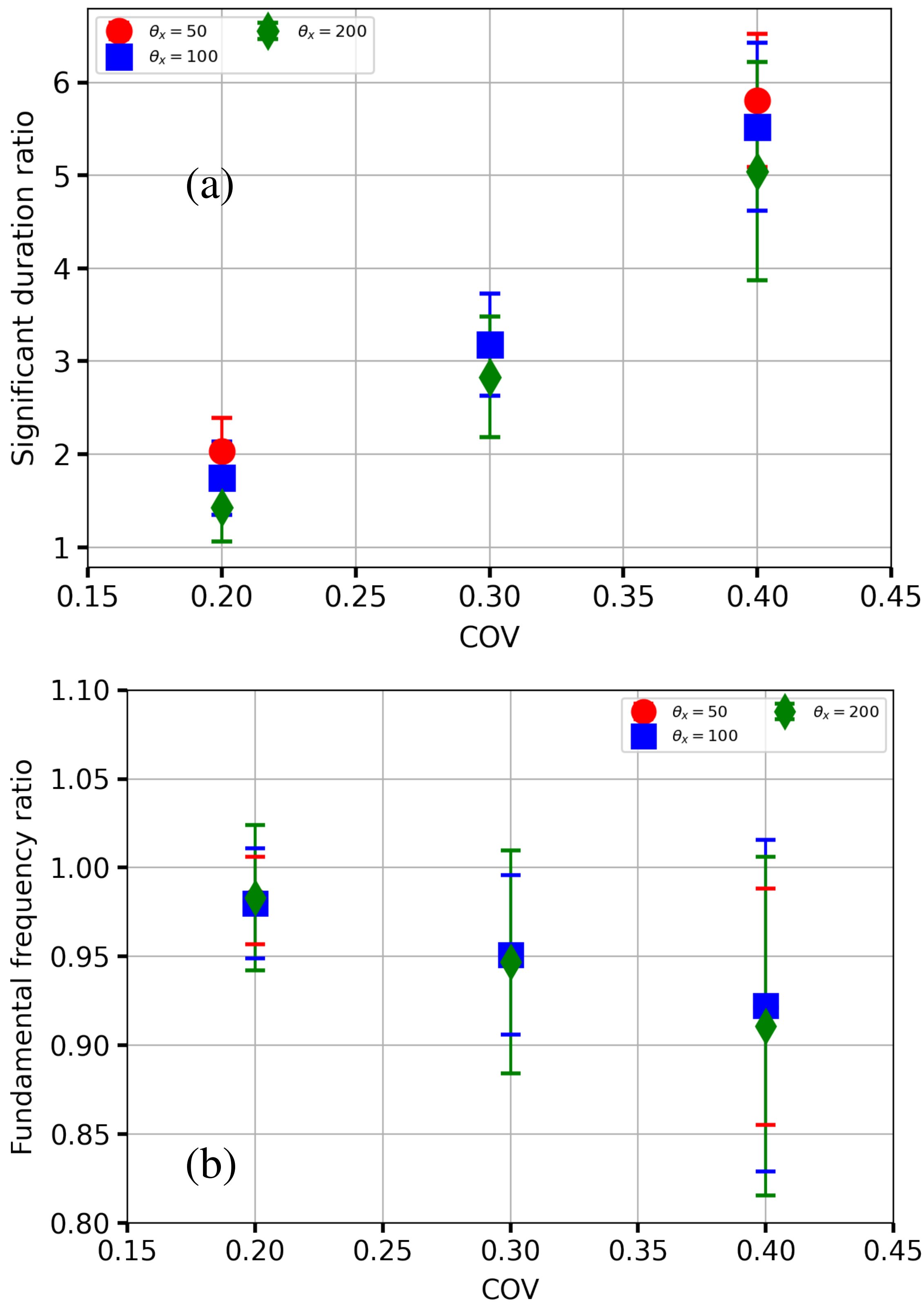

Figure 4.9: Time and frequency domain response for ensemble of realizations for 8 models of Table 4.2 with $\theta_z = 20\,[m]$. Results are shown for $p1$. Circle symbols shows $\theta_x = 50\,[m]$, square shows $\theta_x = 100\,[m]$, and diamond shows $\theta_x = 200\,[m]$. a) significance duration ratio, b) fundamental frequency ratio.

points of scattering) and cause a reflection and refraction of waves within a basin. This might eventually affect the observed SGM. Increasing the size of patches could push the wave-patch interaction toward a larger wavelength (or lower frequency).

Assuming an average of 250 m/s for shear wave velocity and a maximum frequency of 12 Hz, the minimum wavelength is $\sim 21\,m$. By decreasing the frequency, the wavelength increases, and different interaction scales are expected depending on the size of heterogeneities. For the horizontal component, the interference between seismic waves and stochastic patches happens due to mode conversion at the basin corner or the decomposition of the incoming shear wave when entering the basin, dependent on basin-edge effect and shear wave velocity contrast. In general, increasing patch size shows the impact on surface acceleration at a lower frequency, especially in terms of standard deviation, as will be shown later.

In deciding the importance of correlation lengths, focusing on a frequency range is necessary. The seed for random number generation is set to guarantee the reproducibility of a correlated random field for all the models shown here. This means that for a fixed COV, for a certain realization, models with different θ_x will have similar material representation except for a stretch or shrink of patches based on the magnitude of θ_x. Similar behavior is expected for vertical correlation. Therefore, a patch with $\theta_x = 200\,m$ would interact with lower frequency components than a patch with $\theta_x = 100\,m$.

Figure 4.10 shows two sets of comparison. Figures 4.10-a and b show the mean amplification of four models. These figures are supposed to show the impact of θ_z on surface amplification. We fix $\theta_x = 100\,[m]$ for this figures to assess how θ_z would change the mean amplification. We do not fix COV to investigate whether the impact of θ_z changes with COV. The role of θ_z can be explained by considering the overall configuration of the model. As for the first arrival of the SV plane wave, the horizontal component of motion shown here is impacted by θ_z since the wave is horizontally polarized but vertically propagated. However, the influence is not noticeable for lower COV. It becomes more pronounced for larger COV as a separation between curves for $\theta_z = 20\,[m], COV = 0.4$ and $\theta_z = 40\,[m], COV = 0.4$. As for the θ_x, Figures 4.10-c and d portray a similar pattern as Figures 4.10-a and b. Note that in this figure, we use $COV = 0.4$. The influence of θ_x on surface amplification is through affecting surface generated waves and decomposed body waves inside the basin due to the interference among heterogeneities. These figures show that the level of impact of θ_x is not as much as to produce a meaningful difference between different models in terms of mean amplification.

To further study correlations lengths, Figure 4.11 shows the standard deviation of amplification at point $p1$ for vertical and horizontal correlation lengths. The influence of

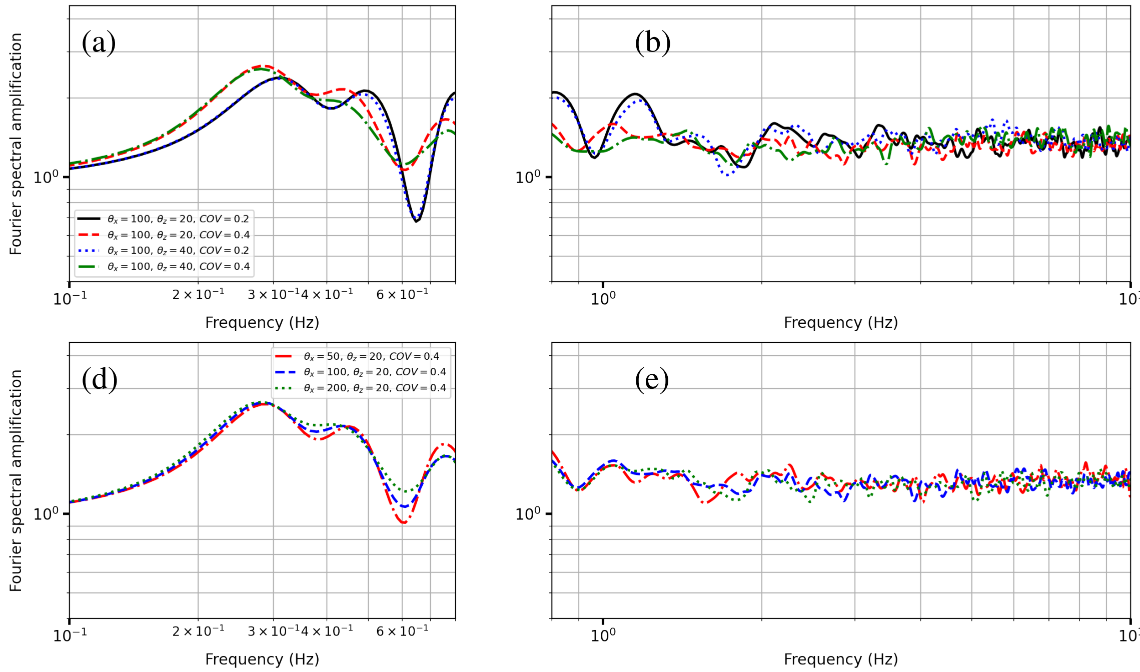

Figure 4.10: Four models with fixed $\theta_x = 100\,[m]$, $\theta_z = 20, 40\,[m]$, and $COV = 0.2, 0.4$: a,b) mean Fourier spectral amplification to study the impact of θ_z. Three models with fixes $\theta_x = 20\,[m]$ and $COV = 0.4$, and three values of $\theta_x = 50, 100, 200\,[m]$: c, d) Fourier spectral amplification to study the impact of θ_x.

correlation lengths can be better seen in standard deviation plots. For θ_z, Figure 4.11-a shows two groups of graphs, which COV separates. As was previously mentioned, COV is the dominant parameter in the correlated random field. For θ_x, in Figure 4.11-b, model with $\theta_x = 200\,m$ has a higher standard deviation than the model with $\theta_x = 100\,m$ (fixed COV) at lower frequencies. However, the difference narrows as we move toward higher frequencies. Note that in the comparisons shown here, since the values are chosen realistically, and are relatively close to each other, the distinction may not be as significant as one would expect. The difference would have been easier to distinguish if we had for instance $\theta_x = 200\,m$ and $\theta_x = 20\,m$. The observations about correlation lengths were also observed in other studies such as El Habar et al. [2019] for a rectangular domain.

As the final illustration to confirm our previous observation about the impact of correlation length on SGM, Figure 4.12 shows significance duration ratio and fundamental frequency ratio as a function of θ_x. Three difference COVs are shown with different symbols. The horizontal axis shows θ_x, and the vertical axis indicates an output of interest. As can be seen, for both significance duration ratio and fundamental frequency ratio, changing θ_x does not significantly impact the outcome, which confirms our earlier findings.

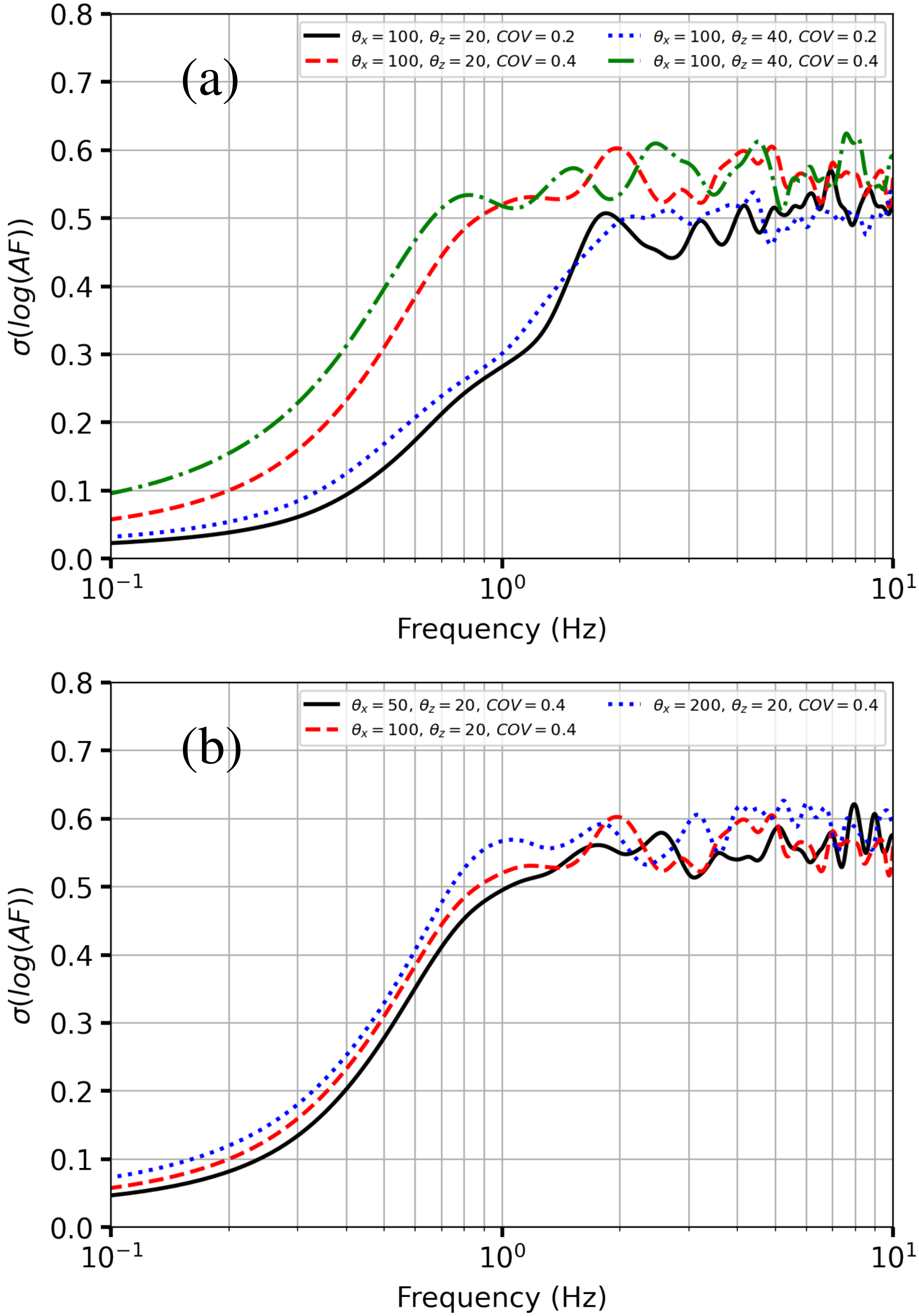

Figure 4.11: Standard deviation of natural logarithm of amplification for a) models with $\theta_x = 100,\ \theta_z = 20, COV = 0.2$**,** $\theta_x = 100\,\theta_z = 20, COV = 0.4$**,** $\theta_x = 100,\ \theta_z = 40, COV = 0.2$**, and** $\theta_x = 100,\ \theta_z = 40, COV = 0.4$**, and b)** $\theta_x = 50,\ \theta_z = 20, COV = 0.4$**,** $\theta_x = 100,\ \theta_z = 20, COV = 0.4$**, and** $\theta_x = 200,\ \theta_z = 20, COV = 0.4$**.**

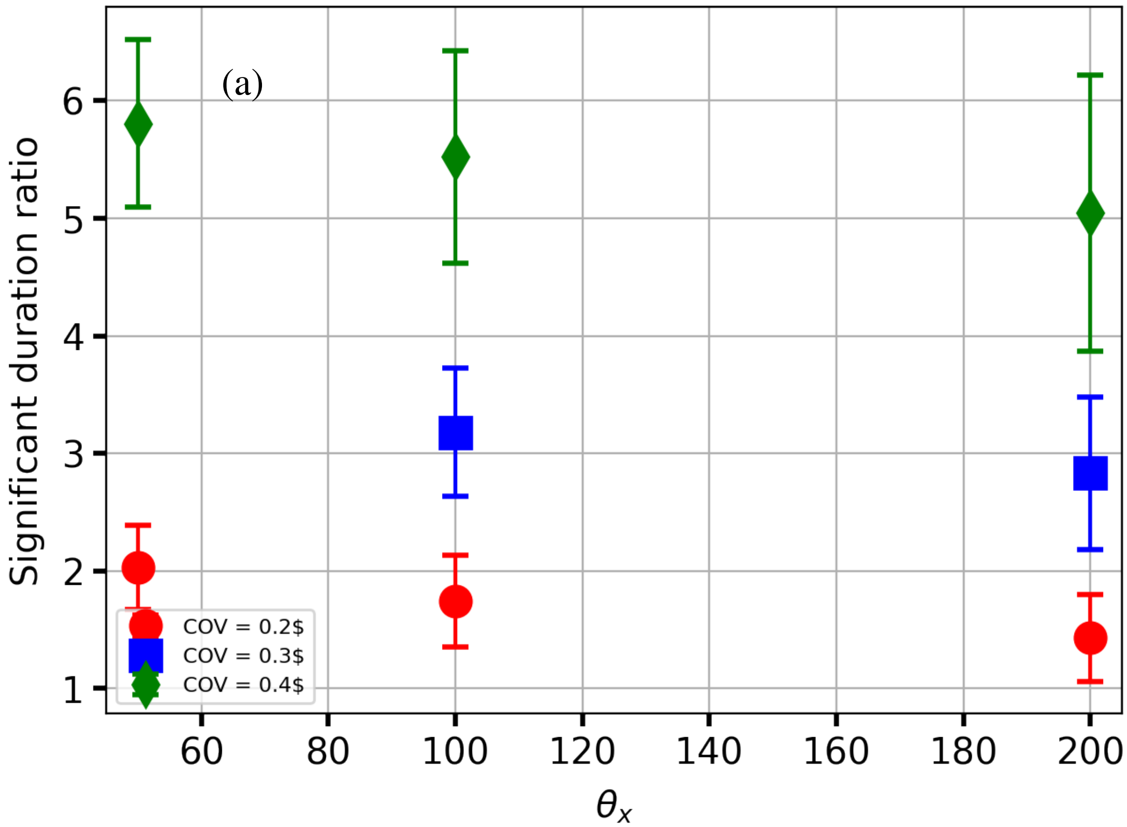

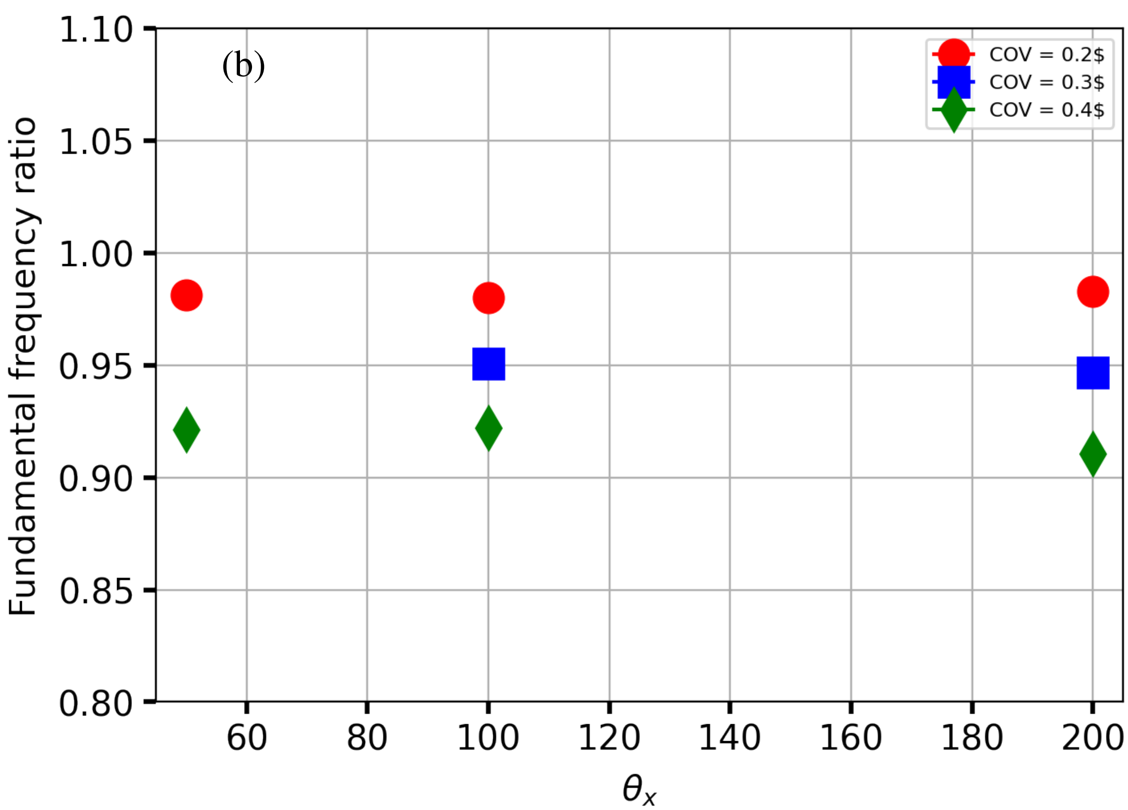

Figure 4.12: Time and frequency domain response for ensemble of realizations of 8 models of Table 4.2 with $\theta_x = 20\,[m]$ with respect to the background medium. The circle symbol shows $COV = 0.2$, the square symbol shows $COV = 0.3$, and diamond symbol shows $COV = 0.4$. Each point shows the mean of a model. a) significance duration ratio, b) fundamental frequency ratio. The difference from Figure 4.9 is that the horizontal axis is θ_x.

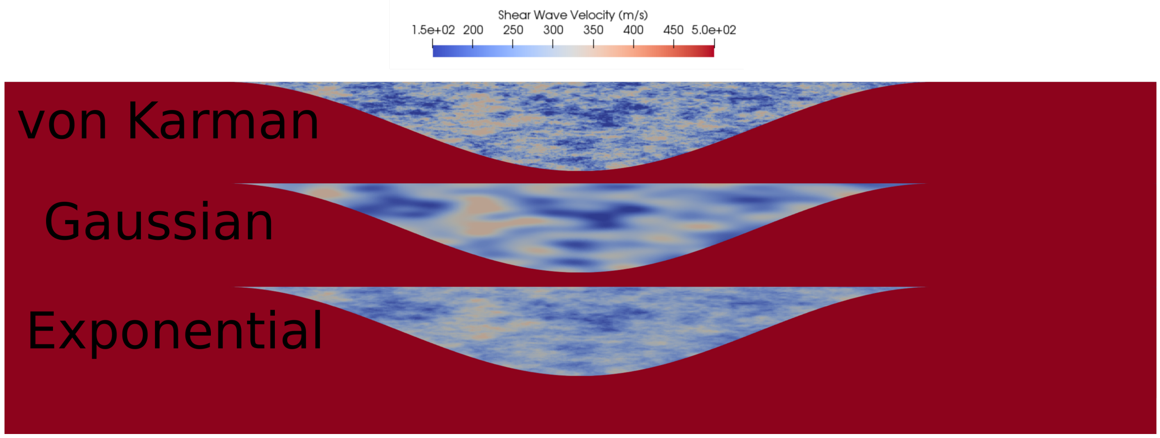

Figure 4.13: Example realizations with different ACF.

4.3.4 Effect of Autocorrelation Function

Up to now, we have used Von-Karman ACF to generate a correlated random field. There are other common autocorrelation functions that have been used in the literature, namely Gaussian (Eq. 4.4) and exponential (Eq. 4.5).

$$C(r) = e^{-r^2} \tag{4.4}$$

$$C(r) = e^{-r} \tag{4.5}$$

In this section, we examine the difference in basin surface response given different ACFs. For this comparison, we use model #2 from Table 4.2 and generate realizations based on different ACFs. Figure 4.13 shows three example realizations. Gaussian has the smoothest variation of shear wave velocity over stochastic patches as was shown repeatedly before, for example, in Frankel and Clayton [1984]. Since the seed numbers for the generation of random numbers are fixed, the general shape of heterogeneity patches is similar. The differences arise as to how fast/slow the correlation decays over distance.

Figure 4.14 shows the comparison results. As can be seen, the trend of amplification does not change for different ACFs. In Figure 4.14-a, the mean Fourier spectral amplification curves follow a similar path for all frequency ranges with a minimal difference between the models. For large frequencies, exponential ACF has a higher amplification over a wide frequency range.

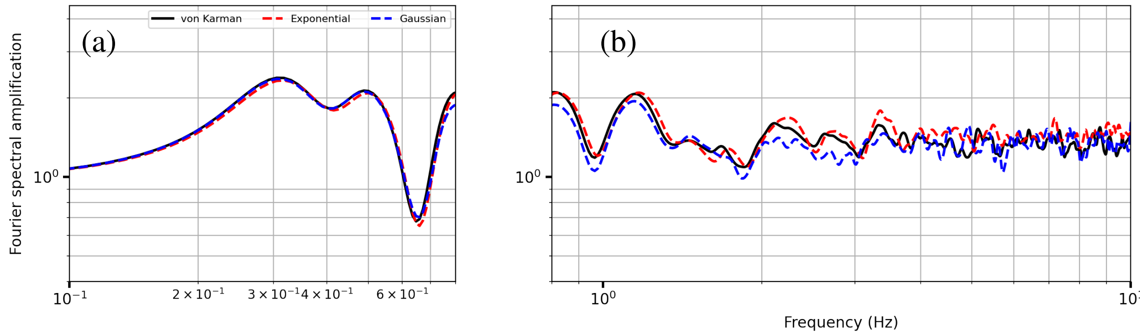

Figure 4.14: Geometric mean of Fourier spectral amplification at point $p1$ for different frequency range with different ACFs.

Figure 4.15 shows the standard deviation of the natural logarithm of amplifications. Gaussian has a higher standard deviation value in comparison to others in low frequency. This is due to the smooth drop of Gaussian ACF (Eq. 4.4), which constructs a larger chunk of heterogeneity. More interaction with seismic waves could result in a more significant reflection/refraction in the basin, increasing fluctuating behavior and standard deviation on the surface. As for higher frequency, there is no clear ACF that dominates the other two. We conclude that in the scenario studied in this chapter, ACF is not an influential parameter on surface response.

4.4 Comparison Between 1D and 2D Analysis

In this section, we assess how the analysis we have discussed in this chapter would compare with the state-of-practice. In practice, $1D$ wave propagation is the common approach for seismic hazard quantification. We intend to examine whether a $1D$ wave analysis is able to account for the response of a $2D$ heterogeneous basin. We choose three stochastic models, namely $\theta_x = 100\,[m]$, $\theta_z = 20\,[m], COV = 0.2$, $\theta_x = 100\,[m]$, $\theta_z = 40\,[m], COV = 0.2$, $\theta_x = 100\,[m]$, $\theta_z = 20\,[m], COV = 0.4$, and extract $1D$ shear wave velocity profile underneath point $p1$ for each realization. We simulate each column subjected to the same input as $2D$ models and compare the responses in terms of 1) mean Fourier spectral amplification and standard deviation and 2) mean response spectra amplification and standard deviation. Note that $p1$ has the closest condition to a $1D$ soil column since it is the farthest from the corners. As one moves toward a basin's edge, the corner effects would introduce a significant $2D$ wave interference to the surface ground motion.

Figure 4.16 shows the Fourier spectral amplification mean and standard deviation. The amplification is defined as the Fourier transform of basin response divided by surface response of $1D$ column. As can be seen in Figure 4.16-a, we observe a different surface

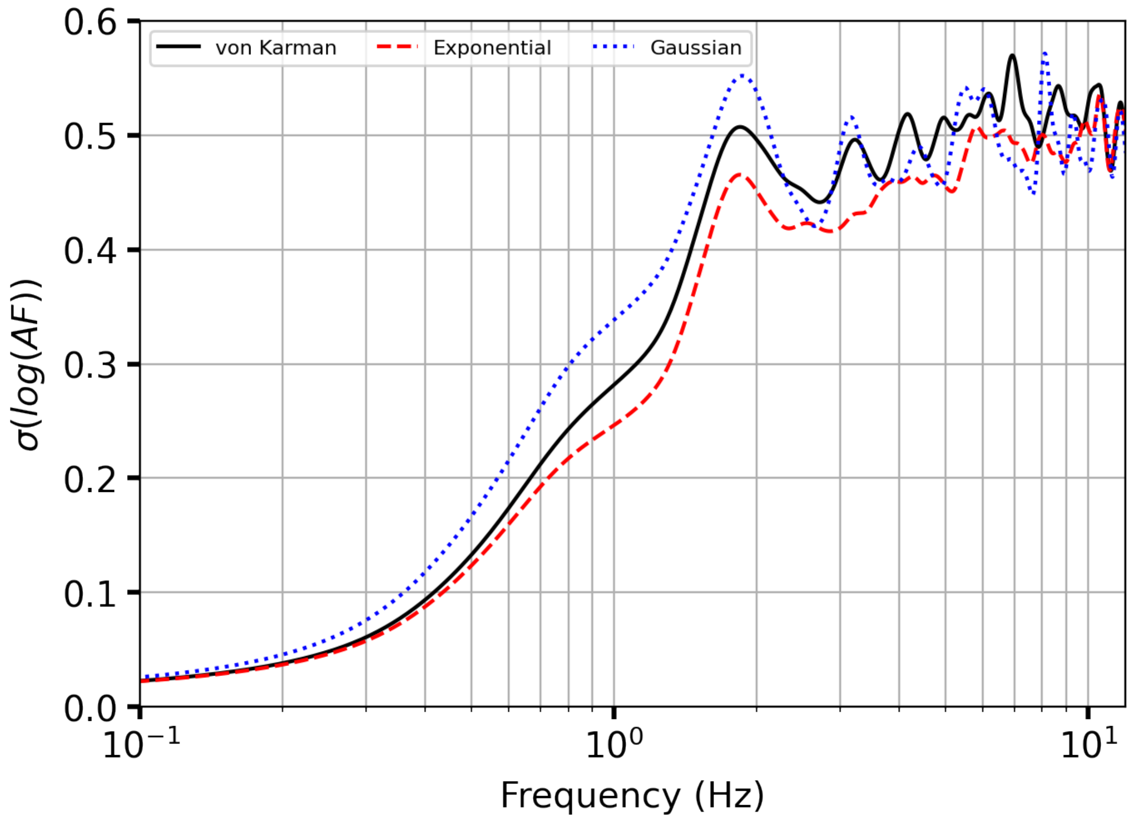

Figure 4.15: Standard deviation of natural logarithm of Fourier spectral amplification at point $p1$ with different ACFs.

response in comparison to the $1D$ analysis. In the $1D$ analysis, a layered soil medium is assumed while the $2D$ effects are neglected. Therefore, we expect significantly different resultant wavefields on basin surfaces both in low and high frequencies. The response in the low-frequency regime comes mostly from the $2D$ effects of the basin. On the other hand, heterogeneities would play an important role in the difference between responses of a $2D$ model and $1D$ layered medium for the high-frequency range. In this figure, the $COV = 0.2$ shows both amplification and de-amplification in low-frequencies (≤ 0.6 $[Hz]$). This observation is due to the fundamental behavior of $1D$ columns and basins. Similar behavior is observed for $COV = 0.4$. Note the shift toward lower frequency for higher COV as was mentioned before. As the frequency increases, the impact of heterogeneities accentuates. For $COV = 0.2$, the resultant amplification although not zero, is not significant since the $2D$ basins resemble background medium for this COV. We observe that both models show a consistent amplification over all frequencies above 1 $[Hz]$. However, for the model with $COV = 0.4$, the difference is significant compared to the $1D$ analysis, and we observe a significant amplification. Figure 4.16-b portrays the difference from the lens of standard deviation. While the model with higher COV shows a clear divergence from $1D$, the other two models still demonstrate a noticeable standard deviation. This means that $1D$ analysis is not appropriate for estimating a heterogeneous basin response even for lower COVs.

Response spectra mean amplification and the standard deviation is another way to investigate the capability of a $1D$ analysis to capture the $2D$ response of a basin with heterogeneities. The amplification is defined similarly to the Fourier spectral amplification of Figure 4.16. Figure 4.17 shows how the mean response spectra and standard deviation vary for different periods. As for response spectra amplification, the $COV = 0.4$ shows the maximum amplification in low period (equivalent to high frequency) and it decreases as we go to $COV = 0.2$. This is in agreement with Figure 4.16, and it can be seen that $1D$ analysis is not able to account for $2D$ effects inside a basin properly.

4.5 Summary and Conclusions

In this chapter, we investigated the effect of material heterogeneity on basin surface acceleration during an earthquake. By means of Monte Carlo simulation, we generate various realizations of a elastic basin velocity field and examined effects of coefficient of variation (COV, § 4.3.2), correlation lengths (θ_x and θ_z, § 4.3.3), and autocorrelation function (ACF, § 4.3.4) on the spatial variation of surface ground motion. Since the focus of this study is on the material heterogeneity effects, we do not consider different basin geometries and an idealized cosine shape with $AR = 4$ and $\beta_2/\beta_1 = 2$ are assumed for numerical analysis (Figure 4.1, derived from Chapter 2). The model is subjected to a vertically propagating SV plane wave of Ricker type with a dominant frequency of $5\,Hz$. We assume $\theta_x = 50$, 100, $200\,m$ and vertical $\theta_z = 20$, $40\,m$, $COV = 0.2$, 0.3, 0.4, and three ACFs, namely Von Karman, Gaussian, and exponential. For each parameter, we study its effect on surface ground motion in both time and frequency domains using 1) Fourier spectral amplification, 2) response spectra amplification, 3) significance duration ratio, and 4) fundamental frequency ratio. The following conclusions have been drawn through analyzing the results.

- COV defines the range of shear wave velocity in a medium with respect to a mean, and increasing COV results in a more considerable material contrast within a basin. This parameter affects the interference pattern of seismic waves and surface acceleration significantly. Our analysis shows that COV is the most influential parameter (among the three we examined in this chapter) on surface ground acceleration. By

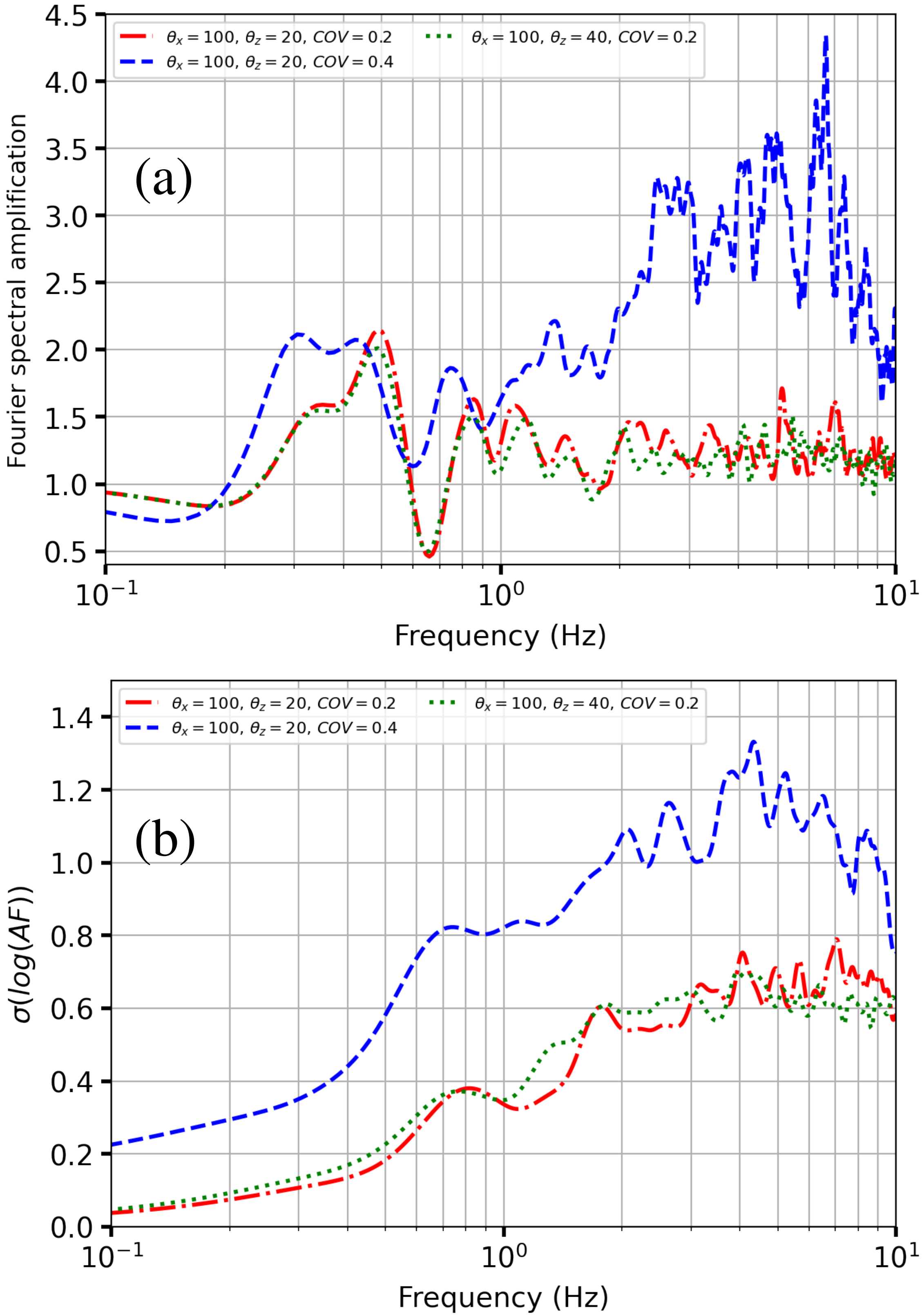

Figure 4.16: Fourier spectral amplification: a) Mean and b) standard deviation. Fourier spectral amplification is defined as the ratio between Fourier transform of time-series at point $p1$ of $2D$ model versus $1D$ analysis of a column underneath $p1$.

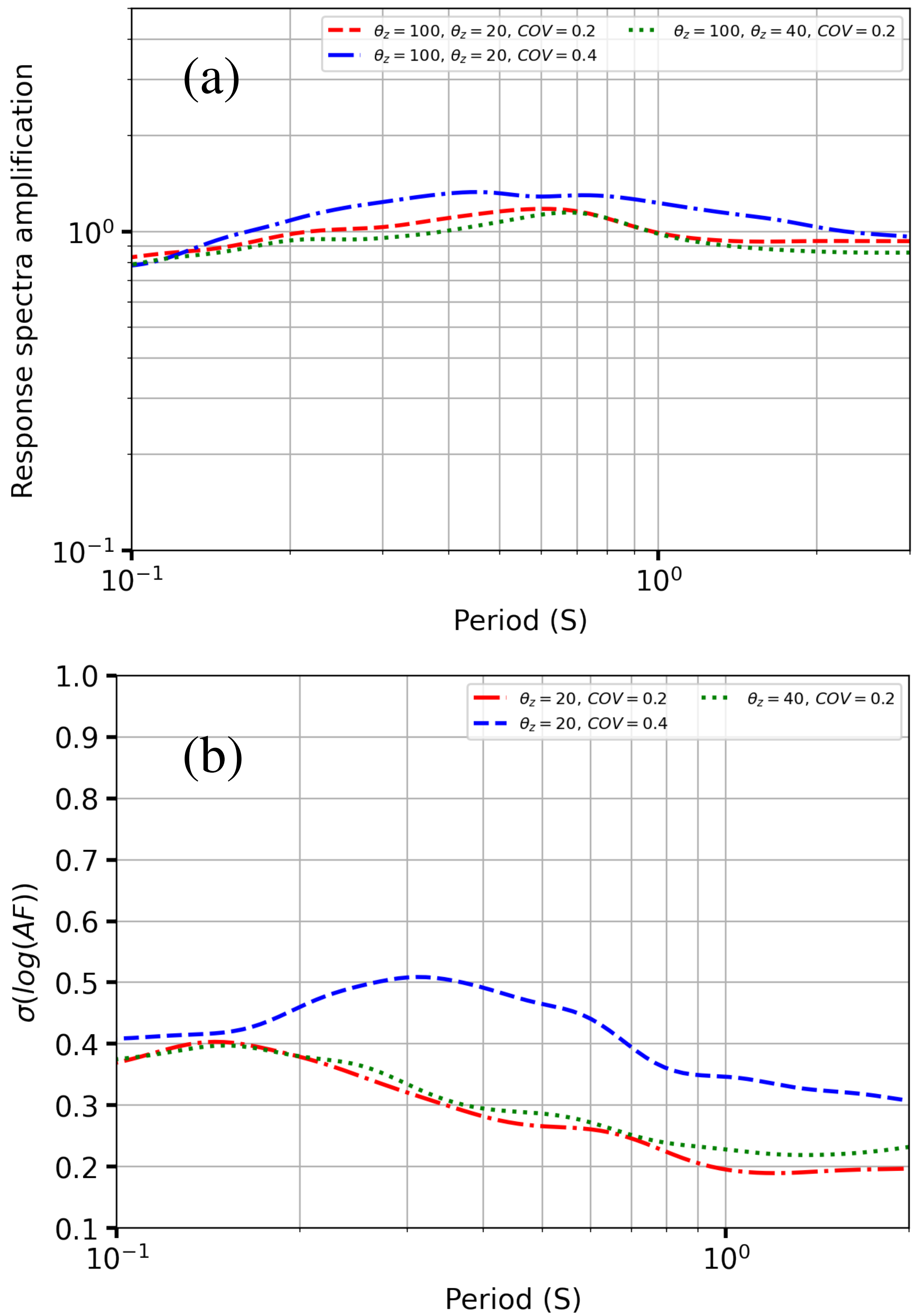

Figure 4.17: Response spectra amplification: a) Mean and b) standard deviation. Response spectra amplification is defined as the ratio between response spectra of time-series at point $p1$ of $2D$ model versus $1D$ analysis of the column underneath $p1$.

increasing COV, we observed elongation in significance duration and a decrease in the fundamental frequency of the basin. In addition, a significant increase in the standard deviation of surface amplification is observed.

- Correlation length (θ_x and θ_z) is another parameter of interest, which changes the size of heterogeneity patches in a medium that could affect wave-patch interaction. We observed that correlation lengths are not as important a factor as COV on surface response. Given that the input motion is a vertically propagating horizontally polarized wave, the size of θ_z affects the vertically propagating wave while contributing toward the horizontal component of surface motion. θ_x works differently by affecting horizontally propagating waves and contributing to the vertical component of motion as SV waves propagate in the basin. Different mechanisms could happen for Rayleigh and P-waves in the basin due to mode conversion and edge-induced surface waves. In sum, the impact of correlation lengths is not significant, but it changes the standard deviation of surface amplification in different frequency ranges depending on the size of heterogeneities.

- The autocorrelation function (ACF) is the last parameter we studied in this chapter. While von Karman ACF is an appropriate choice for studying solid Earth, we have also examined two other common ACFs: Gaussian and exponential. We observed that although there are slight differences between the mean and standard deviation of resultant surface response for different ACFs, the discrepancies are insignificant.

- Finally, we compared the results of heterogeneous basins versus the $1D$ site analysis, which is the standard approach in practice. We extracted all $1D$ columns underneath point $p1$ from all realizations of 3 models. We performed a series of $1D$ analyses to examine how close the response of a $1D$ column would be to the $2D$ basins. Using amplification mean and standard deviation, we showed that $1D$ could not fully account for the $2D$ phenomena in a basin with heterogeneities.

Chapter 5

Conclusions

Contents of this chapter

5.1 Summary of Previous Chapters

This thesis presents the author's research on basin effects parameterization and modeling in $2D$. While the practice still relies on $1D$ site response analysis which is not able to properly capture basin-edge effects, this research contributes toward better incorporation of basin effects in GMPEs and design codes. It also presents a path to reduce computational cost and better representation of basin material in $2D$ simulations.

Chapter 2 presents results of a comprehensive parametric study through which, we were able to prioritize important dimensionless parameters for basin seismic hazard quantification. We concluded that three dimensionless parameters, namely aspect ratio (AR), shear wave velocity contrast (β_2/β_1), and dimensionless frequency (η) are the most influential parameters on a SE- or HC-shaped basin response. We also showed that in the scenarios studied in Chapter 2, damping, materials Poison's ratio, and density are of secondary importance on surface response. We chose HC-shaped to be a more realistic and appropriate due to gradual increase of depth from basin edges. We finally tried to replicate strong ground motion recordings of Kathmandu basin, Nepal during the 2015 M_w 7.8 Gorkha earthquake and showed that a simplified model is able to capture notable characteristics of basin response in low-frequency range.

Chapter 3 presents results of a new approach to estimate acceleration time-series in a basin. Based on our findings in Chapter 2, we utilize three parameters, namely aspect ratio, velocity contrast, and dimensionless frequency, together with a dimensionless location to train a neural network in order to return the acceleration time-series at location $\hat{x}$ in a model with aspect ratio AR and shear wave velocity contrast C. We generate a set of synthetic data using FEM simulations for training and train two models to learn amplitude and phase of transfer function in $0 - 5$ dimensionless frequency range. The model is able to reconstruct time-series in comparison to the ground truth and generalizes well beyond the parameters they were trained on.

Chapter 4 presents results of a set of stochastic FEM simulations to study basin effects in cases where higher frequency response is desirable and accurate basin material representation is of interest. However, the lack of geotechnical information prevents us from performing a deterministic analysis. Therefore, the material in the basin is presented by a correlated random field and we studied parameters such as coefficient of variation, correlation lengths and types of autocorrelation function to examine their impact on surface acceleration using Monte Carlo technique. We concluded that coefficient of variation is the most influential parameter on surface response, followed by correlation lengths and type of autocorrelation function.

5.2 Future Work

As future directions, the following paths might be taken:

- In Chapter 2:
  - Given the fact that all the analysis in this research assumed the simplest elastic material for the sake of interpretability and understanding the physics, one can extend the analysis to include nonlinearity in the simulation as it happens in reality, for instance in Kathmandu basin during the Gorkha Earthquake.
  - The analysis of this research was focused on $2D$ domain. Extension to $3D$ will be beneficial as it was shown in the literature that in some cases, $2D$ analysis may not be able to capture the full picture. This happened in Mexico City during the Michoàcan Earthquake where some attributed the long duration of shaking to $3D$ effects.
  - Following our goal to simplify the problem in order to better understand the phenomena from a physical point of view, we did not include stratigraphy information in our analysis, such a modification will impact the resultant wave field. While the amplitude of surface motion may decrease due to a more smooth transition of shear wave velocity in a stratified basin, one might be able to observe more realistic response.
- In Chapter 3:
  - In Chapter 3, we used a neural network to estimate surface acceleration time-series of a basin given few parameters as input. Such an approach can be used

to better address local site effects in general. A hybrid method can be developed in which empirical data is supplemented by numerical simulations, and a NN replaces arbitrary current functional format of GMPEs.

  – Moreover, for the case of a basin analysis, a more accurate material representation can also be incorporated, namely including depth dependency of material. NN or other machine learning based methods can be used to approach this problem.

- In Chapter 4:

  – Similarly to the point about stratified basin, stochastic FEM simulations can also be helpful in such cases. Instead of defining a horizontally layered medium, one can use a correlated random field to represent a basin while including the variation of velocity and density with depth. This is an easy modification to our simulations in Chapter 4 which in turn results in a more realistic basin configurations.

  – As was mentioned before, the major challenge for MC-type analysis is the computational time. For the case of analyzes in Chapter 4, 50 realizations were used, each taking few hours to complete. The computational time obviously depends on the frequency level of interest, model configurations, among other factors. Overall, this can be a setback. A procedure similar to Chapter 3 can be followed to improve computational efficiency of the simulation procedure. Assuming von Karman autocorrelation function is an appropriate representation for solid Earth, three parameters, namely COV, θ_x and θ_z, are parameters that need to be considered in addition to dimensionless parameters that were used in Chapter 3. Depending on the configuration of a basin and input motion characteristic, it might be possible to fix one of the θ_x or θ_z parameters. Having set the initial parameter, defining a range for each parameters and generating synthetic training, one is able to gather available empirical data to supplement synthetic data. Finally, a model can be trained to learn the behavior for different scenarios.

Bibliography

N. A. Abrahamson and W. J. Silva. Summary of the Abrahamson & Silva NGA ground-motion relations. *Earthquake Spectra*, 24(1):67–97, 2008.

N. A. Abrahamson, W. J. Silva, and R. Kamai. Summary of the ASK14 ground motion relation for active crustal regions. *Earthquake Spectra*, 30(3):1025–1055, 2014.

B. M. Adams. Basin-edge Effects from SH-wave modelling with reference to the Lower Hutt Valley, New Zealand. *PhD Thesis*, 2000.

K. Aki and B. Chouet. Origin of coda waves: Source, attenuation, and scattering effects. *Journal of geophysical research*, 80(23):3322–3342, 1975.

K. Aki and K. L. Larner. Surface motion of a layered medium having an irregular interface due to incident plane SH waves. *Journal of Geophysical Research*, 75(5):933, 1970.

K. Aki and P. G. Richards. Quantitative seismology. University Science Books, 2002.

Z. Al-Yuncha and F. Luzón. On the horizontal-to-vertical spectral ratio in sedimentary basins. *Bulletin of the Seismological Society of America*, 90(4):1101–1106, 2000. ISSN 0037-1106. doi: 10.1785/0119990135. URL <GotoISI>://WOS:000089060700023.

D. Asimaki, K. Mohammadi, H. B. Mason, R. K. Adams, S. Rajuare, and D. Khadka. Observations and simulations of basin effects in the Kathmandu valley during the 2015 Gorkha. *Earthquake Spectra*, 33(S1), 2017.

D. Assimaki, A. Pecker, R. Popescu, and J. Prevost. Effects of spatial variability of soil properties on surface ground motion. *Journal of Earthquake Engineering*, 7(1):1–44, 2003.

J. P. Avouac, L. Meng, S. Wei, T. Wang, and J. P. Ampuero. Lower edge of locked Main Himalayan Thrust unzipped by the 2015 Gorkha earthquake. *Nature Geoscience*, 8: 708–711, 2015.

P. Ayoubi, D. Asimaki, and K. Mohammadi. Basin effects in strong ground motion: A case study from the 2015 Gorkha, Nepal earthquake. In *Geotechnical earthquake engineering and soil dynamics V*, Austin, 2018. ASCE.

P. Ayoubi, K. Mohammadi, and D. Asimaki. A systematic analysis of basin effects on surface ground motion. *Soil Dynamics and Earthquake Engineering*, 141, 2021.

Y. Bao, Z. Tang, H. Li, and Y. Zhang. Computer vision and deep learning–based data anomaly detection method for structural health monitoring. *Structural Health Monitoring*, 18(2), 2019.

P. Y. Bard and M. Bouchon. The seismic response of sediment-filled valleys-Part II. The case of incident P and SV waves. *Bulletin of Seismological Society of America*, 70(5): 1921–1941, 1980.

P. Y. Bard, M. Campillo, F. J. Chávez-Garcia, and F. J. Sánchez-Sesma. The Mexico earthquake of Sep 19, 1985- A theoretical investigation of large and small scale amplification effects in the Mexico city valley. *Earthquake Spectra*, 4(3):609–633, 1988.

K. Battan and J. P. Narayan. 3D basin-shape ratio effects on frequency content and spectral amplitudes of basin-generated surface waves and associated spatial ground motion amplification and differential ground motion. *Journal of Seismology*, 19(2):293–316, 2015. ISSN 1383-4649. doi: 10.1007/s10950-014-9466-8. URL <GotoISI>://WOS:000351393100002.

S. M. Bijukchhen, N. Takai, M. Shigefuji, M. Ichiyanagi, T. Sasatani, and Y. Sugimura. Estimation of 1-D velocity models beneath strong-motion observation sites in the Kathmandu Valley using strong-motion records from moderate-sized earthquakes. *Earth,Planets and Space*, 69(1):97, 2017.

D. Boore. Simulation of ground motion using the stochastic method. *Pure and Applied Geophysics*, 160:635–676, 2003.

D. M. Boore. Love Waves in nonuniform wave guides: Finite Difference calculations. *Journal of Geophysical Research*, 75(8):1512–1527, 1970.

D. M. Boore, K. L. Larner, and K. Aki. Comparison of two independent methods for the solution of wave-scattering problems: Response of a sedimentary basin to vertically incident SH waves. *Journal of Geophysical Research*, 76(2):558–569, 1971. ISSN 2156-2202. doi: 10.1029/JB076i002p00558. URL http://dx.doi.org/10.1029/JB076i002p00558.

D. M. Boore, J. P. Stewart, E. Seyhan, and G. M. Atkinson. NGA-West2 equations for predicting PGA, PGV, and 5% damped PSA for shallow crustal earthquakes. *Earthquake Spectra*, 30(3):1057–1085, 2014.

E. Buckingham. On physically similar systems: Illustrations of the use of dimensional analysis. *Physical Review*, 4(4):345–376, 1914.

K.W. Campbell and Y. Bozorgnia. NGA-West2 ground motion model for the average horizontal components of PGA, PGV, and 5% damped linear acceleration response spectra. *Earthquake Spectra*, 30(3):1087–1115, 2014.

M. Campillo, P. Y. Bard, F. Nicollin, and F. J. Sánchez-Sesma. The Mexico earthquake of September 19, 1985-The incident wavefield in Mexico City during the great Michoacan earthquake and its intersection with the deep basin. *Earthquake Spectra*, 4(3):591–608, 1988.

CERN. Eurocode 8: Design of structures for earthquake resistance - Part 1: General rules, seismic actions and rules for buildings, European Standard EN 1998-1. 2004.

F. J. Chávez-Garcia and P. Y. Bard. Site effects in Mexico-City 8 years after the September 1985 Michoacan earthquakes. *Soil Dynamics and Earthquake Engineering*, 13(4):229–247, 1994. ISSN 0267-7261. doi: 10.1016/0267-7261(94)90028-0. URL <GotoISI>://WOS:A1994PF48600001.

B. S. J. Chiou and R. R. Youngs. Update of the Chiou and Youngs NGA model for the average horizontal component of peak ground motion and response spectra. *Earthquake Spectra*, 30(3):1117–1153, 2014.

V. M. Cruz-Atienza, J. Tago, J. D. Sanabria-Gomez, E. Chaljub, V. Etienne, J. Virieux, and L. Quintanar. Long duration of ground motion in the paradigmatic valley of Mexico. *Scientific Reports*, 6:38807, 2016. ISSN 2045-2322. doi: 10.1038/srep38807. URL <GotoISI>://WOS:000389570200001.

P. Cundall, H. Hansteen, S. Lacasse, and P. Selnes. NEESI soil structure interaction program for dynamic and static problems. *Tech. Rep. 51508-9, Norwegian Geotechnical Institute*, 1980.

G. Di-Giulio, R. de Nardis, P. Boncio, G. Milana, G. Rosatelli, F. Stoppa, and G. Lavecchia. Seismic response of a deep continental basin including velocity inversion: The Sulmona intramontane basin (Central Apennines, Italy). *Geophysical Journal International*, 204 (1):418–439, 2016. ISSN 0956-540X. doi: 10.1093/gji/ggv444. URL <GotoISI>://WOS:000368427000027.

J. Douglas. Ground motion prediction equations 1964 2019. *United Kingdom, Glasgow: University of Strathclyde*, 2019.

M. Dravinski. Influence of interface depth upon strong ground motion. *Bulletin of the Seismological Society of America*, 72(2):597–614, 1982. URL http://www.bssaonline.org/content/72/2/597.abstract.

E. El Habar, C. Cornou, D. Jongmans, D. Y. Abdelmassih, and F. Lopez-Caballero. Influence of 2D heterogeneous elastic soil properties on surface ground motion spatial variability. *Soil Dynamics and Earthquake Engineering*, 123(1):75–90, 2019.

A. Esmaeilzadeh and D. Motazedian. Sensitivity analysis for Finite-Difference seismic basin modeling: A case study for Kinburn Basin, Ottawa, Canada. *Bulletin of the Seismological Society of America*, 109(6):2305–2324, 2019.

E. Faccioli, F. Maggio, R. Paolucci, and A. Quarteroni. 2D and 3D elastic wave propagation by a pseudo-spectral domain decomposition method. *Journal of Seismology*, 1(3):237–251, 1997.

A. Frankel and R. W. Clayton. A Finite-Difference simulation of wave propagation in two-dimensional random media. *Bulletin of Seismological Society of America*, 74(6):2167–2186, 1984.

A. Frankel, E. Wirth, N. Marafi, J. Vidale, and W. Stephenson. Broadband synthetic seismograms for magnitude 9 earthquakes on the Cascadia Megathrust based on 3D simulations and stochastic synthetics, Part 1: Methodology and overall results. *Bulletin of the Seismological Society of America*, 108:2347–2369, 2018.

F. Gelagoti, R. Kourkoulis, I. Anastasopoulos, T. Tazoh, and G. Gazetas. Seismic wave propagation in a very soft alluvial valley: Sensitivity to ground-motion details and soil nonlinearity, and generation of a parasitic vertical component. 100(6):3035–3054, 2010.

F. Gelagoti, R. Kourkoulis, I. Anastasopoulos, and G. Gazetas. Nonlinear dimensional analysis of trapezoidal valleys subjected to vertically propagating SV waves. *Bulletin of the Seismological Society of America*, 102(3):999–1017, 2012. ISSN 0037-1106. doi: 10.1785/0120110182. URL <GotoISI>://WOS:000304870500008.

R. W. Graves, A. Pitarka, and P. G. Somerville. Ground-motion amplification in the Santa Monica Area: Effects of shallow basin-edge structure . *Bulletin of Seismological Society of America*, 88(5):1224–1242, 1998.

S. Hallier, E. Chaljub, M. Bouchon, and H. Sekiguchi. Revisiting the basin-edge effect at Kobe during the 1995 Hyogo-Ken Nanbu earthquake. *Pure and Applied Geophysics*, 165(9-10):1751–1760, 2008. ISSN 0033-4553. doi: 10.1007/s00024-008-0404-y. URL <GotoISI>://WOS:000261576100003.

H. Harbrecht, M. Peters, and M. Siebenmorgen. Efficient approximation of random fields for numerical applications. *Numerical Linear Algebra with Applications*, 22(4):596–617, 2015.

K. He, X. Zhang, S. Ren, and J. Sun. Deep residual learning for image recognition. *In Proceedings of the IEEE Conference on Computer Vision and Pattern Recognition*, pages 770–778, 2016.

M. Horike, H. Uebayashi, and Y. Takeuchi. Seismic response in three-dimensional sedimentary basin due to plane S wave incidence. *Journal of Physics of the Earth*, 38: 261–284, 1990.

A. Ishimaru. Wave propagation and scattering in random media. *New York: Academic Press*, 2, 1978.

R. Jozefowicz, O. Vinyals, M. Schuster, M. Shazeer, and Y. Wu. Exploring the limits of language modeling. *arXiv preprint*, 2016.

H. Kawase. The cause of the damage belt in Kobe:“The basin-edge effect,” constructive interference of the direct S-wave with the basin-induced diffracted/Rayleigh waves. *Seismological Research Letter*, 67(5):25–34, 1996.

H. Kawase and K. Aki. A study on the response of a soft basin for incident S, P, and Rayleigh waves with special reference to the long duration observed in Mexico City. *Bulletin of the Seismological Society of America*, 79(5):1361–1382, 1989. ISSN 0037-1106. URL <GotoISI>://WOS:A1989AT83700003.

D. P. Kingma and J. Ba. Adam: A method for stochastic optimization. *arXiv preprint arXiv: 1412.6980*, 2014.

D. Komatitsch and J. P. Vilotte. The Spectral Element Method : An efficient tool to simulate the seismic response of 2D and 3D geological structures. *Bulletin of the Seismological Society of America*, 88(2):368–392, 1998. ISSN 1943-3573.

D. Komatitsch, Q. Liu, J. Tromp, P. Suss, C. Stidham, and J. H. Shaw. Simulations of ground motion in the Los Angeles basin based upon the Spectral-Element Method. *Bulletin of the Seismological Society of America*, 94(1):187–206, 2004.

D. M. Kusanovic, E. E. Seylabi, A. Kottke, and D. Asimaki. Seismo-vlab: A parallel object-oriented platform for reliable nonlinear seismic wave propagation and soil-structure interaction simulation. *To be submitted to Computer Methods in Applied Mechanics and Engineering*, 2020.

Y. LeCun, Y. Bengio, and G. Hinton. Deep learning. *Nature*, 521, 2015.

S. Lee, H. Chen, and B. Huang. Simulations of strong ground motion and 3D amplification effect in the Taipei Basin by using a composite grid finite-difference method. *Bulletin of Seismological Society of America*, 98(3):1229–1242, 2008.

J. Lysmer and R. L. Kuhlemeyer. Finite dynamic model for infinite media. *Journal of Engineering Mechanics Division*, 95:859–878, 1969.

P. M. Mai and G. C. Beroza. A spatial random field model to characterize complexity in earthquake slip. *Journal of Geophysical Research: Solid Earth*, 107(B11):ESE–10, 2002.

F. McKenna, G. Fenves, and M. Scott. Open system for earthquake engineering simulation. *Pacific Earthquake Engineering Research Center*, 2000.

S. E. Minson, A. S. Baltay, E. S. Cochran, T. C. Hanks, M. T. Page, S. K. McBride, K. R. Milner, and M. A. Meier. The limits of earthquake early warning accuracy and best alerting strategy. *Scientific Reports*, 9(1), 2019.

P. Moczo, J. Kristek, P. Y. Bard, S. Stripajova, F. Hollender, Z. Chovanova, M. Kristekova, and D. Sicilia. Key structural parameters affecting earthquake ground motion in 2D and 3D sedimentary structures. *Bulletin of Earthquake Engineering*, 16(6), 2018.

T. Momoi. Scattering of Rayleigh waves in an elastic quarter space. *Journal of Physics of the Earth*, 28(4):385–413, 1980.

T. K. Mossessian and M. Dravinski. Application of a hybrid method for scattering of P, SV, and Rayleigh waves by near-surface irregularities. *Bulletin of the Seismological Society of America*, 77(5):1784–1803, 1987. ISSN 0037-1106. URL `<GotoISI>://WOS:A1987K149800017`.

S. M. Mousavi, L. E. William, W. Zhu, Y. L. Chuang, and G. C. Beroza. Earthquake transformer—an attentive deep-learning model for simultaneous earthquake detection and phase picking. *Nature Communications*, 11(1), 2020.

N. Nakata and G. C. Beroza. Stochastic characterization of mesoscale seismic velocity heterogeneity in Long Beach, California. *Geophysical Journal International*, 203(1), 2015.

J. P. Narayan. Effects of impedance contrast and soil thickness on basin-transduced Rayleigh waves and associated differential ground motion. *Pure and Applied Geophysics*, 167 (12):1485–1510, 2010. ISSN 0033-4553. doi: 10.1007/s00024-010-0131-z. URL <GotoISI>://WOS:000285099100003.

J. P. Narayan and S. Kumar. Effects of soil layering on the characteristics of basin-edge induced surface waves. *Acta Geophysica*, 57(2):294–310, 2009. ISSN 1895-6572. doi: 10.2478/s11600-008-0075-1. URL <GotoISI>://WOS:000264603000004.

K. B. Olsen, J. C. Pechmann, and G. T. Schuster. Simulation of 3D elastic wave propagation in the Salt Lake Basin. *Bulletin of the Seismological Society of America*, 85(6):1688–1710, 1995. ISSN 0037-1106. URL <GotoISI>://WOS:A1995TL81400012.

S. Pezzuto, A. Quaglino, and M. Potse. On sampling spatially-correlated random fields for complex geometries. *International Conference on Functional Imaging and Modeling of the Heart*, pages 103–111, 2019.

M. Pilz and F. Cotton. Does the one-dimensional assumption hold for site response analysis? A study of seismic site responses and implication for ground motion assessment using KiK-Net strong-motion data. *Earthquake Spectra*, 35(2), 2019.

M. Pilz, F. Cotton, H. N. T. Razafindrakoto, G. Weatherill, and T. Spies. Regional broad-band ground-shaking modelling over extended and thick sedimentary basins: An example from the Lower Rhine Embayment (Germany). *Bulletin of Earthquake Engineering*, 19 (2):581–603, 2021.

A. Pitarka and K. Irikura. Basin structure effects on long-period strong motions in the San Fernando Valley and the Los Angeles basin from the 1994 Northridge earthquake and an aftershock. *Bulletin of the Seismological Society of America*, 86(1B):S126–S137, 1996.

A. Pitarka, K. Irikura, T. Iwata, and H. Sekiguchi. Three-dimensional simulation of the near-fault ground motion for the 1995 Hyogo-ken Nanbu (Kobe), Japan, earthquake. *Bulletin of the Seismological Society of America*, 88(2):428–440, 1998. ISSN 0037-1106. URL <GotoISI>://WOS:000073210300009.

R. Popescu. Effects of soil spatial variability on liquefaction resistance: Experimental and theoretical investigations. *In Proc., 4th Int. Symposium on Deformational Characteristics of Geomaterials*, 1:73–94, 2008.

R. Popescu, J. H Prevost, and G. Deodatis. Spatial variability of soil properties: Two case studies. *Geotechnical Special Publication*, 75:568–579, 1998.

N. Ricker. The form and nature of seismic waves and the structure of seismograms. *Geophysics*, 5(4):348–366, 1940.

E. Riga, K. Makra, and K. Pitilakis. Aggravation factors for seismic response of sedimentary basins: A code-oriented parametric study. *Soil Dynamics and Earthquake Engineering*, 91, 2016.

E. Riga, K. Makra, and K. Pitilakis. Investigation of the effects of sediments inhomogeneity and nonlinearity on aggravation factors for sedimentary basins. *Soil Dynamics and Earthquake Engineering*, 110, 2018.

A. J. Rodgers, N. A. Petersson, A. Pitarka, D. B. McCallen, B. Sjogreen, and N. Abrahamson. Broadband (0–5 Hz) fully deterministic 3D ground-motion simulations of a magnitude 7.0 Hayward fault earthquake: Comparison with empirical ground-motion models and 3D path and site effects from source normalized intensities. *Seismological Research Letters*, 90(3):1268–1284, 2019.

M. Rota, C. G. Lai, and C. L. Strobbia. Stochastic 1D site response analysis at a site in central Italy. *Soil Dynamics and Earthquake Engineering*, 31:626–639, 2011.

T. Saito, H. Sato, M. Ohtake, and K. Obara. Unified explanation of envelope broadening and maximum-amplitude decay of high-frequency seismograms based on the envelope simulation using the Markov approximation: Forearc side of the volcanic front in northeastern Honshu, Japan. *Journal of Geophysical Research: Solid Earth*, 110, 2005.

F. J. Sánchez-Sesma and F. Luzón. Seismic Response of 3-dimensional alluvial valleys for incident P-wave, S-waves, and Rayleigh-waves. *Bulletin of the Seismological Society of America*, 85(1):269–284, 1995. URL <GotoISI>://WOS:A1995QJ46900019.

F. J. Sánchez-Sesma, L. E. Pérez-Rocha, and E. Reinoso. Ground motion in Mexico City during the April 25, 1989, Guerrero earthquake. *Tectonophysics*, 218(1):127–140, 1993.

W. H. Savran and K. B. Olsen. Model for small-scale crustal heterogeneity in Los Angeles basin based on inversion of sonic log data. *Geophysical Journal International*, 205: 856–863, 2016.

K. Sawazaki, H. Sato, and T. Nishimura. Envelope synthesis of shortperiod seismograms in 3-D random media for a point shear dislocation source based on forward scattering approximation: application to small strike-slip earthquakes in southwestern Japan. *Journal of Geophysical Research: Solid Earth*, 116, 2011.

J. Shi and D. Asimaki. A generic velocity profile for basin sediments in California conditioned on Vs30. *Seismological Research Letters*, 89(4):1397–1409, 2018.

P. Spudich and M. Iida. The seismic coda, site effects, and scattering in alluvial basins studied using aftershocks of the 1986 North Palm Springs, California, earthquake as source arrays. *Bulletin of Seismological Society of America*, 83(6):1721–1743, 1993.

M. Stupazzini, R. Paolucci, and H. Igel. Near-fault earthquake ground-motion simulation in the Grenoble Valley by a high-performance Spectral Element code. *Bulletin of the Seismological Society of America*, 99(1):286–301, 2009.

N. Takai, M. Shigefuji, S. Rajaure, S. Bijukchhen, M. Ichiyanagi, M. R. Dhital, and T. Sasatani. Strong ground motion in the Kathmandu Valley during the 2015 Gorkha, Nepal, earthquake. *Earth, Planets and Space*, 68(1):10, 2016.

S. Takemura, T. Furumura, and T. Maeda. Scattering of high-frequency seismic waves caused by irregular surface topography and small-scale velocity inhomogeneity. *Geophysical Journal International*, 201:459–474, 2015.

M. D. Trifunac. Surface motion of a semi-cylindrical alluvial valley for incident plane SH waves. *Bulletin of the Seismological Society of America*, 61(6):1755–1770, 1971. URL http://www.bssaonline.org/content/61/6/1755.abstract.

N. C. Tsai and G. W. Housner. Calculation of surface motions of a layered half-space. *Bulletin of the Seismological Society of America*, 60(5):1625–1651, 1970. ISSN 0037-1106. URL <GotoISI>://WOS:A1970H693300012.

A. Vasuki and S. Govindaraju. Deep neural networks for image classification. *Deep Learning for Image Processing Applications*, 31, 2017.

A. Voulodimos, N. Doulamis, A. Doulamis, and E. Protopapadakis. Deep learning for computer vision: A brief review. *Computational Intelligence and Neuroscience*, 2018.

S. Wei, M. Chen, X. Wang, R. W. Graves, E. Lindsey, T. Wang, , C. Karakas, and D. Helmberger. The 2015 Gorkha (Nepal) earthquake sequence: I. Source modeling and deterministic 3D ground shaking. *Tectonophysics*, 722:447–461, 2018.

H. L. Wong and M. D. Trifunac. Surface motion of a semi-elliptical alluvial valley for incident plane SH waves. *Bulletin of the Seismological Society of America*, 64(5):1389–1408, 1974. URL http://www.bssaonline.org/content/64/5/1389.abstract.

F. Yang and J. Ma. Deep-learning inversion: A next-generation seismic velocity model building method. *Geophysics*, 84(4), 2019.

C. B. Zhu and D. Thambiratnam. Interaction of geometry and mechanical property of trapezoidal sedimentary basins with incident SH waves. *Bulletin of Earthquake Engineering*, 14(11):2977–3002, 2016. ISSN 1570-761X. doi: 10.1007/s10518-016-9938-z. URL <GotoISI>://WOS:000386073200003.

O. Zielke, M. Galis, and P. M. Mai. Fault roughness and strength heterogeneity control earthquake size and stress drop. *Geophysical Research Letters*, 44(2):777–783, 2017.